Mapping variations in bedrock weathering with slope aspect under a sedimentary ridge-valley system using near-surface geophysics and drilling

Berit Hudson-Rasmussen[1], Mong-Han Huang[1], W. Jesse Hahm[2], Daniella Rempe[3], David N Dralle[4], and Mariel D Nelson[5]

[1]University of Maryland, College Park
[2]Simon Fraser University
[3]University of Texas at Austinn
[4]Pacific Southwest Research Station, United States Forest Service
[5]University of Texas at Austin

May 17, 2023

Abstract

Understanding how soil thickness and bedrock weathering vary across ridge and valley topography is needed to constrain the flowpaths of water and sediment production within a landscape. Here, we investigate saprolite and weathered bedrock properties across a ridge-valley system in the Northern California Coast Ranges, USA, where topography varies with slope aspect such that north facing slopes have thicker soils and are more densely vegetated than south facing slopes. We use active source seismic refraction surveys to extend observations made in boreholes to the hillslope scale. Seismic velocity models across several ridges capture a high velocity gradient zone (from 1000 to 2500 m/s) located ˜4-13 m below ridgetops, that coincides with transitions in material strength and chemical depletion observed in boreholes. Comparing this transition depth across multiple north and south-facing slopes, we find that the thickness of saprolite does not vary with slope aspects. Additionally, seismic survey lines perpendicular and parallel to bedding planes reveal weathering profiles that thicken upslope and taper downslope to channels. Using a rock physics model incorporating seismic velocity, we estimate the total porosity of the saprolite and find that inherited fractures contribute a substantial amount of pore space in the upper 6 m, and the lateral porosity structure varies strongly with hillslope position. The aspect-independent weathering structure suggests the contemporary critical zone structure at Rancho Venada is a legacy of past climate and vegetation conditions.

Hosted file

`963341_0_art_file_10987694_rwmtb7.docx` available at https://authorea.com/users/619265/articles/643889-mapping-variations-in-bedrock-weathering-with-slope-aspect-under-a-sedimentary-ridge-valley-system-using-near-surface-geophysics-and-drilling

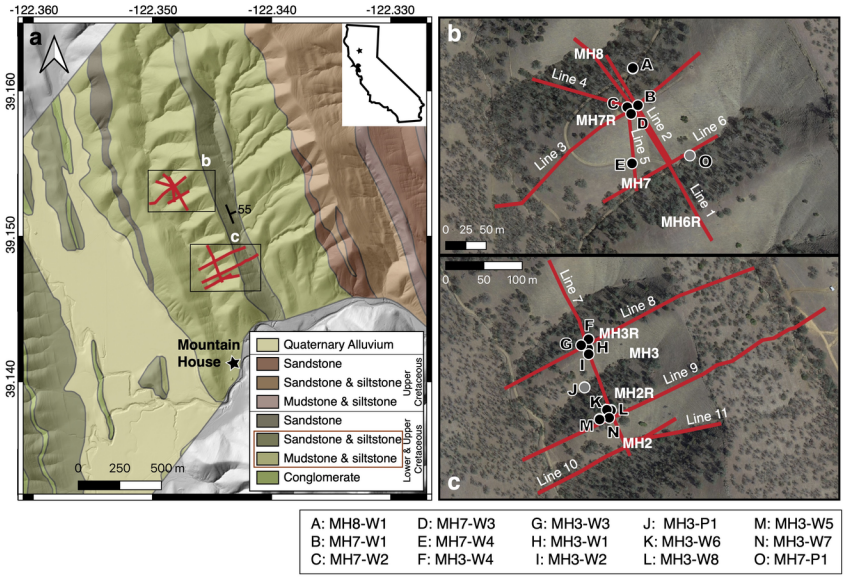

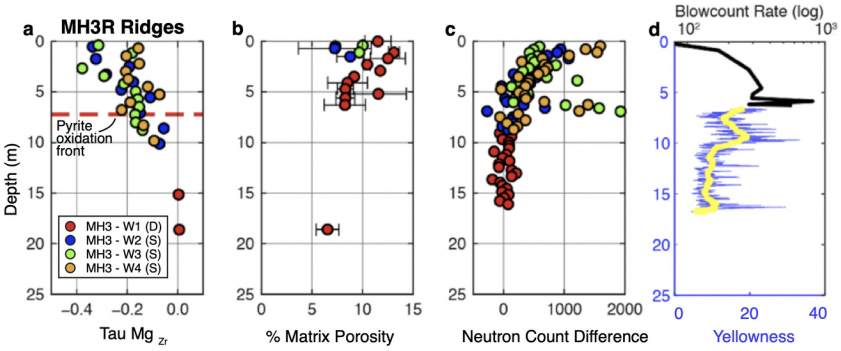

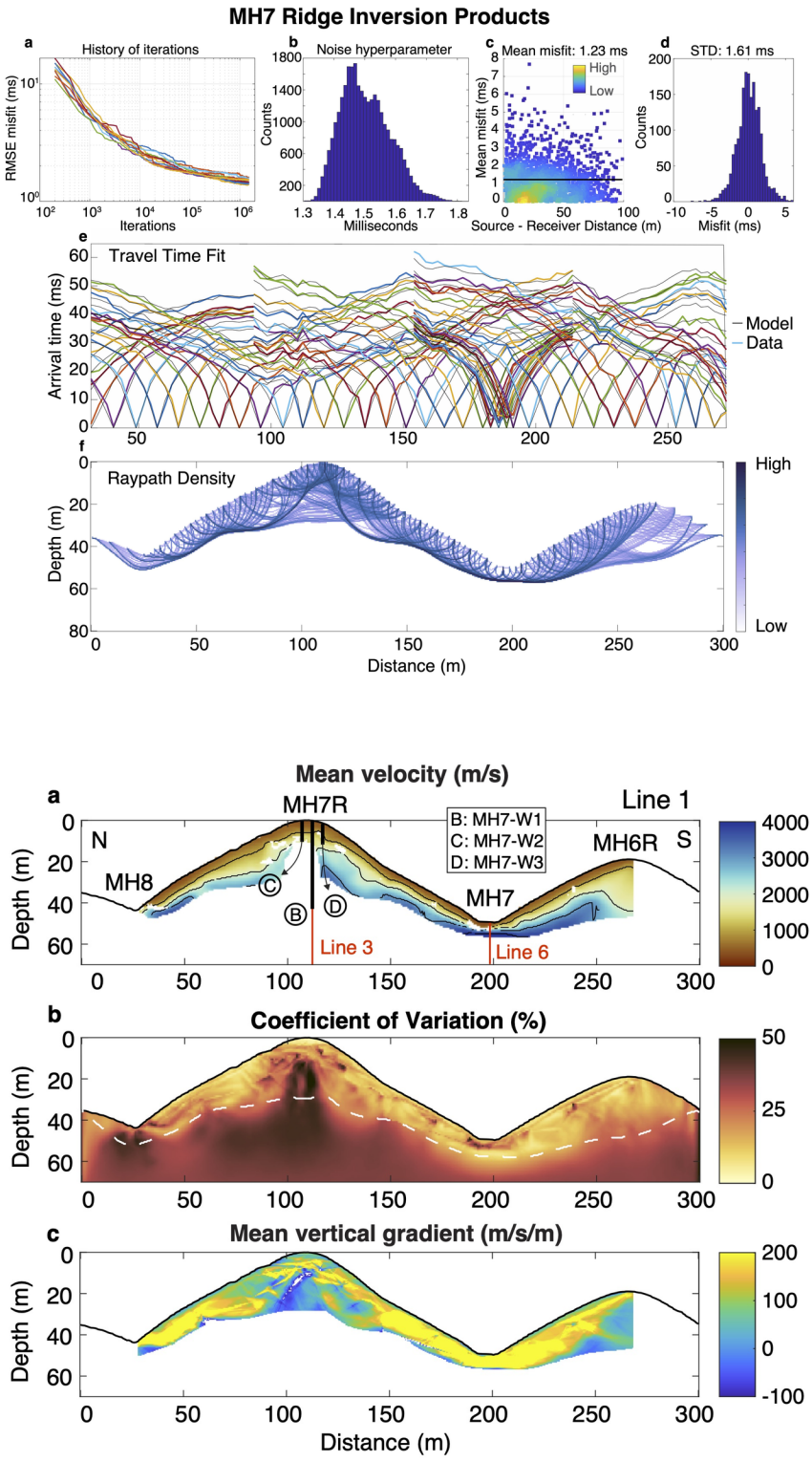

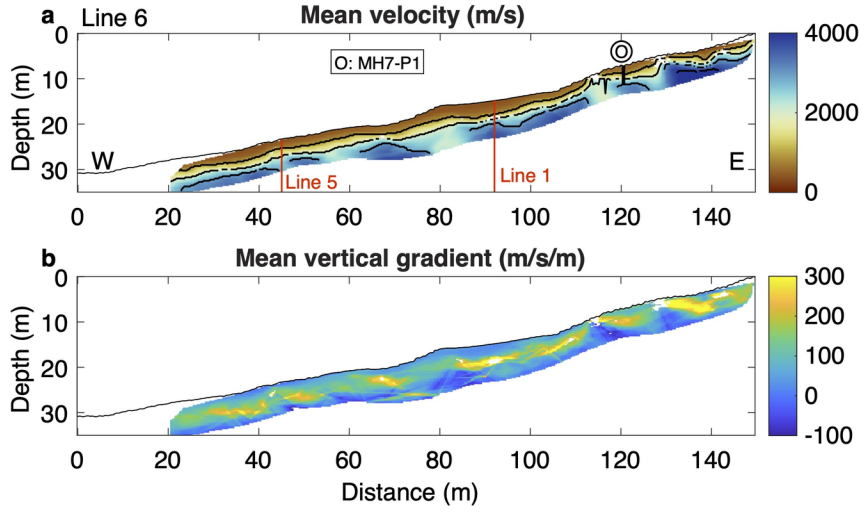

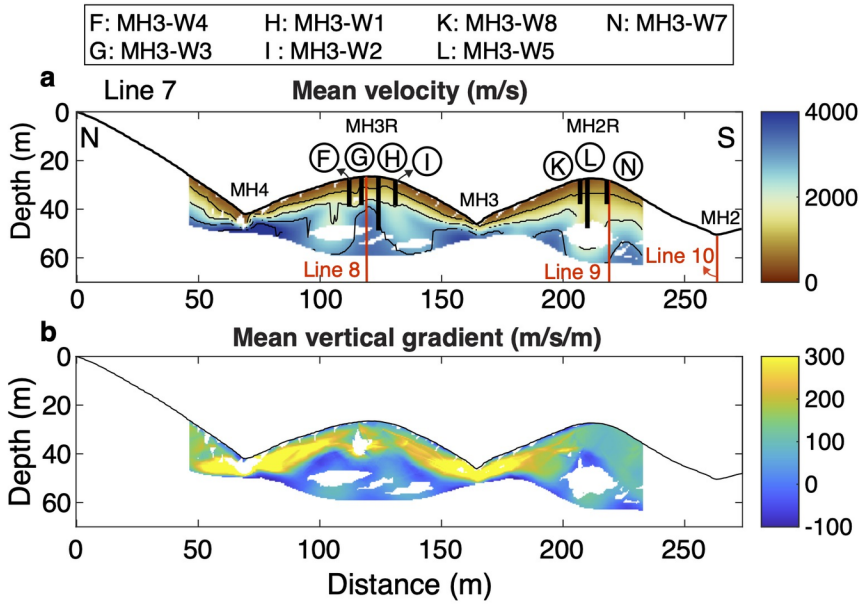

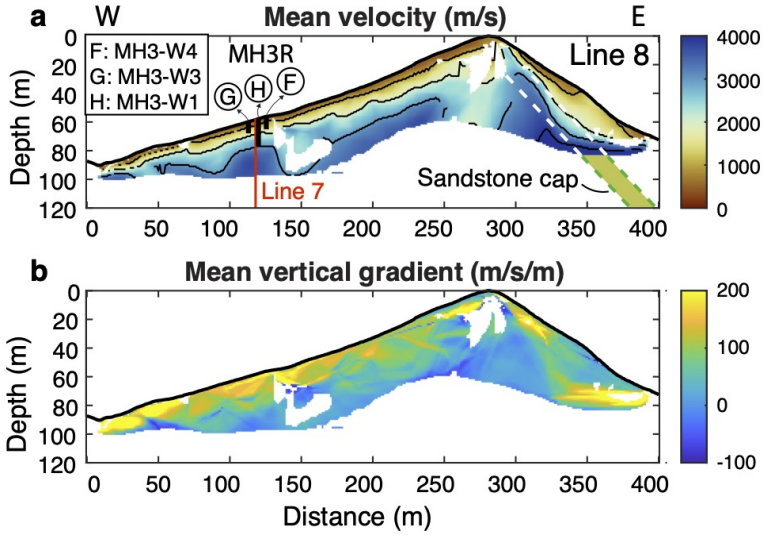

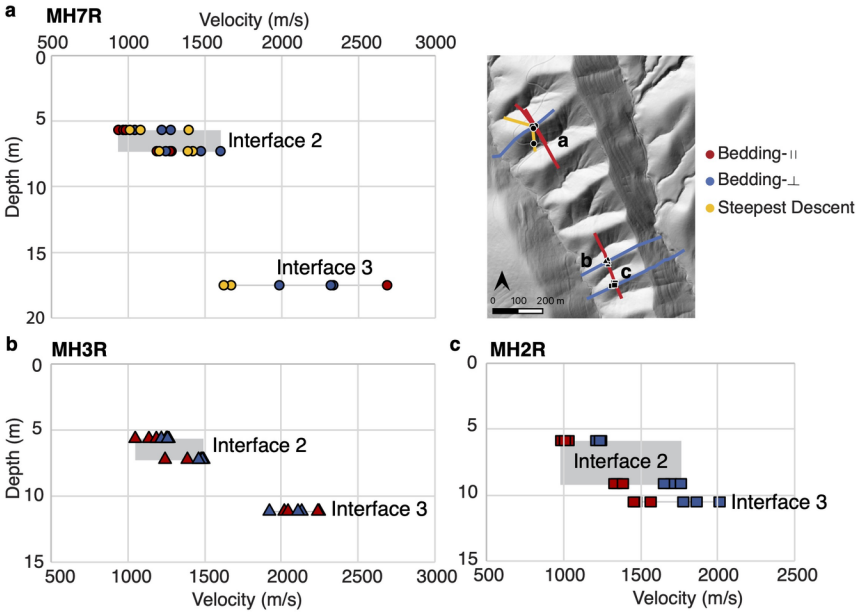

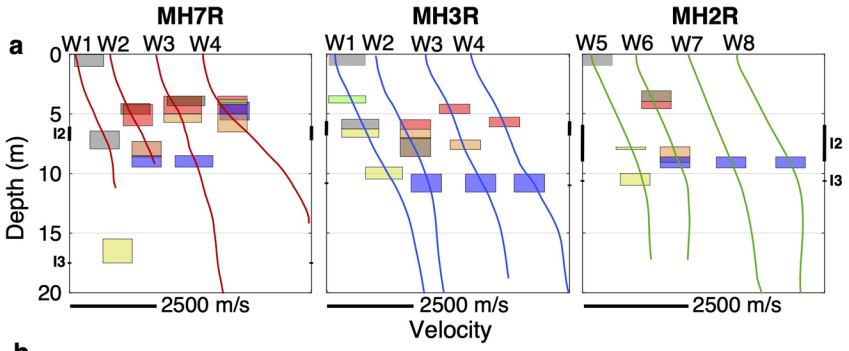

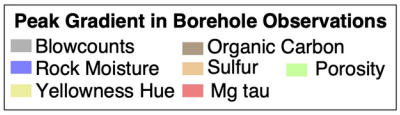

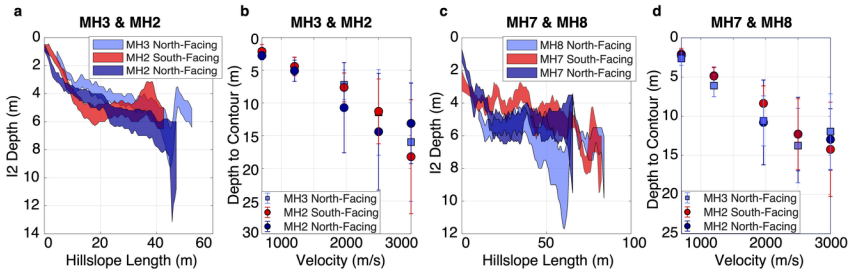

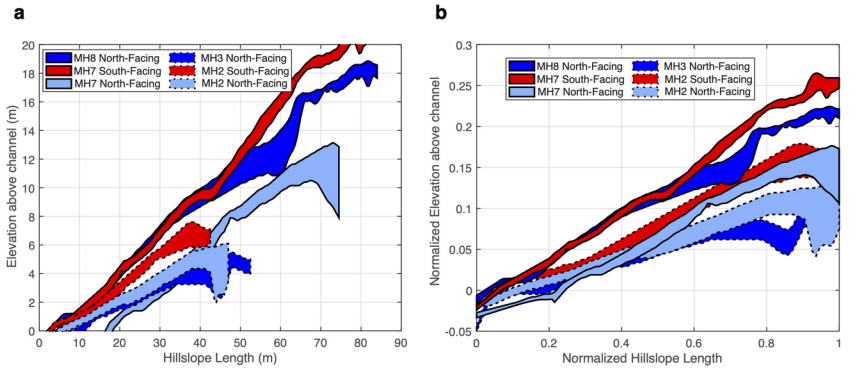

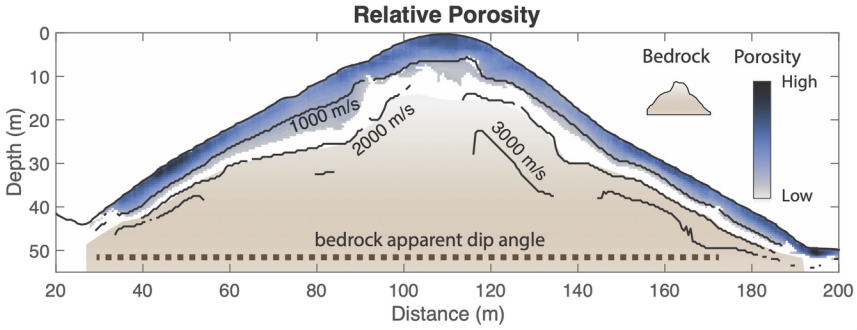

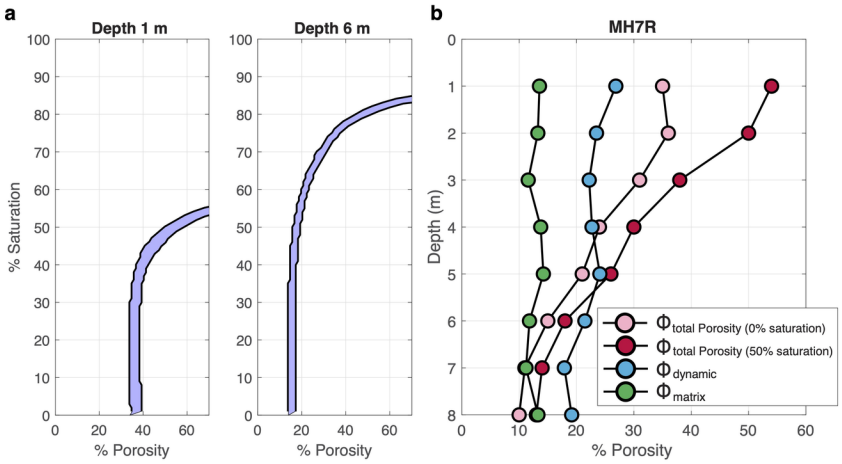

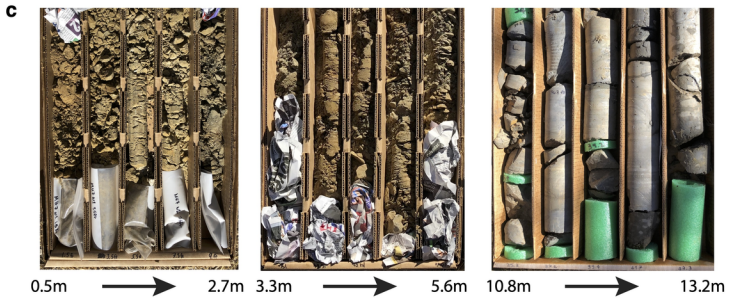

Mapping variations in bedrock weathering with slope aspect under a sedimentary ridge-valley system using near-surface geophysics and drilling

Berit M. Hudson Rasmussen[1], Mong-Han Huang[1], W. Jesse Hahm[2], Daniella M. Rempe[3], David Dralle[4] and Mariel D. Nelson[3]

[1]Department of Geology, University of Maryland, College Park, MD, USA,
[2]Department of Geography, Simon Fraser University, Burnaby, BC, Canada,
[3]Department of Geosciences, Jackson School of Geosciences, The University of Texas at Austin, Austin, TX, USA,
[4]Pacific Southwest Research Station, United States Forest Service, Albany, CA, USA

Abstract

Understanding how soil thickness and bedrock weathering vary across ridge and valley topography is needed to constrain the flowpaths of water and sediment production within a landscape. Here, we investigate saprolite and weathered bedrock properties across a ridge-valley system in the Northern California Coast Ranges, USA, where topography varies with slope aspect such that north facing slopes have thicker soils and are more densely vegetated than south facing slopes. We use active source seismic refraction surveys to extend observations made in boreholes to the hillslope scale. Seismic velocity models across several ridges capture a high velocity gradient zone (from 1000 to 2500 m/s) located ~4-13 m below ridgetops, that coincides with transitions in material strength and chemical depletion observed in boreholes. Comparing this transition depth across multiple north and south-facing slopes, we find that the thickness of saprolite does not vary with slope aspects. Additionally, seismic survey lines perpendicular and parallel to bedding planes reveal weathering profiles that thicken upslope and taper downslope to channels. Using a rock physics model incorporating seismic velocity, we estimate the total porosity of the saprolite and find that inherited fractures contribute a substantial amount of pore space in the upper 6 m, and the lateral porosity structure varies strongly with hillslope position. The aspect-independent weathering structure suggests the contemporary critical zone structure at Rancho Venada is a legacy of past climate and vegetation conditions.

Plain Language Summary

Below Earth's ground surface, porous space within weathered bedrock can store a significant amount of water, which is essential for ecosystems, particularly during the growing seasons. Collecting hydrologic data and core samplings from boreholes provides direct measurements about how bedrock is weathered and broken down towards the earth surface. Our study site is located in a series of ridges and valleys in Northern California, USA, where the local Mediterranean climate has distinctive dry summers and wet winters. This site represents a common topography along the east side of the Coast Ranges. In addition to synthesizing borehole and hydrologic data, we conduct complementary seismic refraction surveys to image material strength in the subsurface in 2D. These images can better capture the lateral variation of weathering zone thickness from channels to ridgetops. Seismic velocity derived from seismic refraction data shows an increase of material strength at the transition zone between saprolite and bedrock that agrees with borehole observations. Although vegetation density is much higher in the north- than the south-facing hills, the depth to fresh bedrock is roughly the same.

Our results also indicate that porous spaces in the weathered bedrock have the potential to store more water than annual precipitation.

Key points

1. A combination of geophysics and borehole measurements allows us to characterize lateral critical zone structure in a ridge-channel system.
2. Despite a strong aspect dependent contrast in soil thickness, saprolite thickness does not vary with slope aspect.
3. Rock physics modeling using seismic velocity suggests inherited bedrock fractures substantially contribute to saprolite total porosity.

1. INTRODUCTION

The transformation of fresh bedrock into weathered bedrock and mobile soil in the subsurface critical zone is facilitated by changes in chemical composition, material strength, and porosity with depth. These processes dictate how landscapes store and release water to trees and streams (Brooks et al., 2015). Documenting the structure of the critical zone, including the thickness and subsurface topography of different materials, is therefore crucial to quantifying water storage (Rempe & Dietrich, 2014; Flinchum et al., 2018a; Callahan et al., 2020) and predicting ecosystem and landscape response to climate change (Godderis and Brantley, 2013; Callahan et al., 2022; Sullivan et al., 2022). Water storage dynamics are not homogenous at the hillslope scale, but are influenced by microtopography (Wang et al., 2021), elevation (Klos et al., 2017; Nielsen et al., 2021), and slope aspect (Anderson et al., 2014). Critical zone structure can additionally be modulated by lithology (Hahm et al., 2014; Leone et al., 2020) and climate (Inbar et al., 2018; Anderson et al., 2019). Exploration of the spatially variable hydrologic dynamics of a landscape therefore requires characterization of subsurface structure over broad spatial scales, and in different geologic settings.

Many studies have observed that with increased solar radiation on equator-facing hillslopes at mid-high latitudes, separate microclimates can be found on equator-facing (i.e., south-facing, in the northern hemisphere) versus pole-facing (i.e., north-facing) hillslopes (Pelletier et al., 2018). In presently precipitation-limited environments (as opposed to temperature-limited), north-facing slopes of the northern hemisphere tend to have more vegetation, and thicker, wetter soils, while south-facing slopes are drier and less vegetated, with thinner soils (Pelletier et al., 2018). While surface slope, tree density, and soil thickness have been well documented to vary based on aspect dependency (Bale et al., 1998; Inbar et al., 2018), fewer studies address the influence of aspect dependency and climate on deeper weathering transitions. Those that do, focus primarily on snow-dominated systems or granite lithology (Anderson et al., 2013; Anderson et al., 2014; Leone et al., 2020; Nielsen et al., 2021).

Seismic refraction can effectively capture the heterogeneity in the subsurface weathered bedrock structure, which can vary drastically from ridge to channel (Leone et al., 2020; Wang et al., 2021; Pasquet et al., 2022). By combining borehole and geophysical methods, recent studies have calibrated geophysical data to direct observations to infer weathering thickness across a landscape (Olona et al., 2010; Holbrook et al., 2014, 2019; Flinchum et al., 2018a; Hayes et al., 2019; Gu et al., 2020). This combined approach allows for better modeling of subsurface water flow dynamics (Gu et al., 2020), comparison of slope aspect microclimates (Leone et al., 2020), and rock physics modeling of porosity (Holbrook et al., 2014; Hayes et al., 2019; Callahan et al., 2020; Gu et al., 2020; Grana et al., 2022). These studies are important advances and have helped to test and calibrate models of critical zone evolution, but they have documented only a fraction of the diverse combinations of topography, biota, lithology, and climate present across Earth's terrestrial surface.

In this study, we image critical zone structure through active-source seismic refraction surveys across a series of sedimentary ridges and valleys in the Mediterranean climate of the California Coast Ranges, USA. The site, Rancho Venada, is an ideal location to explore critical zone processes given its consistent bedding orientation, lack of complicating deformation features, and its striking contrast in vegetation density with slope aspect. Sedimentary

lithologies are understudied in critical zone literature, the vast majority of which involve granite, and Rancho Venada therefore provides a setting to examine the influence of bedding planes and of interbedded lithology on subsurface structure. Characterizing water storage dynamics in this setting is essential as Rancho Venada faces increased drought frequency (East and Sankey, 2020) and rainfall-triggered landslides (Nelson et al., 2017; Sanders et al., 2019; Handwerger et al., 2019). A 2018 drilling campaign established weathered material extending 11-17 m below ridgetops, and only 1-2 m below channels. Building on this previous work, we ask: 1) How does weathering, as expressed by bedrock fracturing and chemical alteration, vary with hillslope aspect? 2) What is the role of sedimentary bedding orientation in critical zone structure? 3) What is the water storage capacity of the weathered bedrock and how does this vary across the landscape? To respond to these questions, we perform a comprehensive comparison of seismic velocity with physical, chemical, and hydrologic properties measured through borehole analysis by Pedrazas et al (2021) and Hahm et al. (2022).

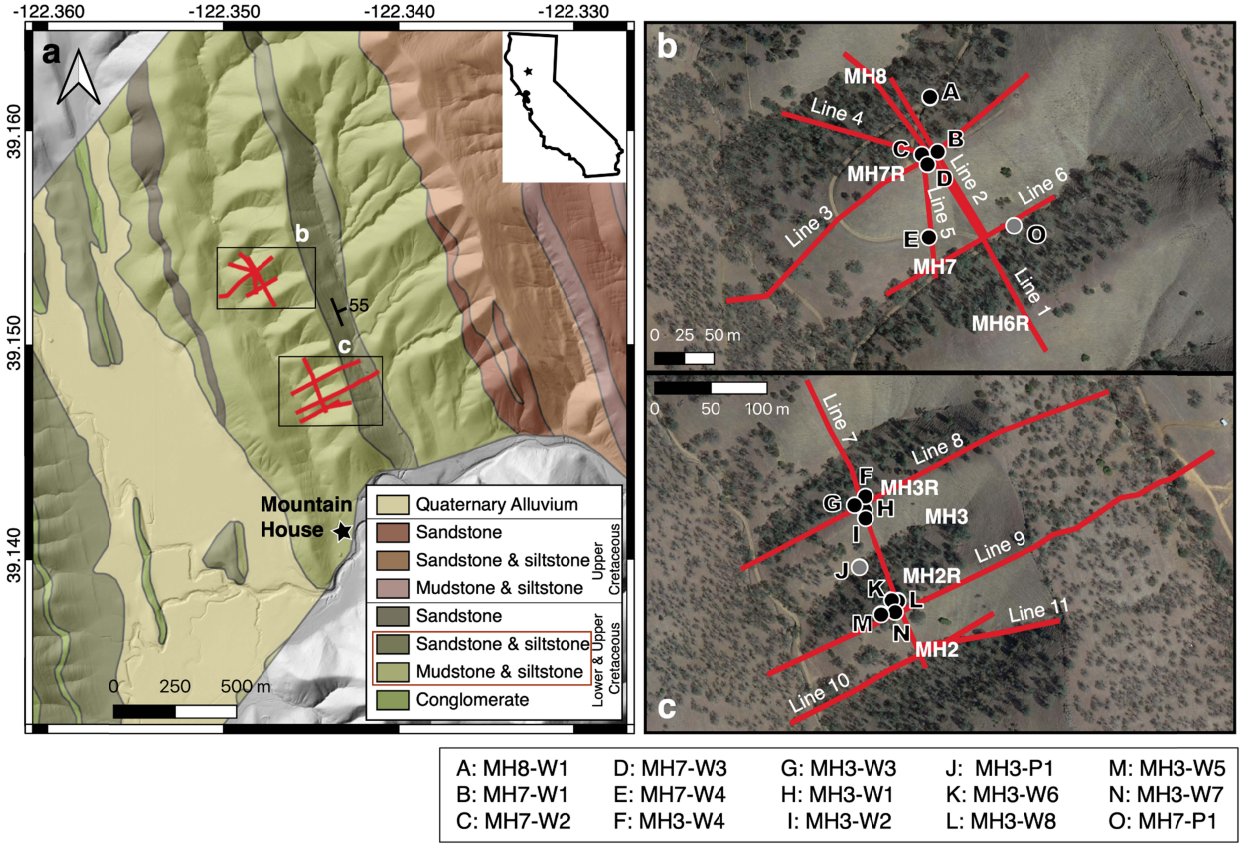

A: MH8-W1	D: MH7-W3	G: MH3-W3	J: MH3-P1	M: MH3-W5
B: MH7-W1	E: MH7-W4	H: MH3-W1	K: MH3-W6	N: MH3-W7
C: MH7-W2	F: MH3-W4	I: MH3-W2	L: MH3-W8	O: MH7-P1

Figure 1. Geologic map of the study location near Williams, California, USA (after Rich, 1971 and Nelson et al., 2017). The geologic units underlying our study hills are outlined in the red box in the legend. The black star in the inset map indicates the study site Rancho Venada. Inset **b** and **c** show the locations of the specific hills of interest and the contrasting tree density on north and south-facing slopes. For the naming convention, MH2 represents the 2nd channel from south, and MH2R represents the ridgetop north of the 2nd watershed. Red lines represent seismic survey lines 1-10. Black circles indicate locations of boreholes cored using a drill-rig, while gray circles were drilled using a Shaw backpack drill (Pedrazas et al., 2021). Letters A to O indicate the borehole number.

2. FIELD SITE

2.1 Geologic setting

The study site, Rancho Venada, is located 16 km west of Williams, California, USA, on the western border of the Sacramento Valley, and is lined with hills organized parallel to the strike of east-dipping turbidite beds (**Figure 1**). We focus on a ridge dissected by evenly spaced (~100-150 m) channels. The specific hills included in this study—referred to as MH2R, MH3R, and MH7R—are underlain by late Cretaceous bedrock of the Great Valley Sequence, composed primarily of thinly interbedded mudstone and siltstone, and capped with sandstone (**Figure 1**; Rich, 1971; Pedrazas et al., 2021). These units are separated from the deformed metamorphic Franciscan Complex by the Stony Creek Fault Zone to the west (Rich, 1971). Originally uplifted and tilted due to the subduction of the Farallon Plate below the North American Plate, Rancho Venada has been experiencing general northwest-southeast compression for the past 3-5 Ma (Atwater and Stock, 1998). There are no major faults or folds within these ridges, with only cm-to-meter-scale structures (monocline fold) observed (Harwood and Helley, 1987; Rich, 1971). The hills were formed at least ~1-2 Ma based on a channel incision rate of ~0.1 mm/yr (Pedrazas, et al., 2021). The regional climate is sub-humid with pronounced wet and dry seasons and a mean precipitation of 534 mm/yr (Hahm et al., 2022). Vegetation is primarily grassland and Blue oak-manzanita woodland, with a notable lack of trees on south-facing hillslopes and a higher vegetation density on the north-facing hillslopes (see **Figure 1b,c**).

2.2 Previous studies

Fourteen boreholes were drilled along three hills at Rancho Venada in November 2018 (Pedrazas et al., 2021). Three deep boreholes were drilled to the total relief of the hills: 47, 20, and 20 m for MH7R, MH3R, and MH2R, respectively. In this study, MH7 refers to the 7th channel north of the Mountain House (MH), and R refers to the ridgetop north of the channel. The drilling process involved augering, coring, and standard penetration tests to obtain blowcount rate (Pedrazas et al., 2021; ASTM, 2022). Blowcount rate is the number of blows necessary to advance a hollow core tube 6 inches into the ground, providing a measure of material strength. Shallower boreholes were augered to 6-9 m depth or drilled with a Shaw drill to < 2 m in the channels. All boreholes were sampled for elemental composition, and images were produced using an optical borehole imager (OBI) for each of the three deep boreholes to capture fracture and bedding density and orientation as well as color. Yellowness hue was calculated from these images, as a proxy for chemical weathering (following Holbrook et al., 2019). Matrix porosity was calculated from auger chips and pieces of the core and using the Accupyc Gas Pycnometer and GeoPyc Envelope Density Analyzer. Neutron count measurements were taken every foot by lowering the probe down each borehole until it reached the water table. These measurements were repeated every month over the course of 2 years to measure the relative seasonal water storage with depth (Hahm et al., 2022; **Figure 2c-f**). Drilling logistics and borehole measurements are described in detail in Pedrazas et al. (2021).

Borehole analysis highlighted three interfaces across the hillslopes: *Interface 1* as the soil - pervasively fractured material transition (i.e. soil to saprolite), *Interface 2* as the pervasively fractured - discretely fractured rock transition (i.e. saprolite to weathered bedrock), and *Interface 3* as the discretely - rarely fractured rock transition (i.e. weathered to fractured bedrock). Chemical analysis of the cores included using the mass transfer coefficient (τ), to track elemental changes as the parent material is weathered. The pyrite oxidation front is also

observed at a 6 - 7 m depth for all boreholes (**Figure 2a**). Matrix porosity for all sites ranges from 15-20% near the surface and drops to 10% within 5 m, and even lower to 5% by 24 m (Pedrazas et al., 2021). The MH3R (**Figure 2d**) and MH7R ridges display a large jump in blowcount rate, indicating an increase in material strength, at a 6-7 m depth, while MH2R shows a more gradual increase in blowcount rate. Neutron probe counts indicate dynamic seasonal rock moisture storage to a depth of 8-9 m (**Figure 2c**). Pedrazas et al. (2021) therefore propose the Interface 2 (saprolite-weathered bedrock) transition depths (MH7R: 6.5 ± 0.8 m, MH3R: 6.3 ± 0.8 m, MH2R: 7.5 ± 1.6 m; Pedrazas et al., 2021) based on the sharp increase in blowcount rate and the pyrite weathering front observed in each borehole. The saprolite above Interface 2 shows depletion of Mg, Na, and K, higher porosity, substantial fracturing, and storage of seasonally variable rock moisture. Yellowness hue, an indicator of chemical weathering, drops abruptly at a 17.5, 11, and 10.5 m depth for MH7R, MH3R, and MH2R, respectively. Pedrazas et al. (2021) define the Interface 3 (weathered- fractured bedrock) transition at the above depths based on yellowness hue and further decrease in fracture density.

Hydrologic analysis by Hahm et al. (2022) utilized a combination of remotely sensed soil moisture and evapotranspiration data, downhole rock moisture surveys, and oak sapflow and water potential measurements to monitor seasonal water storage and vegetation dynamics at Rancho Venada. During two drought years, the winter wet season did not replenish the subsurface storage capacity enough to recharge groundwater, discharge water as streamflow, or sustain trees, which exhibited lower sapflow and smaller leaf size. Their results suggest that Rancho Venada has a large water-holding storage capacity relative to the precipitation it receives during meteorological droughts, and is therefore precipitation-limited (in the sense of Hahm et al., 2019a). Repeat downhole neutron probe measurements across the 2019-2021 water years characterized seasonal rock moisture dynamics, and estimated volumetric water content to vary between 25-40% throughout the year.

Huang et al. (2021) conducted a seismic survey parallel to the bedding strike along the MH2-MH4 catchments at Rancho Venada in December 2019. In this study, we examine the same seismic refraction result (section 4.1.3) in comparison with data from drilling and nine additional seismic surveys to understand the deep critical zone structure.

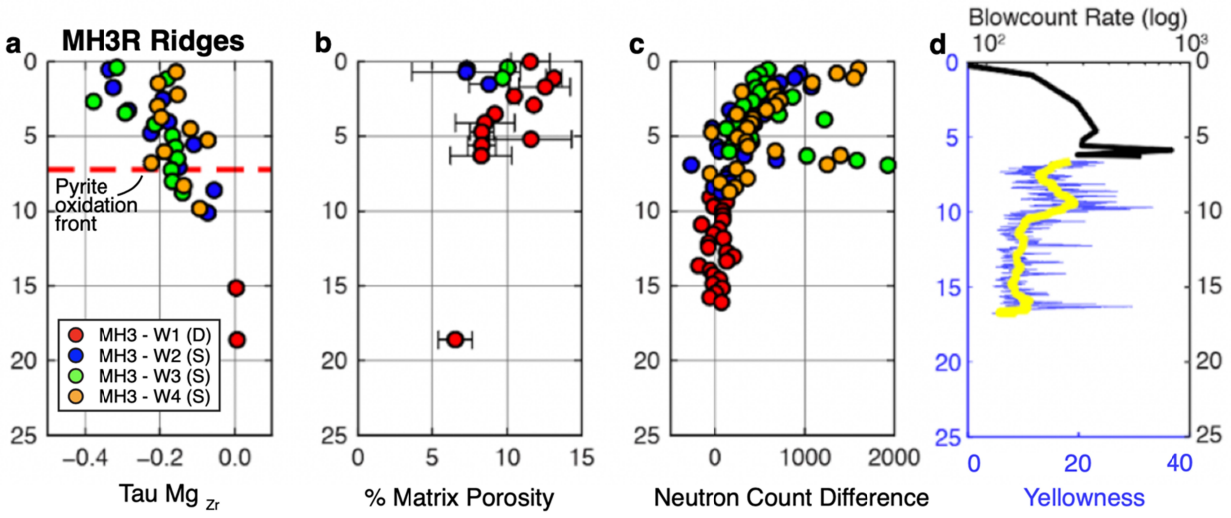

Figure 2. Borehole data for the MH3R ridgetop in Line 6 (see Figure 1 for location). Data is from Pedrazas et al. (2021) and excludes data below 25 m from MH3-W1. (**a**) Depletion of magnesium with

depth, relative to the parent material, with zirconium as the immobile element. It indicates depletion of magnesium (**Figure 2a**), sodium, and potassium towards the surface. Here we chose τ_{Mg} because it shows the most obvious depletion towards the surface. Other τ values are detailed in Pedrazas et al. (2021). The pyrite oxidation depth (from sulfur) shown as the red dashed line at 6.3 m. D and S represent deep and shallow boreholes, respectively. (**b**) Matrix porosity, (**c**) neutron count difference, highlighting where moisture storage in the borehole is variable, and (**d**) log blowcount rate on the upper x-axis. Yellowness hue (blue line) is shown on the lower x-axis. The yellow line represents the smoothed yellowness hue.

3. METHODS

3.1 Seismic refraction surveys and modeling

We conducted 11 active-source seismic refraction surveys: three lines oriented parallel to bedding (including one previously published bedding-parallel line, Line 7; Huang et al., 2021), six perpendicular to bedding, and two along the steepest descent of the north and south-facing hillslopes (**Figure 1**). Parameters of the seismic surveys are shown in **Table S1**. We used 14-Hz geophones and created sources at a 3-10 m shot interval using 5 to 7 kg sledgehammers on a metal plate, which were recorded using the Geometrics ES-3000 system and Geoid systems. For all lines except Line 9, the shot interval was one meter near borehole locations. We performed off-end shots 36-54 m away from the first geophone and after the last geophone for each survey. Locations along the seismic line were recorded with GPS to create an elevation profile of each seismic line using a digital elevation model (DEM) generated from an airborne lidar survey of Rancho Venada in 2017 (Dietrich, 2019).

We used the Geometrics PickWin software package to pick p-wave arrival times and the THB rj-MCMC inversion scheme from Huang et al. (2021) to generate seismic velocity models. For traditional inversion methods, smoothing is commonly used to regularize the inversion in order to reduce roughness coming from measurement errors. However, the smoothing parameter is normally set arbitrarily because measurement error from p-wave picking is generally unknown. The THB rj-MCMC method uses a probabilistic model to estimate measurement uncertainty (called hyperparameter) and whether measurement uncertainty propagates with source-receiver distance. THB rj-MCMC produces a posterior distribution of an ensemble of velocity models that can fit the p-wave measurements equally well, therefore we capture both the range of plausible solutions and the uncertainty associated with the model (Burdick and Lekic, 2017). The standard deviation of ensemble velocity can be calculated from the accepted models to indicate areas where the velocity has greater uncertainty (Huang et al., 2021). The THB method therefore allows for analysis of data uncertainty and explores model resolution along lateral distance and depth, which are important for assessing the reliability of seismic velocity images and interpretation of critical zone structure (**Figure 3**).

3.2 Borehole comparison and hillslope analysis

To compare borehole data to seismic velocity measurements, we created a vertical velocity profile for each borehole located within 10 m of a seismic survey. We examined the p-wave velocity corresponding to the interface depth ranges from Table 1 of Pedrazas et al. (2021). Several boreholes were imaged by more than one seismic line and therefore have multiple recorded velocities. We averaged the velocity at each interface across all borehole-velocity profiles of the same survey line orientation. Since the interfaces are not abrupt

boundaries, but transitional zones, we calculated the average velocity of the Interface 2 (saprolite to weathered bedrock transition) depth ± 1 standard deviation. Our result is a range of velocities over which we expect more rapid changes in material strength to occur. We then use this velocity zone to compare weathering structure across the three ridges. While borehole data is limited to one mid-slope location, we can calculate the depth to the bedding-parallel Interface 2 velocity range across the entire hillslope. We then compare the depth of this velocity range between north and south-facing hillslopes to examine aspect differences in rock weathering. To account for different lengths of hillslopes, we divide horizontal distance and depth by the hillslope length to examine normalized profiles. We do the same process for Interface 3 (weathered to fractured bedrock transition).

3.3 Porosity modeling

Matrix porosity (Φ_{matrix}) was measured from pieces of the core and reflects intra-grain pore space, ranging from > 20% at the surface to < 10% at a 10 m depth below ridges (Pedrazas et al., 2021). These measurements do not capture the total porosity which includes pore space associated with fractures, from processes like gravity unloading and tectonic loading. On the other hand, seismic waves from near-surface active source seismic surveys are generally sensitive to length scale in 10s of meters (e.g. Flinchum et al., 2022). In order to estimate a total bulk porosity (Φ_{total}) that is reflective of fracture and matrix pore space, and to obtain porosity values on a broader spatial scale, we apply a rock physics model to our seismic refraction data (e.g. Hayes et al., 2019, Holbrook et al., 2014, and Gu et al., 2020). This model requires knowledge of the material mineralogy, relative saturation, and a set of empirical parameters related to grain size and other sediment properties. While we have elemental analysis of samples from the cores (Pedrazas et al., 2021), we do not know the exact mineral composition at Rancho Venada. We assumed three mineral components based on a geologic map of the region (Rich, 1971), and then varied the percentage of each, with quartz: 20-50%, feldspar: 20-30%, and chlorite: 20-60%. This produces a range of bulk and shear moduli for the protolith. We then used the Hertz-Mindlin contact theory to calculate the dry bulk and shear modulus of the saprolite with shale or sandstone protolith, assuming a critical porosity of 0.4, contact points as 5, and an empirical parameter (*e*) as 5 (after Gu et al., 2020). Since saturation also contributes to the bulk modulus and we do not know relative saturation with depth, we vary water saturation between 0-100% and use Gasman's equation (Helgerud et al., 1999) to calculate the bulk and shear modulus of saprolite at different saturation states for each possible porosity value. With these bulk and shear moduli, we can then calculate seismic velocity using:

$$Vp = \sqrt{\frac{K_{sat} + \frac{4}{3}\mu_{sat}}{\rho_b}}\ , \tag{1}$$

where Vp, K_{sat}, μ_{sat}, and ρ_b are the seismic velocity, bulk modulus, shear modulus, and bulk density, respectively. We then compare Vp to the observed seismic velocity profile at each borehole. Since both bulk porosity and relative saturation are unknown, the best-fitting velocities present a tradeoff curve between porosity and saturation, where any point along the curve predicts the same Vp. By assuming 0% saturation, we can make a 1D profile of porosity with depth.

While we do not have absolute measurements of relative water content with depth, we can estimate relative changes in volumetric water content with depth using repeat downhole neutron probe surveys previously conducted at Rancho Venada (Hahm et al., 2022). Repeated neutron probe surveys capture variations in moisture storage over time. By observing the change in water content (Δθ) over multiple years, we can infer a minimum estimate of storage, and thus porosity, that is available at each depth. Porosity must be at least as high as Δθ. For MH7R, we calculated Δθ from 02/12/2019 to 09/01/2021 using combined measurements from MH7-W2 and MH7-W3. We binned the measurements to 1m depth intervals and calculated Δθ across the observation period after removing outliers. Wells MH3-W2, MH3-W3, and MH3-W4 were used for MH3R, and MH3-W6 and MH3-W7 were used for MH2R. The observation period for MH2R and MH3R was 11/15/2018 to 09/02/2021. Assuming that the matrix porosity is perennially saturated, then the seasonally dynamic rock moisture storage measured by the neutron probe represents additional porosity (e.g. from fractures), as opposed to porosity within the matrix (Φ_{matrix}). We can therefore estimate a minimum dynamic porosity ($\Phi_{dynamic}$) using,

$$\phi_{dynamic} = \Delta\theta + \phi_{matrix}, \quad (2)$$

that can be compared with the meter-scale modeled Φ_{total} from seismic refraction. $\Phi_{dynamic}$ represents a lower bound on Φ_{total}. Both Δθ and Φ_{matrix} were interpolated to 1m depth intervals so they could be added together.

4. RESULTS

4.1 Seismic velocity between ridges and channels

2D seismic images reveal changes in p-wave velocity (Vp) across the landscape. For all surveys, we mask out velocity past the ends of each line where no geophones are present. We additionally mask out regions where normalized smoothed raypath density is below 0.1 rays per model grid (using median filter with 5-pixel radius) and where coefficient of variation (CoV; standard deviation divided by mean velocity) > 30%. Low-velocity material is defined as Vp < 1000 m/s, mid-velocity as 1000 < Vp < 3000 m/s, and high-velocity as Vp > 3000 m/s. In this section, we report results of Lines 1, 6, 7, and 8. The results of Line 2-5 and Lines 9-11 can be found in the Supplementary Materials. THB rj-MCMC provides information about the overall performance of the inversion (**Figure 3**). This includes the root mean square (RMSE) misfit of the predicted p-wave arrival times of each Markov Chain in different iterations (**Figure 3a**), a noise hyperparameter that can objectively estimate data uncertainty (**Figure 3b**), a model misfit distribution of the mean velocity model with different source-receiver distance, the standard deviation of that distribution (**Figure 3c-d**), the p-wave arrival time model fitting to data of the mean velocity model (**Figure 3e**), and a normalized raypath density distribution of the mean velocity model (**Figure 3f**). For example, for MH7 the RMSE misfit starts to stabilize after ~$5x10^5$ iterations for all of the markov chains, implying further iteration of model parameters do not further improve the fitting, but instead can explore parameter distributions that can fit the data equally well (Huang et al., 2021). We find that the mean misfit of data (1.23 ms) is similar to the hyperparameter noise (~1.5 ms), suggesting a good balance of model parameters that do not under- or over-fit the data (**Figure 3b,c**).

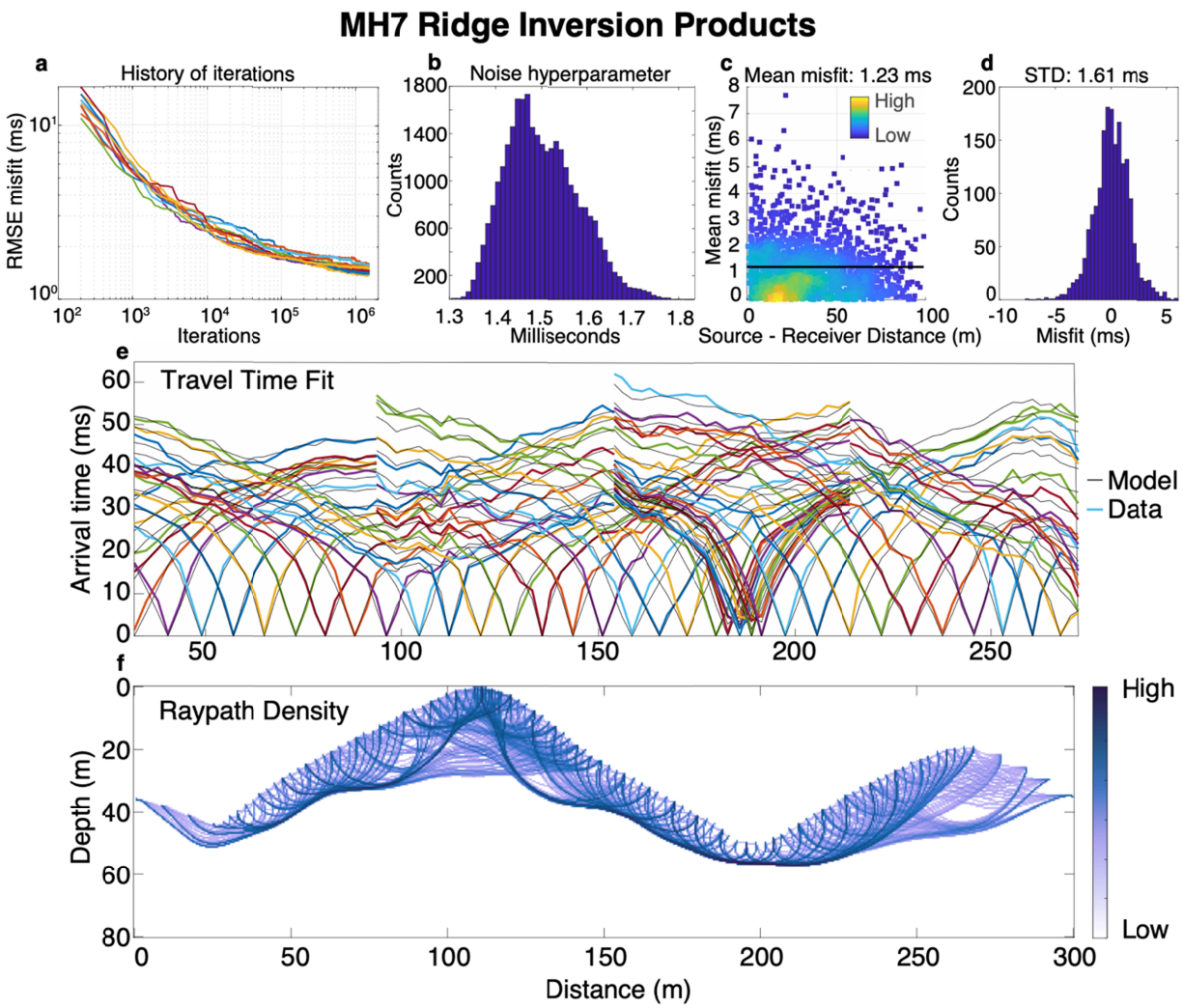

Figure 3. THB rj-MCMC products for Line 1. (**a**) RMSE misfit evolution in log-log scale. (**b**) Noise hyperparameter distribution after burn-in. (**c**) Mean misfit with source-receiver distance of the mean velocity model. (**d**) Standard deviation of the misfit in the mean velocity model. (**e**) Modeled travel time (black lines) and observed travel time (colored lines) of the mean velocity model. (**f**) Normalized raypath density of the mean velocity model.

4.1.1 MH7R bedding-parallel transect (Line 1)

Below the ridgetop (MH7R), uncertainty is higher (CoV > 30%) due to low raypath density. We therefore mask out much of the region and can only resolve 10 m below the ridgetop (**Figure 3ab, Figure 4b**). Below the hillslopes, we can reliably resolve depths up to 20 m, while we can only resolve 10 m at the channels due to a rapid increase of seismic velocity. Three boreholes (MH7-W1, MH7-W2, and MH7-W3) at MH7R are within 10 m of Line 1 (**Figure 1**).

Below channels (MH7 and MH8), higher velocities are present at shallow depths, while towards the ridgetops, velocities < 3000 m/s extend for over 20 m (**Figure 4a**). The highest 2D velocity gradients occur below the channels, where velocity increases from 400 m/s to 4000 m/s within 5 meters (**Figure 4c**). A >300 m/s/m gradient contour zone can be traced across the

hillslopes, suggesting a change in material strength within this high gradient zone. The 3000 m/s contour line does not mirror the surface topography at the ridgetop. However, we do not have deep enough ray paths to constrain whether Vp > 3000 m/s extend below the elevation of the channel (**Figure 4a**). A second survey line (Line 2 in **Figure 1b**) was conducted parallel to bedding across MH7R with twice as many geophones in efforts to obtain deeper ray paths and resolve velocity below the ridge (see **Figure S1**). Line 2 resolves deeper material below the hillslopes, reaching Vp > 3500 m/s above the elevation of the channel, but we were still unable to resolve structure below 14 m at the ridgetop, likely indicating a near constant seismic velocity below this depth.

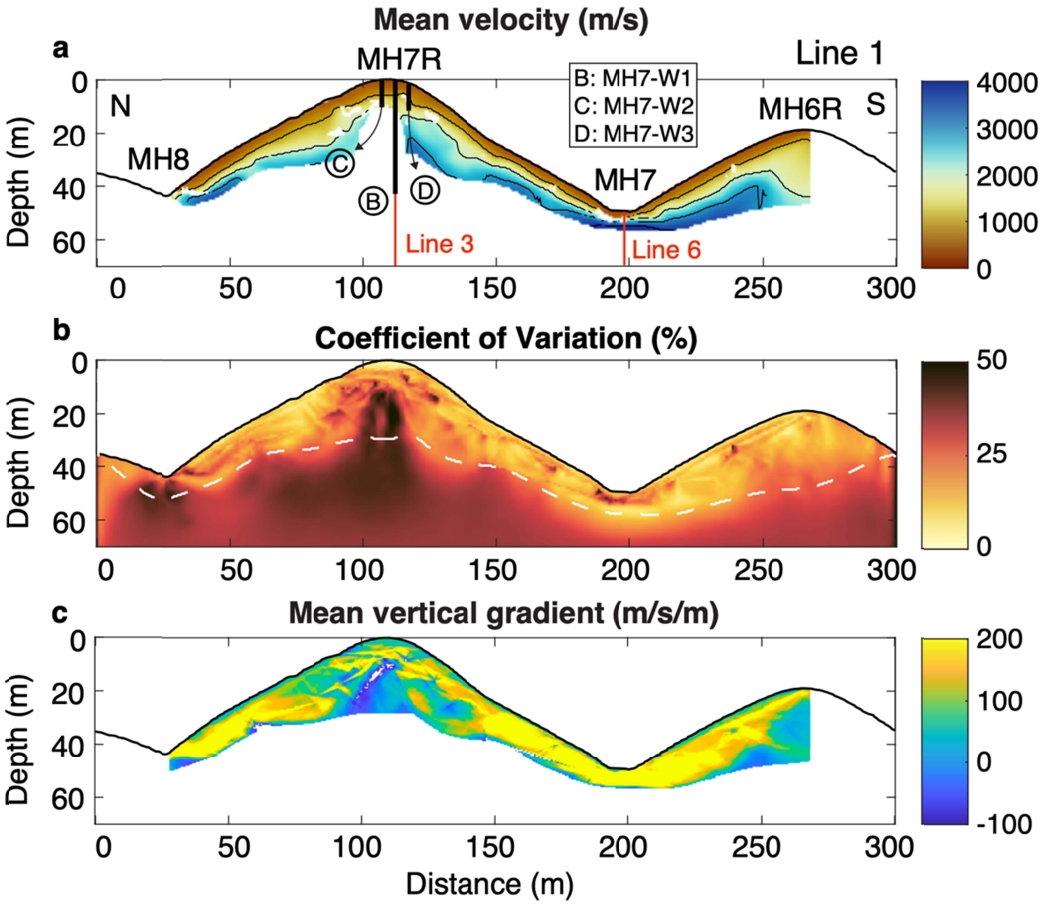

Figure 4. Results of Line 1 inversion using THB rj-MCMC (Huang et al., 2021). (**a**) Mean velocity model with contour lines at 1000, 2000, 3000, and 4000 m/s. The model is masked out where no geophones are present (edges of survey), below the deepest raypath, and where coefficient of variation (CoV; standard deviation/mean velocity) > 30%. Vertical dashed lines highlight the locations of boreholes within 10 m of the survey line. From north to south, these include boreholes MH7-W2, MH7-W1, and MH7-W3 for Line 1. The orange vertical line indicates the intersection point of Lines 1 and 3. (**b**) Percent CoV with the deepest raypath as the white dashed line. (**c**) Mean vertical velocity gradient (m/s/m), masked out where there are no geophones and below the deepest raypath.

4.1.2 MH7 channel (Line 6)

Much of the shallow velocity profile for Line 6 has low raypath density due to a high velocity contrast at shallower depth, which does not allow for deep raypaths without a longer source-receiver distance. Since weathering transitions happen at shallow (< 5 m) depth below the channel, we show an interpolated version of the mean velocity (**Figure 5a**). Vp rapidly reaches 3000 m/s within 1-5 m of the surface, with a slightly shallower high gradient zone farther east. The seismic survey configuration does not have sensitivity below ~10 m depth. Velocity for Line 6 agrees with Line 1 at their intersection (red line at 90 m). The MH2 channel (Lines 10-11) is shown in **Figure S6** and reaches high velocities within 6m of the surface on the western side, and within 2m further east.

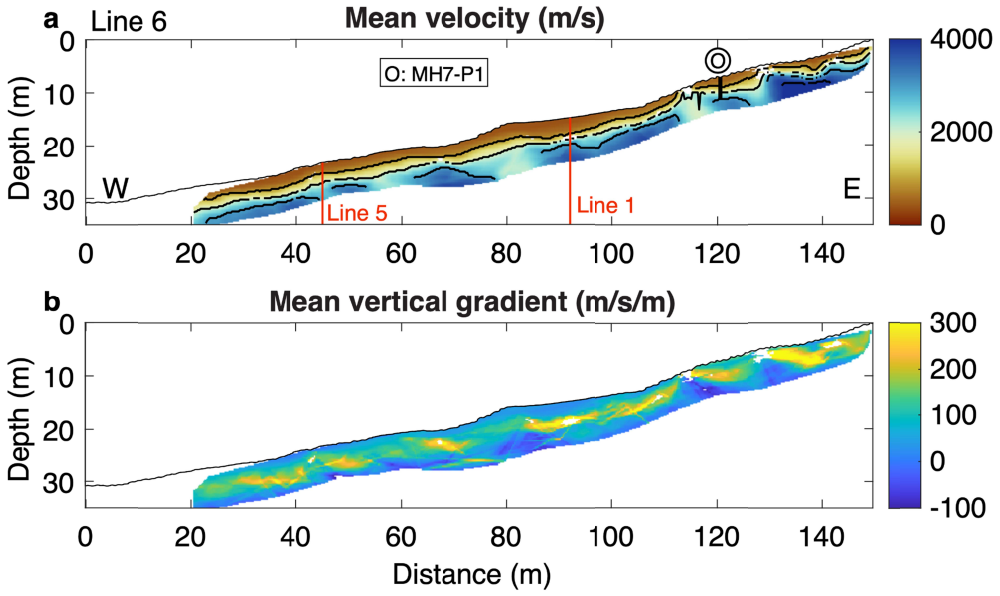

Figure 5. Results of Line 6 inversion. (**a**) Interpolated mean velocity model with contour lines at 1000, 2000, 3000, and 4000 m/s. The model is masked out below the deepest raypath and where CoV > 40%. Black dashed lines highlight the locations of boreholes within 10 m of the survey line. Red lines indicate the intersection points with Line 5 (45 m) and Line 1 (90 m). (**b**) Mean vertical velocity gradient (m/s/m).

4.1.3 MH3R and MH2R bedding-parallel (Line 7)

Line 7 is the same transect shown in Huang et al. (2021). Four boreholes at MH3R are within 10 m of Line 7: MH3-W1, MH3-W2, MH3-W3, and MH3-W4. Results of this survey indicated an upslope-thickening weathering profile for MH3R, with low-velocity (< 1000 m/s) material extending 5 m below the ridge and <1 m below the MH3 channel (**Figure 6a**). Three boreholes at MH2R are within 10 m of Line 7: MH3-W5, MH3-W6, and MH3-W7. The MH2R ridgetop presents a different velocity structure than its neighbor. Low-velocity material extends to a similar depth of 5-6m, but mid-velocity material extends further below the ridgetop than at MH3R. Velocities at MH2R increase gradually, remaining at 2000 m/s even at depths of 20 m below the ridge. The 3000 m/s contour is barely reached within the resolvable depth range.

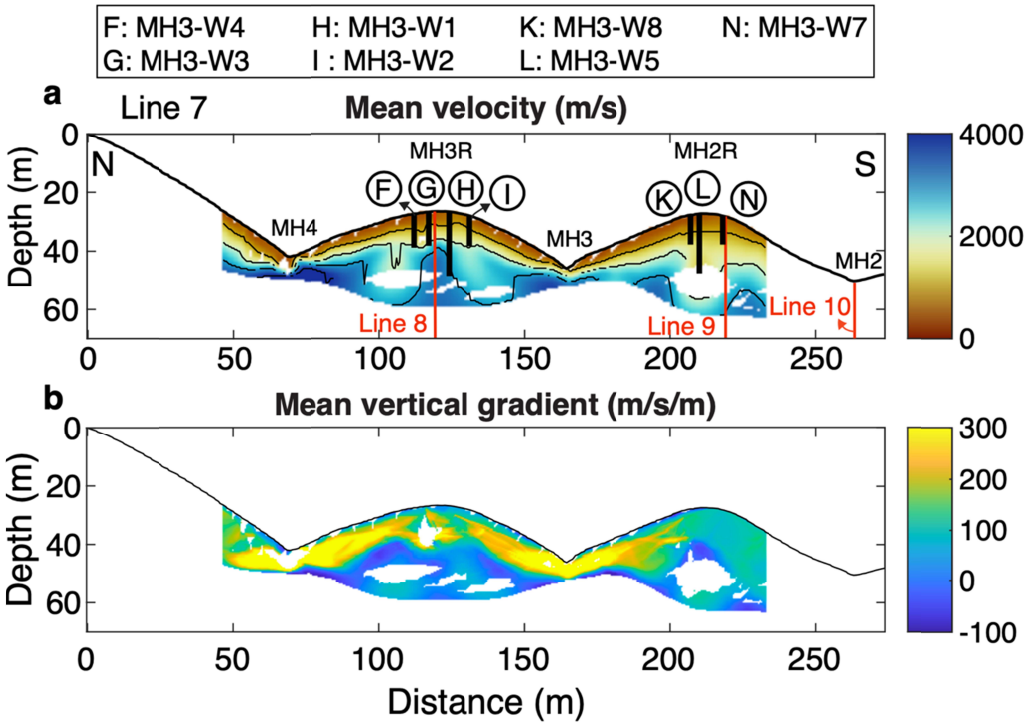

Figure 6. Results of Line 7 inversion. (**a**) Mean velocity model with contour lines at 1000, 2000, 3000, and 4000 m/s. The model is masked out below the deepest raypath and where CoV > 30%. Black dashed lines highlight the locations of boreholes within 10 m of the survey line. From north to south, these include boreholes MH3-W3, MH3-W4, MH3-W1, and MH3-W2 on MH3R, and MH3-W6, MH3-W5, and MH3-W7 on MH2R. The orange vertical lines indicate the intersection points of Line 7 with Lines 8 (MH3R) and Line 9 (MH2R). (**b**) Mean vertical gradient (m/s/m). Note the gradient color scale ranges from -100 to 300 m/s/m.

4.1.4 MH3R perpendicular (Line 8)

Three boreholes at MH3R are within 10 m of Line 8: MH3-W1, MH3-W3, and MH3-W4. The velocity contours are surface-parallel for most of the west-facing slope, though the 3000 m/s contour is more variable (**Figure 7a**). The east-facing slope has a highly variable thickness of weathered material, with Vp > 2000 m/s reached at the surface near the ridgetop, and at > 25m depth towards the east channel. The shallow high-velocities east of the ridge correspond to the location of the east-dipping sandstone cap that tops each ridge. While the structure of east and west-facing slopes are different, there is not a consistent difference in weathered zone thickness (**Figure S12**). Bedding-perpendicular Line 9 also reveals subtle variations in velocity structure that may relate to lithologic contrasts (**Figure S5**), but the overall east and west-facing structures do not appear to differ dramatically. All bedding-perpendicular lines indicate largely surface-parallel weathered material that thins at the channel and thickens at the ridge.

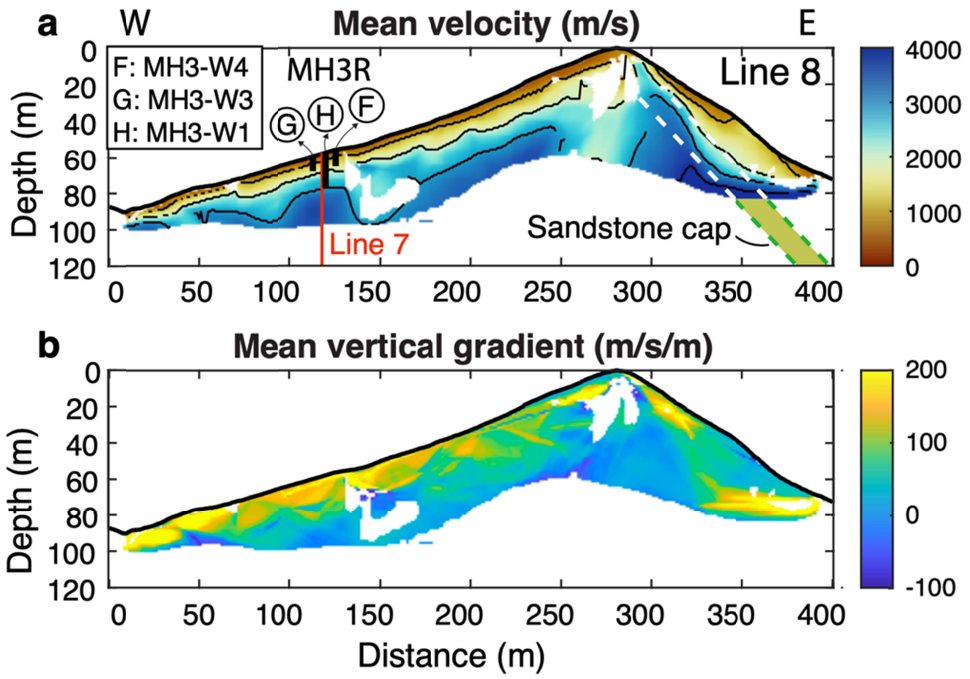

Figure 7. Results of Line 8 inversion using THB rj-MCMC. (**a**) Mean velocity model with contour lines at 1000, 2000, 3000, and 4000 m/s. The model is masked out below the deepest raypath and where CoV > 30%. Black dashed lines highlight the locations of boreholes within 10 m of the survey line. From west to east, this includes boreholes MH3-W4, MH3-W1, and MH3-W3. The orange vertical line indicates the intersection point with Line 7. The white and green dashed lines and SS represent the sandstone capstone. (**b**) Mean vertical gradient (m/s/m).

4.2 Borehole and seismic velocity comparison

We do not attempt to analyze the soil-saprolite boundary (Interface 1 at 0.3-0.5 m, Pedrazas et al., 2021) using seismic refraction, as the relatively low seismic source frequency from hammer shots (typically 20-30 Hz) and p-wave picking uncertainty do not allow us to capture submeter structure. Using seismic refraction data, we can delineate deeper interfaces using a velocity contour, or the peak vertical velocity gradient. Here we present the results of both. Material above the Interface 2 depth (pervasively fractured saprolite) gradually increases in Vp from 400-1000 m/s. The average Vp across the borehole-defined Interface 2 depth range for all ridges is 1284 ± 203 m/s (**Figure 8**). For each ridge, the Interface 2 Vp varies with the orientation of the seismic line relative to bedrock bedding, with bedding-perpendicular lines often fastest. Uncertainty in the Interface 2 depth from borehole data also adds to the velocity range. Material below the Interface 2 depth (weathered bedrock) is generally 1300-2000 m/s. Average velocity corresponding to the Interface 3 depth is 1973 ± 435 m/s across all lines. Vp at Interface 3 differs significantly between the three ridges (**Figure 8**). Interpretation of Interface 3 from the borehole is based primarily on a decrease in yellowness hue with depth (inferred as a decrease of chemical weathering) and a decrease in fracture density (Pedrazas et al., 2021). However, the different Vp ranges for Interface 3 between ridges suggests these borehole changes may not map onto a specific velocity contour.

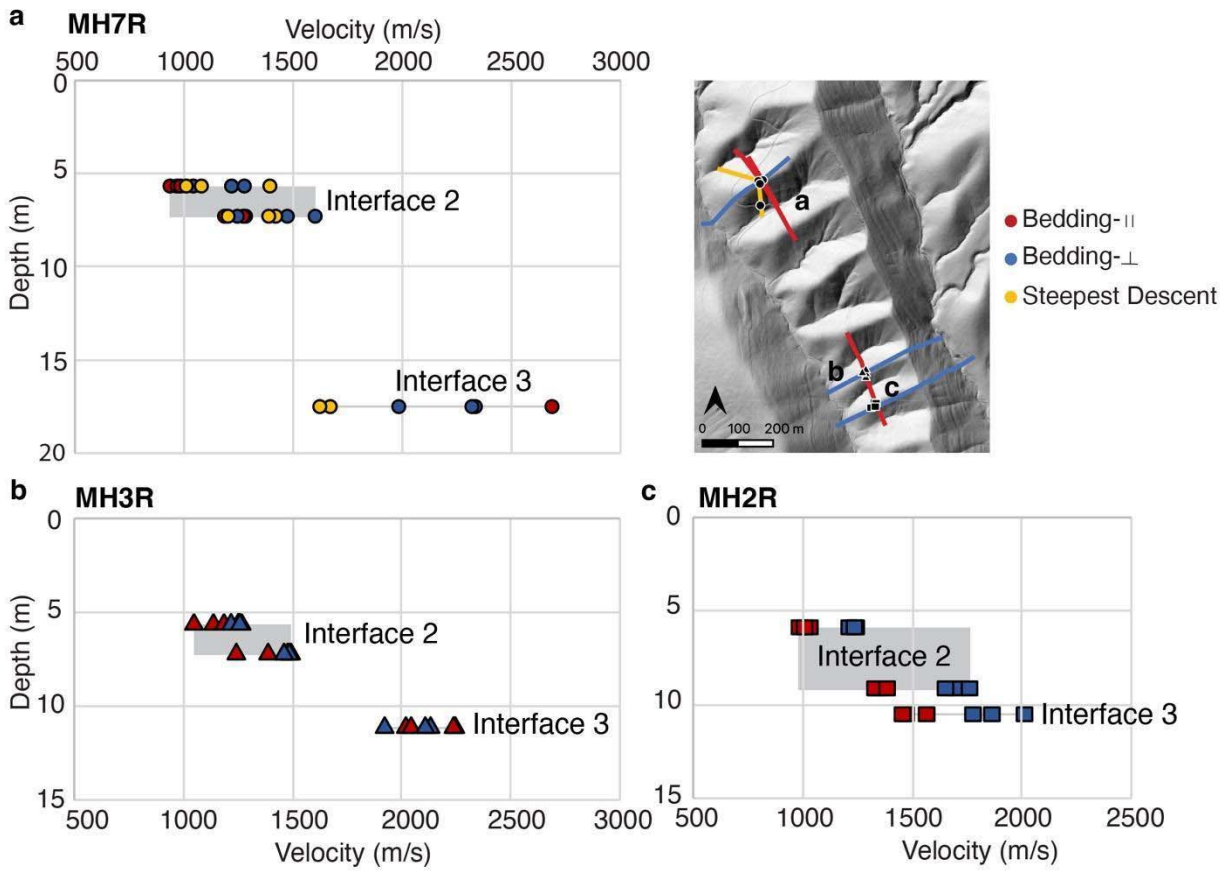

Figure 8. Seismic velocity at borehole interfaces 2 and 3 identified by Pedrazas et al. (2021) for (**a**) MH7R, (**b**) MH3R, and (**c**) MH2R. An upper and lower depth bound is plotted for Interface 2 based on the depth standard deviation from Pedrazas et al. (2021). Marker colors indicate the survey line orientation.

The maximum vertical velocity gradient captures the fastest increase of Vp with depth, which may be comparable to borehole interfaces. However, vertical velocity gradient does not exhibit a clear peak that can be easily traced across a hillslope. Rather, a zone of high gradient is observed in all profiles (**Figures 4c, 5b, and 7b**). At the MH7R ridgetop, we see a zone of high velocity gradient from around 3 m to 7–10 m depth (**Figure 9b**). At MH3R, this high gradient zone appears as 2 peaks centered at 3 m and 10 m. For MH2R, the high gradient zone is gradual without a clear peak, stretching from 2–12 m. There is not a clear relationship between velocity gradient and borehole property gradients (colored boxes in **Figure 9b**), but the most rapid changes in borehole properties do occur within the highest velocity gradient zone (~3–13 m) for each survey. Borehole transitions such as the increase in blowcount rate occur more gradually for MH2R (Pedrazas et al., 2021), consistent with its much lower velocity gradient.

Orientation of the seismic lines also influences the gradient structure. Across all three ridges, bedding-parallel lines have more pronounced peak gradient features, and bedding-perpendicular lines show a more consistent lower gradient, reflective of a more gradual increase in velocity (see **Figures 4c and 6b vs. Figure 7b**). It is difficult to distinguish Interfaces 2 and 3 using the velocity gradient. Rather, a relatively high-gradient zone, across which borehole properties change most dramatically, spans both interfaces.

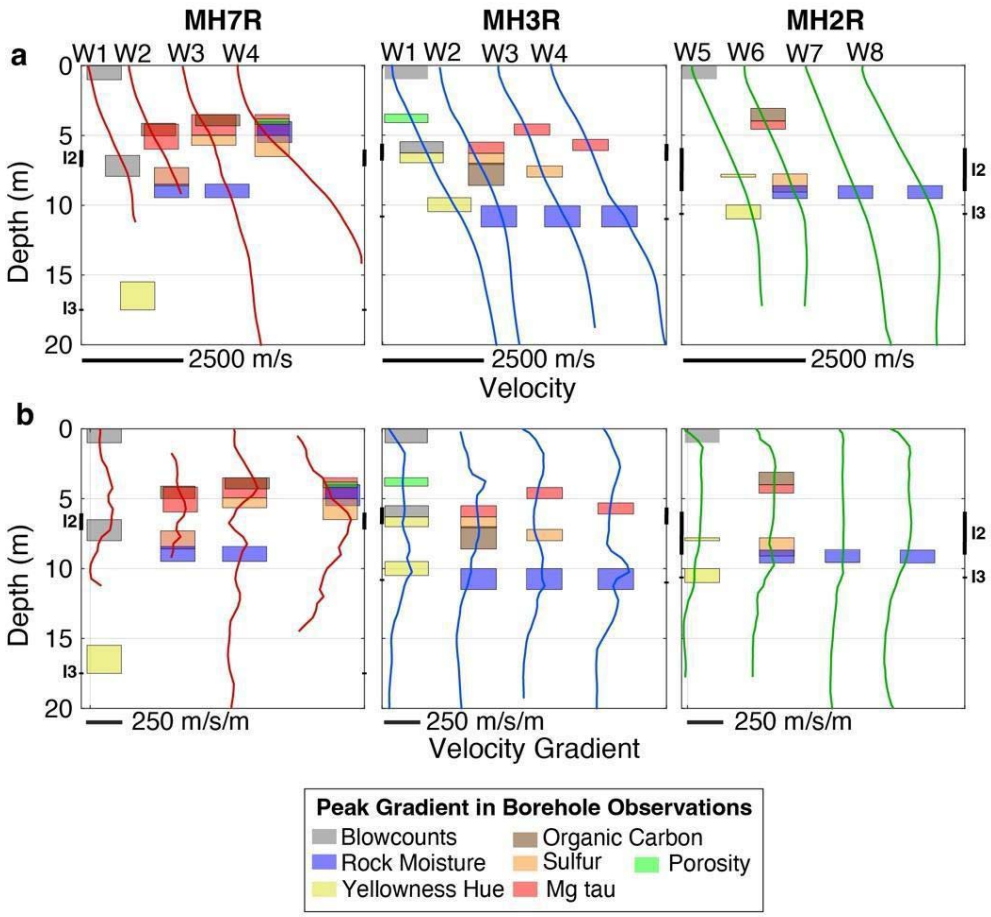

Figure 9. Velocity (a) and velocity gradient (b) profiles for each borehole across the three ridges. Each 1D profile represents the velocity and velocity gradient at each borehole averaged across all seismic line orientations. Colored boxes represent depth ranges where the vertical gradient of each borehole property is highest. Interface 2 (I2) and Interface 3 (I3) depths are shown on the edge of each plot (from Pedrazas et al., 2021). Only the deep boreholes MH7-W1, MH3-W1, and MH2-W5 have observations of blowcount rate and yellowness hue. The absence of a data type for a given profile indicates there were no sharp changes in that property with depth. The x-axis is stretched to space out each borehole, and a scale bar is shown for velocity and velocity gradient.

4.3 Hillslope analysis

To examine aspect-dependency in the subsurface, we compare the depth to the saprolite-weathered bedrock transition (Interface 2, 1284 ± 203 m/s) and weathered-fractured bedrock transition (Interface 3, 1973 ± 435 m/s) on sets of north-facing and south-facing hillslopes that share the same ridge or the same catchment. **Figure 10** shows the depth to Interface 2 with distance from the ridge along a straight-line transect. For all hillslopes, the saprolite layer thickens towards the ridge, and the depth to the base of the saprolite appears nearly identical on north and south-facing slopes, though it is variable from channel to ridge (**Figure 10a,c**).

Averaged depths to the 700 m/s, 1284 m/s (Interface 2 contour), 1973 m/s (Interface 3 contour), 2500 m/s, and 3000 m/s velocity contours present an inconsistent relationship between aspect and velocity, with the average south-facing depth sometimes shallower and

sometimes identical to north-facing slopes. When the Interface 2 depth is normalized with distance from the ridge (**Figure S8**), the MH7 south-facing slope does appear to have a shallower Interface 2 depth than the MH7 or MH8 north-facing slopes. However, at MH2, the normalized south-facing slope has a greater Interface 2 depth. Normalized average depth to velocity contours similarly shows shallower weathering depth on the MH7 south-facing slope, but deeper or identical weathering depth on the MH2 south-facing slope (**Figure 10**). Through combined analysis of borehole data and geophysics, we find no consistent difference in saprolite thickness with slope aspect for our surveyed ridges. This appears to be true for slopes within the same catchment (i.e., MH7 S and MH7 N), and for slopes sharing the same ridge (i.e., MH7 S and MH8 N).

We also compared Interface 2 depth between the MH8 north-facing and MH7 south-facing slopes along the steepest descent survey orientation (Lines 4 and 5; **Figure S7**. The steepest-descent profiles also do not demonstrate clear differences in Interface 3 depth between north-facing and south-facing slopes, although the Interface 3 depth does appear shallower below the MH7 south-facing slope in the mid-slope position (**Figure S9c,d**).

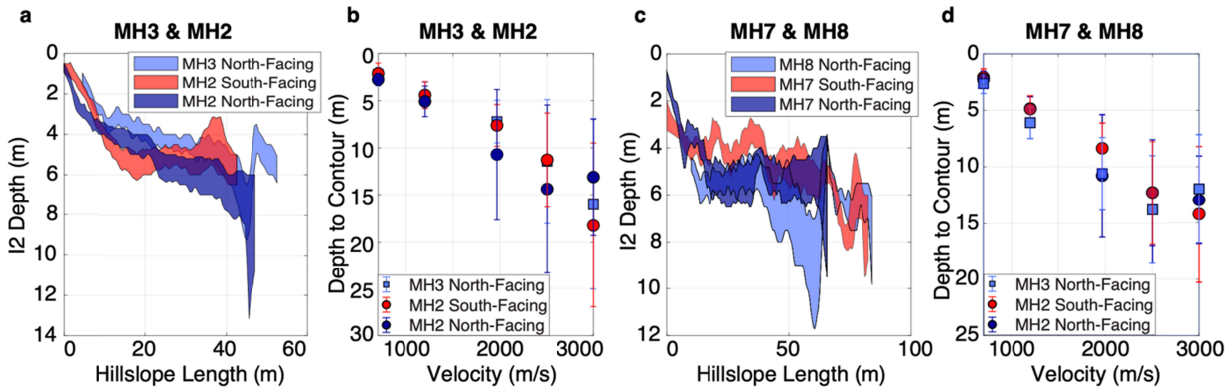

Figure 10. Comparison of weathering thickness on north- versus south-facing hillslopes for Line 6 (a-b), and Line 1 (c-d). Depth to Interface 2 (I2; saprolite-weathered bedrock) with hillslope length (**a,c**) is shown based on the I2 velocity range (1284 ± 203 m/s velocity contours). Average depths to various velocity contours are shown in (**b, d**), including the average Interface 2 velocity contour (1284 m/s) and average Interface 3 velocity contour (1973 m/s).

4.4 Trade-off between porosity and saturation

4.4.1 1D porosity and saturation at MH7

Following Section 3.3, our rock physics model indicates a tradeoff between relative saturation and porosity that can predict the same seismic velocity measured at depth. We varied the mineral composition between quartz, feldspar and chlorite, but we did not consider clay at the top few meters depth in the porosity modeling and may have overestimated porosity near the soil-saprolite transition zone if there is presence of higher clay mineral content. However, the relative amount of each mineral component does not have a large influence on porosity (**Figure 11a**; Callahan et al., 2020). Therefore, while we have not included all possible mineral components (i.e. there is > 1wt% organic carbon noted in Pedrazas et al., 2021), mineral composition is likely only a small source of error in the porosity estimate. Similarly, we do not

take into account the capillary forces in the unconsolidated zone at shallower depth, which may impact the modeled porosity near-surface (Solazzi et al., 2021).

The rock physics model applied at 1 m and 6 m depth (**Figure 11a**) indicates that, below ~40%, changes in saturation do not affect the modeled total porosity (Φ_{total}). On the other hand, small increases in saturation > 40% necessitate dramatic increases in porosity to explain the same velocity observation. Since precise measurements of saturation along depth are absent and shallow depths are unlikely to have saturation greater than 40% in August (5 months into the dry season) when our seismic survey was performed, we assume relative saturation is 0% for the whole depth profile. Although 0% saturation is also incorrect, the porosity estimate is insensitive to saturation values when saturation is less than 40% (**Figure 11a**).

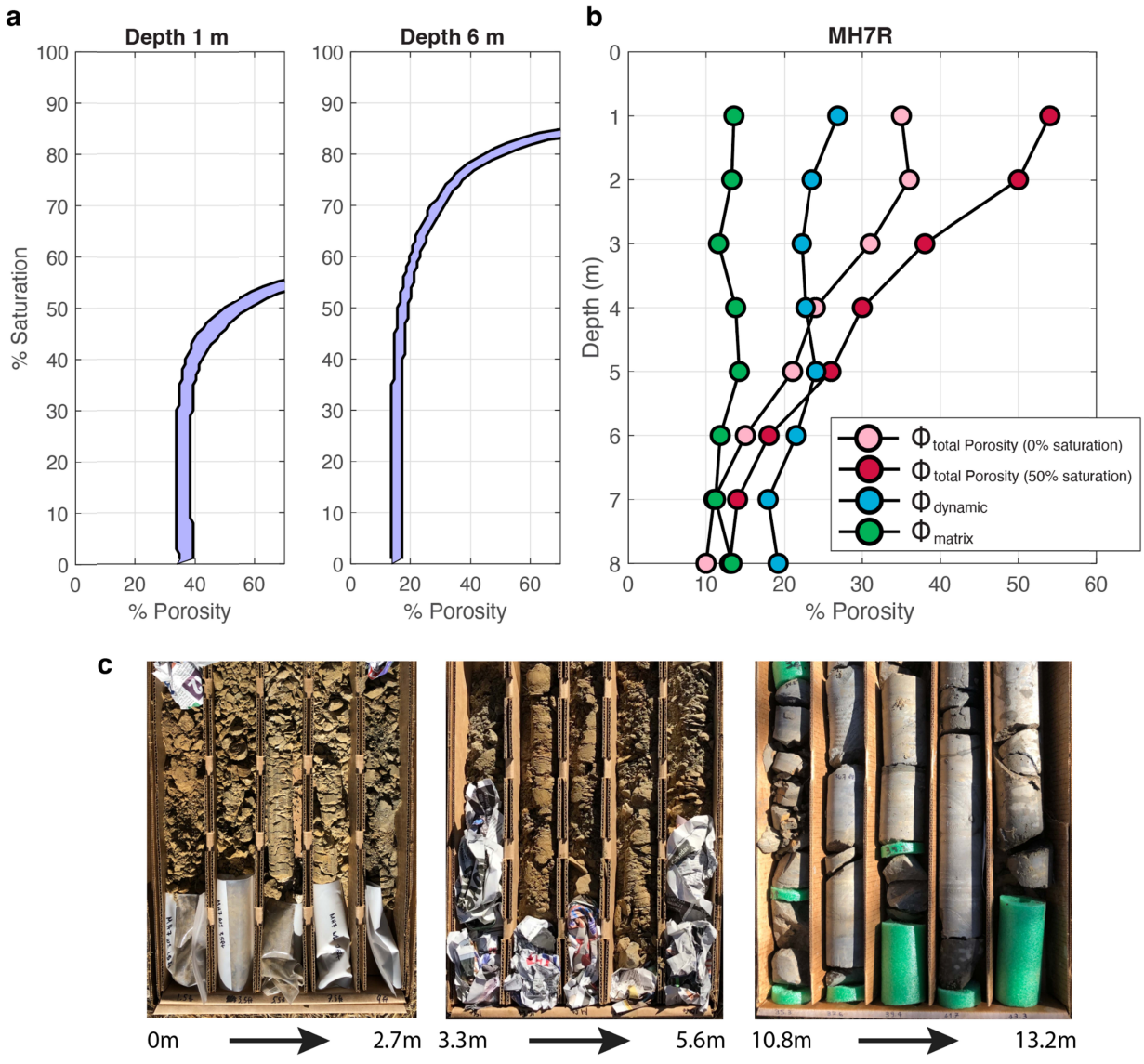

Figure 11. 1D rock physics model at MH7R (Line 1, a). (a) Tradeoff between saturation and porosity at MH7R at different depths based on the rock physics model using seismic refraction. Each point along the

curve represents a porosity/saturation value that predicts a nearly identical (< 1% difference) Vp at that depth. The width of the purple shaded area represents variation within the assumed mineral composition (i.e. 20% quartz, 30% feldspar, 50% chlorite, versus 30% quartz, 50% feldspar, 20% chlorite, etc.). (**b**) Porosity with depth from the rock physics model (Φ_{total}) based on the average velocity profile across all wells at MH7R. Measured matrix porosity (Φ_{matrix}) from cores at MH7-W1, MH7-W2, and MH7-W3, interpolated to a 1m depth is shown in green. The dynamic porosity ($\Phi_{dynamic}$) is based on neutron probe measurements at MH7-W2 and MH7-W3, with outliers removed and also interpolated to 1m depth. (c) Core photos along different depths that show change of fracture density from shallow to greater depth. Note samples shallower than 6 m depth are highly fractured and chemically weathered.

Matrix porosity (Φ_{matrix} in **Figure 11b**) measured from core samples is consistently < 15% for MH7. Matrix porosity does not account for fractures, which we know to be pervasive in the upper 6 m (Pedrazas et al., 2021). The dynamic porosity ($\Phi_{dynamic}$ in **Figure 11b**; see Equation 2) ranges from > 25% at a 1m depth to ~17% at a 7 m depth. If we assume the matrix is perennially saturated, $\Phi_{dynamic}$ represents a lower bound for the total porosity. Finally, the modeled total porosity (Φ_{total}) ranges from 35% at a 1 m depth to 9% at a 8 m depth, assuming 0% saturation (**Figure 11b**).

Total porosity (Φ_{total}) rapidly decreases between 2-3m and 5-6m depth, and then stabilizes below 6m. At ~5-6m depth, the modeled Φ_{total} is less than $\Phi_{dynamic}$. This depth corresponds with the Interface 2 (saprolite-weathered bedrock) boundary, where the core changes from pervasively to discreetly fractured (**Figure 11c**). Total porosity for MH3R and MH2R are shown in **Figures S10 and S11**, respectively, and similarly show Φ_{total} ranging from 30-35% at the surface to 10% by 8 m depth. MH2R has higher Φ_{total} in the upper 6m than MH3R, and a more gradual change in porosity with depth, consistent with the deeper low-velocity material observed at MH2R in **Figure 6**.

4.4.2 2D porosity at MH7

The rock physics model can also be applied on a 2D scale to examine the landscape porosity distribution across the north and south facing hillslopes. 2D models show the most pronounced decrease in porosity occurs within the saprolite layer (< 6 m depth, **Figure 12**). Below this depth, porosity is low and only decreases gradually. The mean porosity models represent the average of porosity estimated using varied percentages of feldspar, quartz, and chlorite (see Section 3.3). To construct a 2D model of bulk porosity, we assumed saturation was 0% (see Section 4.4.1). Assuming a different 2D saturation model would change the results of our model, particularly at shallow depths (**Figure 11b**). However, when saturation is low (< 40% and 50% at 1 m and 6 m depth, respectively), variation in the saturation model does not have a dramatic effect on modeled porosity (**Figure 11a**). The 2D model reveals there is heterogeneity in total porosity across each hillslope.

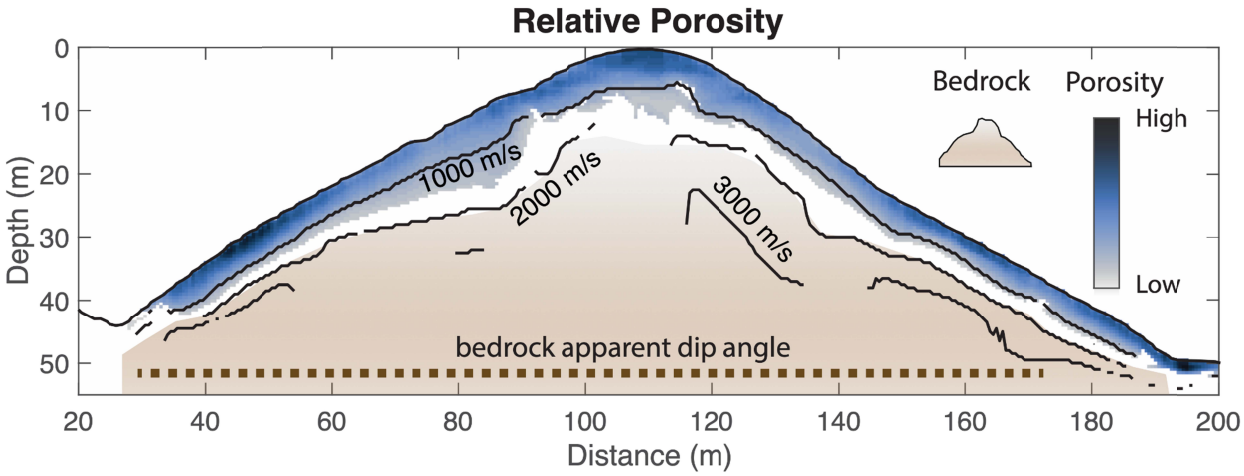

Figure 12. 2D relative total porosity model of the MH7R hill (based on seismic line 1). Light to dark blue colors represent an increase of porosity. The light brown color represents bedrock location, and the dashed line indicates apparent dip of the bedrock. The contour lines are the seismic P-wave velocity (Vp). The rock physics model was applied to the 2D velocity model, with velocity > 1500 m/s masked out.

5. DISCUSSION

5.1 Borehole and seismic velocity comparison

Seismic refraction is a useful tool to determine broad scale subsurface structure by identifying transitions in P-wave velocity (Vp) that can correspond to rock properties associated with weathering. However, seismic refraction is not expected to perfectly capture borehole-inferred properties since it is sensitive to larger spatial scales (meter-scale; Flinchum et al., 2022), whereas the borehole diameter is 6.35 - 12.7 cm and has cm-level sampling resolution for some measurements (Pedrazas et al., 2021). Vp is a measurement of bulk material strength that depends on lithology, porosity, moisture content, and chemical weathering. Several studies have shown good agreement between Vp and rock strength or fracture density (e.g. Lee and de Freitas, 1990; Clarke and Burbank, 2011; Flinchum et al., 2018a; West et al., 2019; Holbrook et al., 2019), as well as chemical mass loss (Gu et al., 2020).

Seismic refraction surveys at Rancho Venada capture a critical zone structure that closely matches the borehole-derived structure presented by Pedrazas et al. (2021). Material with Vp < 1284 m/s is interpreted as saprolite, consistent with other studies that find saprolite Vp < 2000 m/s (Befus et al., 2011) or < 1200 m/s (Flinchum et al., 2018a; Leone et al., 2020). The core within this zone is “pervasively fractured,” oxidized, and mechanically weak (Pedrazas et al., 2021). An increase in vertical velocity gradient occurs towards the bottom of the saprolite layer, marking a gradual transition to weathered bedrock. From the 1284 m/s contour, and the onset of the high gradient zone, we can determine the thickness of the saprolite across the landscape as 0 – 2 m thick at the channels, then increasing in thickness with lateral distance from the channel. It remains ~4-6 m thick under most of the hillslope and thickens only slightly approaching the ridgetop (**Figure 10a,c**). Saprolite thickness is nearly identical between ridges, despite a 25 m difference in relief from MH7R to MH3R and MH2R.

Below the saprolite layer, Vp increases from ~1200 to 2000 m/s generally in less than 10 m. This Vp range is variably thick across the landscape and is inferred to be weathered bedrock based on the presence of open, oxidized fractures (Pedrazas et al., 2021). Below this, the core exhibits a sudden decrease in yellowness hue and decrease in fracture density from “discreetly” to “rarely” fractured (**Figures 2 & 9**; Pedrazas et al., 2021). The bottom of the weathered bedrock is also upslope-thickening (**Figure S9**).

Velocity below the weathered bedrock increases gradually from 2000 to > 3000 m/s. The core in this depth range is rarely fractured, and fractures present are closed and unoxidized (Pedrazas et al., 2021). The gradual increase in Vp may be due to further reductions in fracture density with depth and an increase of overburden. When porosity is low, even a < 5 % decrease in crack volume can increase Vp by 1000 m/s in granites (Flinchum et al., 2022). Unweathered, unfractured bedrock is more likely to be reached at ~20 m depth where velocities reach 3000 m/s and velocity gradient approaches zero. Several studies use 4000 m/s as the bedrock velocity contour (Befus et al., 2011; Holbrook et al., 2014; Gu et al., 2020), however 3000 m/s is still within the expected range for unweathered sedimentary bedrock with 10% porosity (Eberhart-Phillips et al., 1989; Mavko 2009; Dvorkin et al., 2021). A collection of Vp measurements from laboratory and field settings show that clay-rich rocks commonly have a fresh bedrock velocity between 2000 - 4000 m/s (Lee, 2018). Velocity from the channel surveys, which should be relatively fresh, are mostly < 4000 m/s (**Figures 5 & S6**). All of our surveys therefore reach unweathered, rarely fractured bedrock at or above the channel elevation, and we do not see topography of the weathering front that systematically mirrors surface topography as expected for a highly stressed tectonic environment (Moon et al., 2017).

The transition from saprolite to weathered bedrock (Interface 2), from weathered to fractured bedrock (Interface 3), and from fractured to unfractured bedrock are difficult to distinguish as separate interfaces using velocity contours or the vertical velocity gradient. In particular, the seismic velocity at interface 3 ranged between 1600 m/s and 2700 m/s for MH7R, 1900 m/s and 2300 m/s for MH3R, and 1400 m/s and 2000 m/s for MH2R, which are not consistent across different ridges (**Figure 8**). As a result, using absolute seismic velocity to identify interface 3 may not be reliable. While this may be due in part to variability in velocity structure between different survey line orientations, the lack of a clear distinction between interfaces is also visible in the borehole data. For example, the depth of dynamic rock moisture storage from neutron probe counts at 8-9 m below ridgetops generally exceeds the Interface 2 depth (6 m) but not the Interface 3 depth (11-17 m). While we interpret a “layered” critical zone structure, our observations suggest a broad, gradual zone of physical and chemical weathering, starting a few meters below the surface, and extending to ~20 m below the ridgetops (**Figure 11**). This gradual zone of increasing material strength is similar to critical zone models presented at Shale Hills (West et al., 2019) and Calhoun Observatory (Holbrook et al., 2019).

From analysis of borehole data, seismic velocity, and vertical velocity gradient, we can characterize critical zone structure at Rancho Venada as including: (1) a thin (< 1 m) soil layer (Pedrazas et al., 2021), (2) a ~ 5m thick saprolite layer that thins abruptly at the channels, across which most chemical reactions occur and mechanical strength dramatically changes, (3) a weathered bedrock layer of high velocity gradient in which the presence of open, oxidized fractures gradually decrease, and (4) a variably thick fractured bedrock layer with closed, unoxidized fractures.

5.2 Characterizing weathering across hillslopes

Our seismic refraction surveys capture changes in the material properties of the subsurface that align with borehole observations, allowing us to project Interfaces 2 and 3 across the landscape. With these interfaces estimated at the landscape scale, we can explore how the weathering structure varies with respect to slope aspect and bedding orientation, and exploit relationships between P-wave velocity (Vp) and rock properties to model subsurface bulk porosity.

5.2.1 North vs. south facing hillslopes

Several seismic refraction studies have observed thicker saprolite and weathered rock on north-facing slopes and a thinner weathered layer on south-facing slopes (Befus et al., 2011; McGuire et al., 2014; Nielsen et al., 2021; Wang et al., 2021). However, most of these sites have a different lithology and climate regime than Rancho Venada, both of which are shown to affect the magnitude of weathering asymmetry with aspect (Inbar et al., 2018; Pelletier et al., 2018) and the thickness of weathered material (Hahm et al., 2019b).

The stark difference in vegetation (**Figure 1**) and the thicker soil profiles on north- versus south-facing hillslopes indicate that aspect-dependent solar radiation does play a role in surface landscape processes at Rancho Venada (Pedrazas et al., 2021). Tree roots here can extend 14 m laterally and 6-8 m down into the weathered bedrock (Hahm et al., 2022), and therefore we may reasonably expect roots to contribute to bedrock weathering through biochemical or biomechanical processes (i.e. Pawlik et al., 2016). However, seismic refraction does not show a clearly thicker saprolite layer on north-facing slopes (**Figure 10**), consistent with borehole observations from Pedrazas et al. (2021). This result is contrary to what we might expect in a precipitation-limited environment (as in Pelletier et al., 2018), where increased soil moisture and root-rock interactions on north-facing slopes can exert a top-down influence on critical zone structure.

Other studies have also observed a lack of clear aspect-dependent saprolite thickness at sites with clear aspect-dependent vegetation density. For example, south-facing slopes of the Santa Catalina Mountains in Arizona have thicker saprolite, despite a lower tree density (Leone et al., 2020). This is attributed to the orientation of bedrock foliation planes, which dip into the surface topography at a high angle on the south-facing slope and are oriented parallel to the north-facing slope. The high angle intersection on the south-facing slope facilitates enhanced weathering along the weak foliation planes, creating thicker saprolite. At Rancho Venada, bedding and dominant fracture planes are oriented N10°W, therefore the apparent dip of the lithology and of the most abundant fracture set is nearly horizontal for the bedding-parallel seismic survey lines. There is no significant difference in the angle between bedding or fracture planes and the surface topography for north versus south-facing slopes. Therefore, increased hydraulic conductivity along planes of weakness (e.g. bedding planes) cannot explain the lack of north/south aspect-dependency below the soil layer at Rancho Venada.

It is possible that the top-down influence of tree roots on the critical zone does not extend deep enough or is masked out by more dominant landscape processes that create symmetrical hillslopes. Regional tectonic stress, hydrologic properties of the bedrock, or the influence of bedding orientation on the landscape could contribute to saprolite thickness at Rancho Venada. In this case, top-down climate processes may be negligible below the soil

layer. Still, given the stark contrast in vegetation density with aspect, the documented seasonal use of bedrock moisture by tree roots at depths > 5 m at this site (Hahm et al., 2022), and the potential for tree roots to expand fractures and promote chemical weathering within fractured rock (Hasenmueller et al., 2017), it is worth considering the role of climate and root distribution in influencing weathering depth.

A plausible explanation for the similar weathering thickness on north and south-facing slopes is that weathering processes at RV have not always been precipitation-limited. Oxygen isotope analysis of sediment cores from Clear Lake (~20 km from Rancho Venada) reveal that from 13ka – 80ka the climate of the region was 8°C colder with ~1000 mm/yr more precipitation than its present condition (Adams and West, 1983). This cooler, wetter climate regime may have resulted in minimal differences in tree density with aspect, or a different tree species composition altogether (Cole, 1983; Adams and West, 1983). Assuming a steady-state landscape with a 0.1 mm/yr erosion rate (Pedrazas et al., 2021), a 6 m thick saprolite would have a residence time of 60 ky, and therefore most of the saprolite at Rancho Venada would have been influenced by a cooler climate regime in the past. A shift from cold-wet to warm-dry climate conditions in the last 13ka may therefore only impact the soil layer and the shallowest part of the saprolite. This may explain why the vegetation density and soil thickness are different between north- and south-facing slopes, while the saprolite thickness is roughly the same.

The influence of past climate on slope aspect asymmetry has been documented across many regions. At Shale Hills in Pennsylvania, frost-cracking during the last glacial maximum interacted with microtopography to drive the hillslope asymmetry observed today, despite a lack of frost-cracking conditions in the present climate (West et al., 2019; Wang et al., 2021). Likewise, the strong slope asymmetry currently observed in the Redondo Mountains in New Mexico can be explained by vegetation regimes present in the cooler Pleistocene (Istanbulluoglu, 2008). Past climate can also play a significant role in aspect-dependent surface topographic gradients and drainage densities (McGuire et al., 2014).

5.2.2 Porosity

Characterizing water storage at the landscape scale is crucial in Mediterranean climate environments. Water stored below the soil during wet seasons can be accessed by vegetation during the growing season in dry summers, and help sustain them through drought (Hahm et al., 2022). Several recent studies have applied rock physics models to estimate total porosity from seismic refraction data (e.g. Holbrook et al., 2014; Pasquet et al., 2016; Flinchum et al., 2018a,b; Hayes et al., 2019; Gu et al., 2020; Callahan et al., 2020). The parameters known to influence Vp include elastic moduli of the mineral composition, porosity, and saturation level. Saturation with depth can be measured from drying and weighing material (Holbrook et al., 2014), Vp/Vs ratio from downhole geophysics such as from sonic velocity logs (Gu et al., 2020), or nuclear magnetic resonance surveys (Flinchum et al., 2018b; Holbrook et al., 2019). Without direct measurements of saturation, the rock physics model explores a nonlinear relationship between porosity and saturation (**Figure 11a**).

Despite not having direct measurements of absolute saturation with depth, we are able to take advantage of multiple datasets to explore porosity at the landscape scale. The matrix porosity (Φ_{matrix}), measured from chips of the core, is assumed to be perennially saturated porosity that changes little with depth at our study hills. Incorporating $\Delta\theta$ from neutron probe

surveys suggests additional storage must be available to accommodate the observed seasonally dynamic water content. The dynamic porosity ($\Phi_{dynamic}$) therefore represents a lower bound estimate of the total porosity. Modeling bulk porosity from seismic refraction allows us to estimate a total porosity that reflects the unsaturated, pervasively fractured nature of the core. Our total porosity distribution ranges from 35% at the surface to ~9% at a 8 m depth (**Figure 11b**), implying a significant volume of fracture porosity.

While there are significant sources of uncertainty (e.g. mineral composition, empirical parameters, saturation) in the rock physics model such that our estimates of bulk porosity are not exact, the relative decrease in bulk porosity across the saprolite-weathered bedrock boundary matches high fracture density in core photos (**Figure 11c**) and material strength from the core that is not represented by matrix porosity alone. Additionally, the extensive hydrologic datasets at this site provide a check on our rock physics model, as total porosity must be higher than the observed water storage (Hahm et a., 2022). The agreement between seismically-determined porosity gradients and transitions in fracture density and moisture content from boreholes implies that our seismic surveys can be deployed at a larger scale to capture porosity transitions where boreholes are absent. A combination of other geophysical datasets such as incorporating electrical resistivity measurements could provide a better constraint on lateral distribution of saturation (e.g. Blazevic et al., 2020; Chen and Niu, 2022).

5.3 Broader implications to Critical Zone models

Weathering structure at Rancho Venada can inform mechanistic features of critical zone development in semi-arid landscapes. Upslope thickening topography of the weathered layers suggests that the hydraulic conductivity model proposed by Rempe and Dietrich (2014), in which drainage of chemically equilibrated groundwater controls the fresh bedrock boundary, could apply to this landscape. This model predicts a permanent water table limiting the extent of chemical weathering reactions, but we find no evidence of a permanent water table here within the depth range of the weathered zone (Hahm et al., 2022; Pedrazas et al., 2021). Water was observed in the boreholes 30 - 35 m below the surface for MH7R, and 15 - 21m below the surface for MH3R and MH2R (Hahm et al., 2022; Pedrazas et al., 2021). However, the present-day water table may not align with the interface depths if the water table has dropped since the cooler and wetter climate of the Pleistocene. Alternatively, the nested reaction fronts proposed by Lebedeva and Brantley (2013) and Brantley et al. (2017) could describe Rancho Venada's weathering structure. Lebedeva and Brantley (2020) show that in settings with low infiltration rate, reaction fronts can be located above the water table.

Pedrazas et al. (2021) found a roughly linear scaling relationship between hillslope length and relief of interfaces 2 and 3. Both interfaces agree with the predicted elevation of fresh unweathered bedrock (Zb) defined by Rempe and Dietrich (2014). The elevation of the transition to unweathered bedrock (Interface 3) appears roughly linear from channel to ridge (**Figure 13a**). When normalized by the channel-ridgetop distance, the hillslope profiles sharing the larger ridgetop (MH8N and MH7S) have a steeper slope of interface 3 than profiles for the smaller ridges (MH6R, MH3R, MH2R), possibly indicating some variability in weathering processes between the lower vs. higher relief ridges (**Figure 13b**). Our seismic profiles do not allow us to draw a strong conclusion on the scaling relationship between hillslope length and relief, as proposed in Pedrazas et al. (2021). However, the agreement between seismic

refraction and borehole data at this site means that additional seismic surveys spanning new ridges can be used to determine Zb depth even without boreholes present.

The ratio of gravitational and horizontal tectonic stresses can also determine the potential of subsurface fracturing and create deep weathering extending below the elevation of the channel in high-compressional regimes (St. Clair et al., 2015; Moon et al., 2017). Pelletier (2017) further suggests that soil production is highly influenced by topographic steepness that can open preexisting bedrock fractures. We performed seismic surveys both parallel and perpendicular to the least compressive stress orientation and did not observe low velocities below the channel elevation in either case. The lack of surface-mirroring weathering could be qualitatively used to assume low compressive stress parallel to the bedding strike at Rancho Venada. However, this site is less than 30 km away from the Bartlett Springs Fault system, and the principal compressive stress has been oriented roughly N-S (roughly parallel to the bedding strike) for at least the past 5 Myr (Atwater and Stock, 1998). With a contemporary maximum shear strain rate of ~50 - 100 nano-strain/yr (Zeng et al., 2018; Xu et al., 2020), we consider Rancho Venada subject to a high contemporary tectonic stressing rate relative to most regions of the U.S. Even though the current tectonic stressing rate is high, high internal strain rate and regional earthquake cycles may decrease material strength at Rancho Venada. This adds additional complexity to estimating fracture distribution from a simple stress model.

The sedimentary bedrock lithology has a distinct influence on the landscape at Rancho Venada, shaping the orientation and surface slope of the ridges and valleys (Rich et al., 1971; Pedrazas et al., 2021). The main study ridges are located within a turbidite sequence of interbedded mudstone and siltstone, with occasional meter-scale sandstone beds. The thicker weathered zone below MH2R is likely because MH2R intersects a larger proportion of fine-grained material (Pedrazas et al., 2021; **Figure 6**). East of our boreholes, the main north-striking ridge is capped by a thick (> 5 m) sandstone bed. Line 8 features a high-velocity zone at shallow depth east of the ridgetop that matches the location of the MH3R sandstone cap (**Figure 7**), highlighting the role of sedimentary bedding in controlling weathering depth. The anti-dip hillslope just east of the ridge is dominated by mudstone (though the overall unit east of the main ridge has a higher sandstone component, as in **Figure 1**), and has much thicker low-velocity material (**Figure 7**). The difference in fracture or joint density between different major rock types (sandstone vs mudstone) may influence the thickness of the critical zone here. Bedding orientation and changes in lithology may also help to explain why different orientations of seismic refraction survey lines result in different Vp values for the same location (**Figure S3**).

However, we do not find lithology or bedding structure to be as strong a control on critical zone structure at Rancho Venada as at some metamorphic sites (i.e. Leone et al., 2020). While there is thicker weathered material on the east-facing slope of Line 8, we do not observe a similar pattern for Line 9, which also runs perpendicular to bedding across an east and west-facing slope (**Figure S5**). We therefore do not see a consistent contrast between east and west-facing slopes despite the vastly different intersection of bedding planes with surface topography (**Figure 7**). Future work to compare fracture orientation and surface slope with weathering depth, along with more detailed geologic mapping, may further flesh out the influence of the regional geology on the critical zone structure at this site.

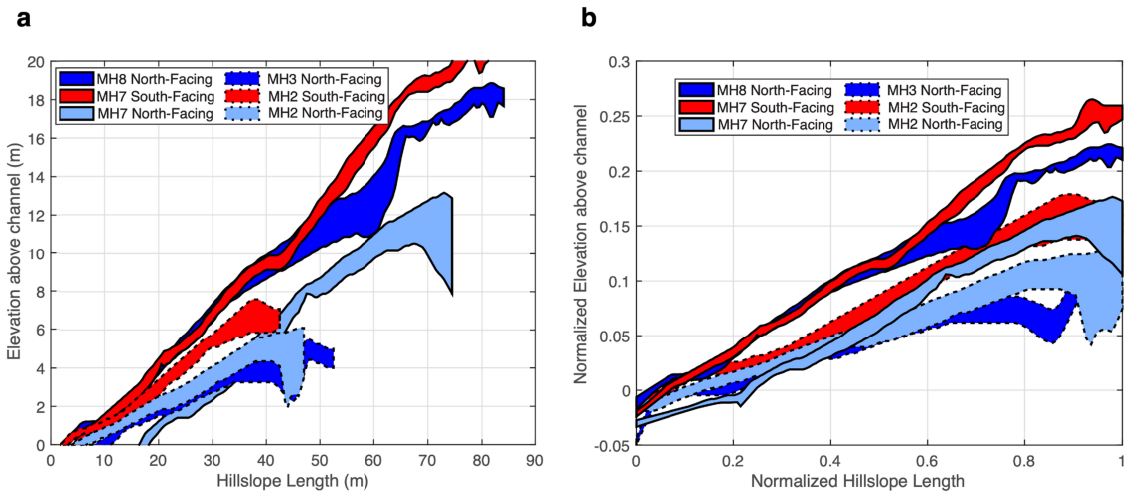

Figure 13. (a) Topography of interface 3 with hillslope length. The 6 different profiles are north (blue) and south (red) facing hills from seismic lines 1 and 7. Note 0 m in the y-axis represents the ground surface. **(b)** Same as **a** but the hillslope length of each profile is normalized. Note there is no consistent pattern between different profiles.

6. CONCLUSIONS

Through a combination of near-surface geophysics and direct observations from boreholes, we are able to characterize critical zone structure at Rancho Venada, a semi-arid, sedimentary ridge-valley landscape in northern California. Seismic data alone reveals a weathered zone from 4-13 m below ridgetops, over which velocity increases from ~1000 – 2500 m/s. In combination with borehole data, we can detect a transition from pervasively fractured and chemically weathered material, to more competent material at a 5-6 m depth, corresponding to a velocity range of 1284 ± 203 m/s. This transition is interpreted as the saprolite-weathered bedrock transition, and is largely surface-parallel, with a slight thickening towards the ridges and sharp thinning at the channels. A second, deeper transition zone is observed in the borehole logs, as yellowness hue further decreases, corresponding to a velocity range of 1973 ± 435 m/s. We interpret the deeper transition as the weathered - fractured bedrock boundary. Bedding-parallel and bedding-perpendicular lines indicate the weathered zone thins towards the main channel in the west, and towards the subchannels to the north and south.

Despite higher tree density and thicker soils on north-facing slopes, we observe an overall similar saprolite and weathered bedrock layer on both north- and south-facing slopes, contrary to what we might expect in a precipitation-limited environment. The cooler, wetter climate experienced during the Pleistocene may have allowed for the presence of trees on both hillslopes, creating equally thick saprolite layers that have not yet adjusted to the current climate condition.

7. ACKNOWLEDGEMENTS

We thank the Brown and the Hemmi families for providing site access. Bill Dietrich, Associated Editor Jon Pelletier, and 3 anonymous reviewers provided insightful feedback that significantly improved the quality of this work. We are grateful for field assistance from Anna

Weniger, Colleen Murphy, Jeng-Hann Chong, Kristen Fauria, and Maryn Sanders to carry out the seismic refraction surveys. We also thank Bill Dietrich, Kristen Fauria, and Alex Bryk for their insights and significant contributions in the earlier phase of the research. BHR is supported by the Carleton College Paglia post-baccalaureate fellowship. Part of this research is contributed by NSF-EAR-2012616.

8. DATA AVAILABILITY STATEMENT

Borehole data sets are published in Pedrazas et al. (2021). Volumetric water content and water table depths are published in Hahm et al. (2022). The THB rj-MCMC inversion is available on Zenodo (http://doi.org/10.5281/zenodo.4590999) and actively maintained in Github (https://github.com/MongHanHuang/THB_rjMCMC).

9. REFERENCES

Adam, D. P., & West, G. J. (1983). Temperature and Precipitation Estimates Through the Last Glacial Cycle from Clear Lake, California, Pollen Data. *Science*, 219, 168-170.

Anderson, R. S., Anderson, S. P., & Tucker, G. E. (2013). Rock damage and regolith transport by frost: An example of climate modulation of the geomorphology of the critical zone. *Earth Surface Processes and Landforms*, 38(3), 299–316. https://doi.org/10.1002/esp.3330

Anderson, S. P., Hinckley, E-L., Kelly, P., & Langston, A. (2014). Variation in critical zone processes and architecture across slope aspects. *Procedia Earth and Planetary Science*, 10, 28-33.

Anderson, R. S., Rajaram, H., & Anderson, S. P. (2019). Climate driven coevolution of weathering profiles and hillslope topography generates dramatic differences in critical zone architecture. *Hydrological Processes*, 33(1), 4–19.

American Society for Testing and Materials (ASTM), 2022, Standard Test Method for Standard Penetration Test (SPT) and Split-Barrel Sampling of Soils. URL: https://www.astm.org/d1586_d1586m-18e01.html

Atwater, T., & Stock, J. (1998). Pacific-north america plate tectonics of the neogene southwestern united states: an update. *International Geology Review*, 40(5), 375–402.

Bale, C. L., Williams, J. B., & Charley, J. L. (1998). The impact of aspect on forest structure and floristics in some Eastern Australian sites. *Forest and Ecology Management*, 110, 363-377.

Befus, K. M., Sheehan, A. F., Leopold, M., Anderson, S. P., & Anderson, R. S. (2011). Seismic constraints on critical zone architecture, Boulder Creek Watershed, Front Range, Colorado. *Vadose Zone*, 10, 915-927.

Blazevic, L. A., Bodet, L., Pasquet, S., Linde, N., Jougnot, D., & Longuevergne, L. (2020). Time-lapse seismic and electrical monitoring of the vadose zone during a controlled infiltration experiment at the Ploemeur hydrological observatory, France. *Water*, 12(5), 1230.

Brantley, S. L., Lebedeva, M. I., Balashov, V. N., Singha, K., Sullivan, P. L., & Stinchcomb, G. (2017). Toward a conceptual model relating chemical reaction fronts to water flow paths in hills. *Geomorphology*, 277, 100-117.

Brooks, P. D., Chorover, J., Fan, Y., Godsey, S. E., Maxwell, R. M., McNamara, J. P., & Tague, C. (2015). Hydrological partitioning in the critical zone: Recent advances and

opportunities for developing transferable understanding of water cycle dynamics. *Water Resources Research,* 51, 6973–6987. doi:10.1002/2015WR017039.

Burdick, S., & Lekic, V. (2017). Velocity variations and uncertainty from transdimensional P-wave tomography of North America. *Geophys. J. Int.*, 209, 1337-1351.

Callahan, R. P., Riebe, C. S., Pasquet, S., Ferrier, K. L., Grana, D., Sklar, L. S., Taylor, N. J., et al. (2020). Subsurface weathering revealed in hillslope-integrated porosity distributions. *Geophysical Research Letters*, 47.

Callahan, R. P., Riebe, C. S., Sklar, L. S., Pasquet, S., Ferrier, K. L., Hahm, W. J., ... & Holbrook, W. S. (2022). Forest vulnerability to drought controlled by bedrock composition. Nature Geoscience, 1-6.

Chen, H., & Niu, Q. (2022). Improving moisture content estimation from field resistivity measurements with subsurface structure information. Journal of Hydrology, 613, 128343.

Clarke, B. A., & Burbank, D. W. (2011). Quantifying bedrock-fracture patterns within the shallow subsurface: Implications for rock mass strength, bedrock landslides, and erodibility. *Journal of Geophysical Research*, 116. doi:10.1029/2011JF001987

Cole, K. (1983). Late Pleistocene Vegetation of Kings Canyon, Sierra Nevada, California. *Quaternary Research*, 19, 117-129.

Dietrich, W. (2019). High resolution mapping of antelope valley ranch, ca. National Center for Airborne Laser Mapping (NCALM). https://doi.org/10.5069/G9QC01MQ

Dvorkin J, Walls, J., & Davalos, G. (2021). Velocity-Porosity-Mineralogy Model for Unconventional Shale and Its Applications to Digital Rock Physics. *Front. Earth Sci.*, 8. doi:10.3389/feart.2020.613716

East, A. E., & Sankey, J. B. (2020). Geomorphic and sedimentary effects of modern climate change: Current and anticipated future conditions in the western United States. Reviews of Geophysics, 58. https://doi.org/10.1029/2019RG000692

Eberhart-Phillips, D., Han, D.-H., & Zoback, M. D. (1989). Empirical relationships among seismic velocity, effective pressure, porosity, and clay content in sandstone. *Geophysics*, 54(1), 82-89.

Flinchum, B. A., Holbrook, W. S., Rempe, D., Moon, S., Riebe, C. S., Carr, B. J., Hayes, J. L., St Clair, J., and Peters, M. P. (2018a). Critical zone structure under a granite ridge inferred from drilling and three-dimensional seismic refraction data. *Journal of Geophysical Research*, 123: 1317–1343.

911 Flinchum, B. A., Holbrook, W. S., Grana, D., Parsekian, A. D., Carr, B. J., Hayes, J. L., & Jiao,
912 J. (2018b). Estimating the water holding capacity of the critical zone using near-surface
913 geophysics. *Hydrological Processes*, 32, 3308-3326.

914 Flinchum, B. A., Holbrook, W. S., & Carr, B. J. (2022). What Do P-Wave Velocities Tell Us
915 About the Critical Zone? *Front. Water*, 3. https://doi.org/10.3389/frwa.2021.772185

916 Godderis, Y., & Brantley, S. L. (2013). Earthcasting the future critical zone. *Elementa*, 1. doi:
917 10.12952/journal.elementa.000019

918 Grana, D., Parsekian, A. D., Flinchum, B. A., Callahan, R. P., Smeltz, N. Y., Li, A., Hayes, J. L.,
919 et al. (2022). Geostatistical Rock Physics Inversion for Predicting the Spatial Distribution
920 of Porosity and Saturation in the Critical Zone. *Math Geosci*.
921 https://doi.org/10.1007/s11004-022-10006-0

922 Gu, X., Mavko, G., Ma, L., Oakley, D., Accardo, N., Carr, B. J., Nyblade, A. A., et al. (2020).
923 Seismic refraction tracks porosity generation and possible CO2 production at depth
924 under a headwater catchment. *PNAS*.

925 Hahm, W. J., Riebe, C. S., Lukens, C. E., & Araki, S. (2014). Bedrock composition regulates
926 mountain ecosystems and landscape evolution. *PNAS*, 111, 3338-3343.

927 Hahm, W. J., Dralle, D. N., Rempe, D. M., Bryk, A. B., Thompson, S. E., Dawson, T. E., &
928 Dietrich, W. E. (2019a). Low subsurface water storage capacity relative to annual rainfall
929 decouples mediterranean plant productivity and water use from rainfall variability.
930 *Geophysical Research Letters*, 46, 6544–6553. https://doi.org/10.1029/2019gl083294

931 Hahm, W. J., Rempe, D. M., Dralle, D. N., Dawson, T. E., Lovill, S. M., Bryk, A. B., & Dietrich,
932 W. E. (2019b). Lithologically controlled subsurface critical zone thickness and water
933 storage capacity determine regional plant community composition. *Water Resources*
934 *Research*, 55(4), 3028–3055. https://doi.org/10.1029/2018WR023760

935 Hahm, W. J., Dralle, D. N., Sanders, M., Bryk, A. B., Fauria, K. E., Huang, M. H., Hudson-
936 Rasmussen, B., et al. (2022). Bedrock vadose zone storage dynamics under extreme
937 drought: Consequences for plant water availability, recharge, and runoff. *Water*
938 *Resources Research*, 58. https://doi.org/10.1029/2021WR031781

939 Handwerger, A. L., Huang, M-H., Fielding, E. J., Booth, A. M., & Burgmann, R. (2019). A shift
940 from drought to extreme rainfall drives a stable landslide to catastrophic failure. *Scientific*
941 *Reports*, 9. https://doi.org/10.1038/s41598-018-38300-0

942 Harwood, D.S. and Helley, E.J., 1987, Late Cenozoic tectonism of thhe Sacramento Valley,
943 California, Profesisonal Paper 1359, https://doi.org/10.3133/pp1359

Hasenmueller, E. A., Gu, X., Weitzman, J. N., Adams, T. S., Stinchcomb, G. E., Eissenstat, D. M., et al., and Kaye, J. P. (2017). Weathering of rock to regolith: The activity of deep roots in bedrock fractures. Geoderma, 300, 11–31. https://doi.org/10.1016/j.geoderma.2017.03.020

Hayes, J. L., Riebe, C. S., Holbrook, W. S., Flinchum, B. A., & Hartsough, P. C. (2019). Porosity production in weathered rock: Where volumetric strain dominates over chemical mass loss. *Science Advances*, 5. https://doi.org/10.1126/sciadv.aao0834.

Helgerud, M. B., Dvorkin, J., Nur, A., Sakai, A., & Collett, T. (1999). Elastic-wave velocity in marine sediments with gas hydrates: Effective medium modeling. *Geophysical Research Letters*, 26, 2021-2024.

Holbrook, W. S., Riebe, C. S., Elwaseif, M., Hayes, J. L., Harry, D. L., Basler-Reeder, K., Malazian, A. (2014). Geophysical constraints on deep weathering and water storage potential in the Southern Sierra Critical Zone Observatory. *Earth Surface Processes Landforms*, 39, 366–380.

Holbrook, W. S., Marcon, V., Bacon, A. R., Brantley, S. L., Carr, B. J., Flinchum, B. A., & Riebe, C. S. (2019). Links between physical and chemical weathering inferred from a 65-m-deep borehole through Earth's critical zone. *Scientific Reports*, 9(1), 4495. https://doi.org/10.1038/s41598-019-40819-9

Huang, M.-H., Hudson-Rasmussen, B., Burdick, S., Lekic, V., Nelson, M. D., Fauria, K. E., & Schmerr, N. (2021). Bayesian seismic refraction inversion for critical zone science and near-surface applications. *Geochemistry, Geophysics, Geosystems*, 22(5). https://doi.org/10.1029/2020GC009172

Inbar, A., Nyman, P., Rengers, F. K., Lane, P. N. J., & Sheridan, G. J. (2018). Climate dictates magnitude of asymmetry in soil depth and hillslope gradient. *Geophysical Research Letters*, 45, 6514–6522.

Istanbulluoglu, E., Yetemen, O., Vivoni, E. R., Gutiérrez-Jurado, H. A., & Bras, R. L. (2008). Eco-geomorphic implications of hillslope aspect: Inferences from analysis of landscape morphology in central New Mexico. *Geophysical Research Letters*, 35.

Klos, P. Z., Goulden, M. L., Riebe, C. S., Tague, C. L., O'Geen, A. T., Flinchum, B. A., Safeeq, M., et al. (2018). Subsurface plant-accessible water in mountain ecosystems with a Mediterranean climate. *WIREs Water*, 5. https://doi.org/10.1002/wat2.1277

Lebedeva, M. I., & Brantley, S. L. (2013). Exploring geochemical controls on weathering and erosion of convex hillslopes: beyond the empirical regolith production function. *ESPL*, 38, 1793-1807.

977 Lebedeva, M. I., and Brantley, S. L. (2020). Relating the depth of the water table to the depth of
978 weathering. *Earth Surf. Process. Landforms*, 45: 2167– 2178.
979 https://doi.org/10.1002/esp.4873

980 Lee, S. G., & de Freitas, M. H. (1990). Seismic refraction surveys for predicting the intensity and
981 depth of weathering and fracturing in granitic masses. *Field Testing in Engineering*, 6.

982 Lee, S. S. (2018). Spatial Patterns of Bedrock Weathering at the Hillslope Scale Inferred via
983 Drilling and Multi-Scale Geophysical Methods, (Master's Thesis). Austin, TX: University
984 of Texas.

985 Leone, J. D., Holbrook, W. S., Riebe, C. S., Chorover, J., Ferré, T. P. A., Carr, B. J., & Callahan,
986 R. P. (2020). Strong slope-aspect control of regolith thickness by bedrock foliation. *Earth*
987 *Surface Processes and Landforms*, 45, 2998–3010. https://doi.org/10.1002/esp.4947

988 Mavko, M., Mukerji, T., & Dvorkin, J. (2009). Appendices. *The rock physics handbook: Tools for*
989 *seismic analysis of porous media* (pp. 437–478). Cambridge: Cambridge University
990 Press.

991 McGuire, L. A., Pelletier, J. D., and Roering, J. J. (2014), Development of topographic
992 asymmetry: Insights from dated cinder cones in the western United States, *J. Geophys.*
993 *Res. Earth Surf.*, 119, 1725– 1750, doi:10.1002/2014JF003081.

994 Moon, S., Perron, J. T., Martel, S. J., Holbrook, W. S., & St Clair, J. (2017). A model of three-
995 dimensional topographic stresses with implications for bedrock fractures, surface
996 processes, and landscape evolution. *Journal of Geophysical Research: Earth Surface*,
997 122(4), 823–846. https://doi.org/10.1002/2016JF004155

998 Nelson, M. D., Bryk, A. B., Fauria, K., Huang, M. H., & Dietrich, W. E. (2017). Physical
999 properties of shallow landslides and their role in landscape evolution investigated with
1000 ultrahigh-resolution lidar data and aerial imagery. AGU fall meeting Abstracts.

1001 Nielsen, T., Bradford, J., Holbrook, W. S., & Seyfried, M. (2021). The effect of aspect and
1002 elevation on critical zone architecture in the Reynolds Creek Critical Zone Observatory:
1003 A seismic refraction study. *Frontiers in Water*, 3, 670524.

1004 Olona, J., Pulgar, J. A., Fernández-Viejo, G., López-Fernández, C., & González-Cortina, J. M.
1005 (2010). Weathering variations in a granitic massif and related geotechnical properties
1006 through seismic and electrical resistivity methods. *Near Surface Geophysics*, 8(6), 585-
1007 599.
1008
1009 Pasquet, S., Holbrook, W. S., Carr, B. J., & Sims, K. W. W. (2016). Geophysical imaging of
1010 shallow degassing in a Yellowstone hydrothermal system. *Geophysical Research*
1011 *Letters*, 43(23), 12-027.

Pasquet, S., Marçais, J., Hayes, J. L., Sak, P. B., Ma, L., & Gaillardet, J. (2022). Catchment-Scale Architecture of the Deep Critical Zone Revealed by Seismic Imaging. *Geophysical Research Letters*, 49(13).

Pawlik, L., Phillips, J. D., & Samonil, P. (2016). Roots, rock, and regolith: Biomechanical and biochemical weathering by trees and its impact on hillslopes—A critical literature review. *Earth-Science Reviews,* 159, 142–159. https://doi.org/10.1016/j.earscirev.2016.06.002

Pedrazas, M. A., Hahm, W. J., Huang, M.-H., Dralle, D., Nelson, M. D., Breunig, R. E., Fauria, K. E., et al. (2021). The relationship between topography, bedrock weathering, and water storage across a sequence of ridges and valleys. *Journal of Geophysical Research: Earth Surface*, 126(4). https://doi.org/10.1029/2020JF005848

Pelletier, J. D., Barron-Gafford, G. A., Gutiérrez-Jurado, H., Hinckley, E. S., Istanbulluoglu, E., McGuire, L. A., Niu., G.-Y., et al. (2018). Which way do you lean? Using slope aspect variations to understand critical zone processes and feedbacks. *Earth Surface Processes and Landforms* 43: 1133–1154.

Rempe, D. M., & Dietrich, W. E. (2014). A bottom-up control on fresh-bedrock topography under landscapes. *PNAS*, 111, 6576–6581.

Rich, E. I. (1971). Geologic map of the Wilbur Springs quadrangle, Colusa and Lake counties, California (Tech. Rep.).

Sanders, M., Nelson, M. D., Bryk, A. B., Huang, M.-H., Fauria, K., & Dietrich, W. E. (2019). The role of small shallow landslides in landscape evolution as revealed by high resolution differential lidar surveys and field mapping. In AGU fall meeting 2019. AGU.

Solazzi, S. G., Bodet, L., Holliger, K., & Jougnot, D. (2021). Surface-wave dispersion in partially saturated soils: the role of capillary forces. Journal of Geophysical Research: Solid Earth, 126(12), e2021JB022074.

St Clair, J., Moon, S., Holbrook, W. S., Perron, J. T., Riebe, C. S., Martel, S. J., & d. Richter, D. (2015). Geophysical imaging reveals topographic stress control of bedrock weathering. *Science*, 350(6260), 534–538. https://doi.org/10.1126/science.aab2210

Sullivan., P. L., Billings, S. A., Hirmas, D., Li, L., Zhang, X., Ziegler, S., Murenbeeld, K., et al. (2022). Embracing the dynamic nature of soil structure: A paradigm illuminating the role of life in critical zones of the Anthropocene. *Earth Science Reviews*, 225. https://doi.org/10.1016/j.earscirev.2021.103873

Wang, W., Nyblade, A. A., Mount, G., Moon, S., Chen, P., Accardo, N., Gu., X, et al. (2021). 3D seismic anatomy of a watershed reveals climate-topography coupling that drives water

flowpaths and bedrock weathering. *Journal of Geophysical Research: Earth Surface*, 126. https://doi.org/10.1029/2021JF006281

West, N., Kirby, E., Nyblade, A. A., & Brantley, S. L. (2019). Climate preconditions the critical zone: elucidating the role of subsurface fractures in the evolution of asymmetric topography. *ESPL*, 513, 197–205.

Xu, X., Sandwell, D. T., Klein, E., & Bock, Y. (2021). Integrated Sentinel-1 InSAR and GNSS time-series along the San Andreas fault system. *Journal of Geophysical Research: Solid Earth*, 126. https://doi.org/10.1029/2021JB022579

Zeng, Y., Petersen, M. D., & Shen, Z.-K. (2018). Earthquake potential in California-Nevada implied by correlation of strain rate and seismicity. *Geophysical Research Letters*, 45, 1778-1785. https://doi.org/10.1002/2017GL075967

Figure_01.

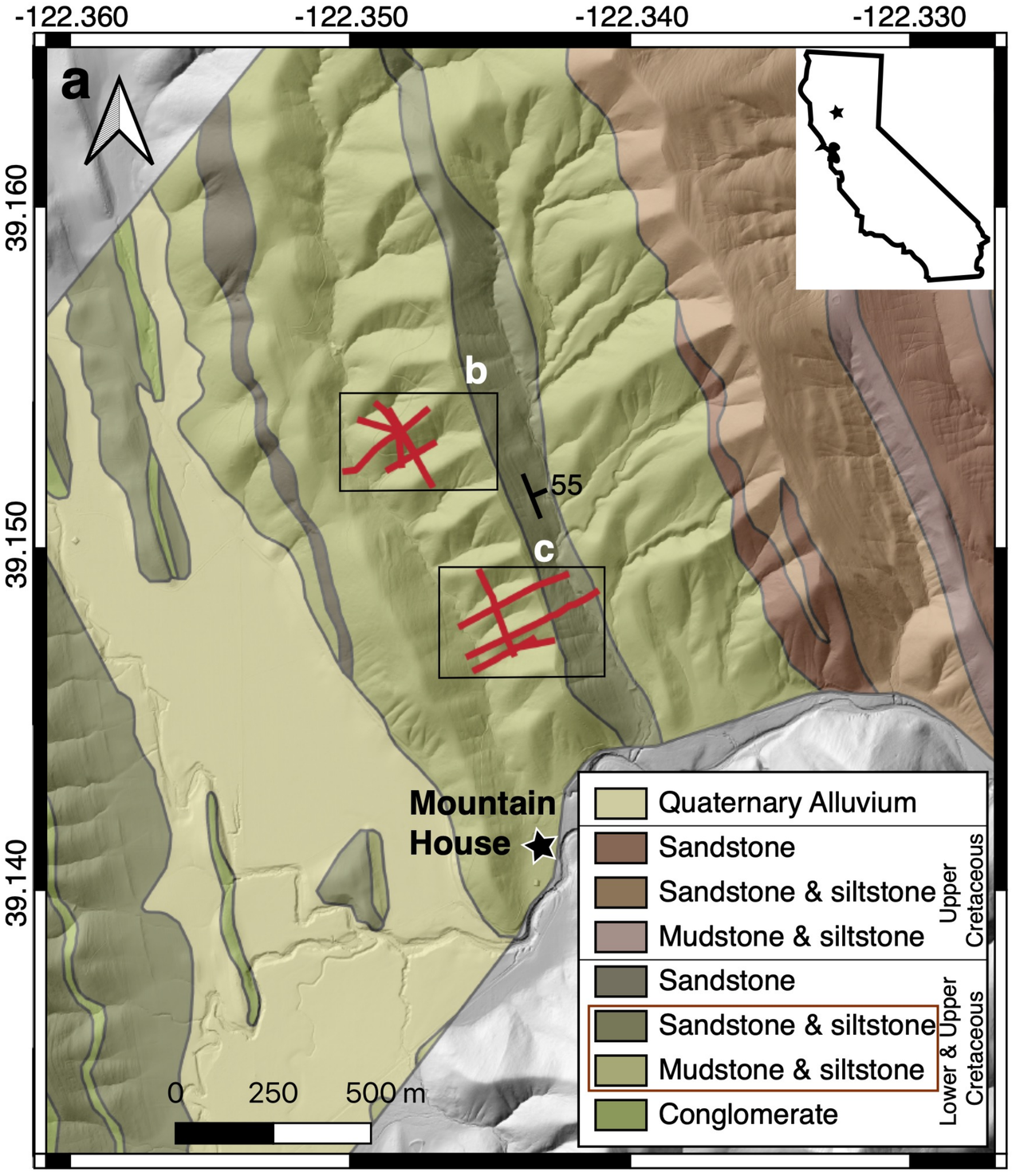

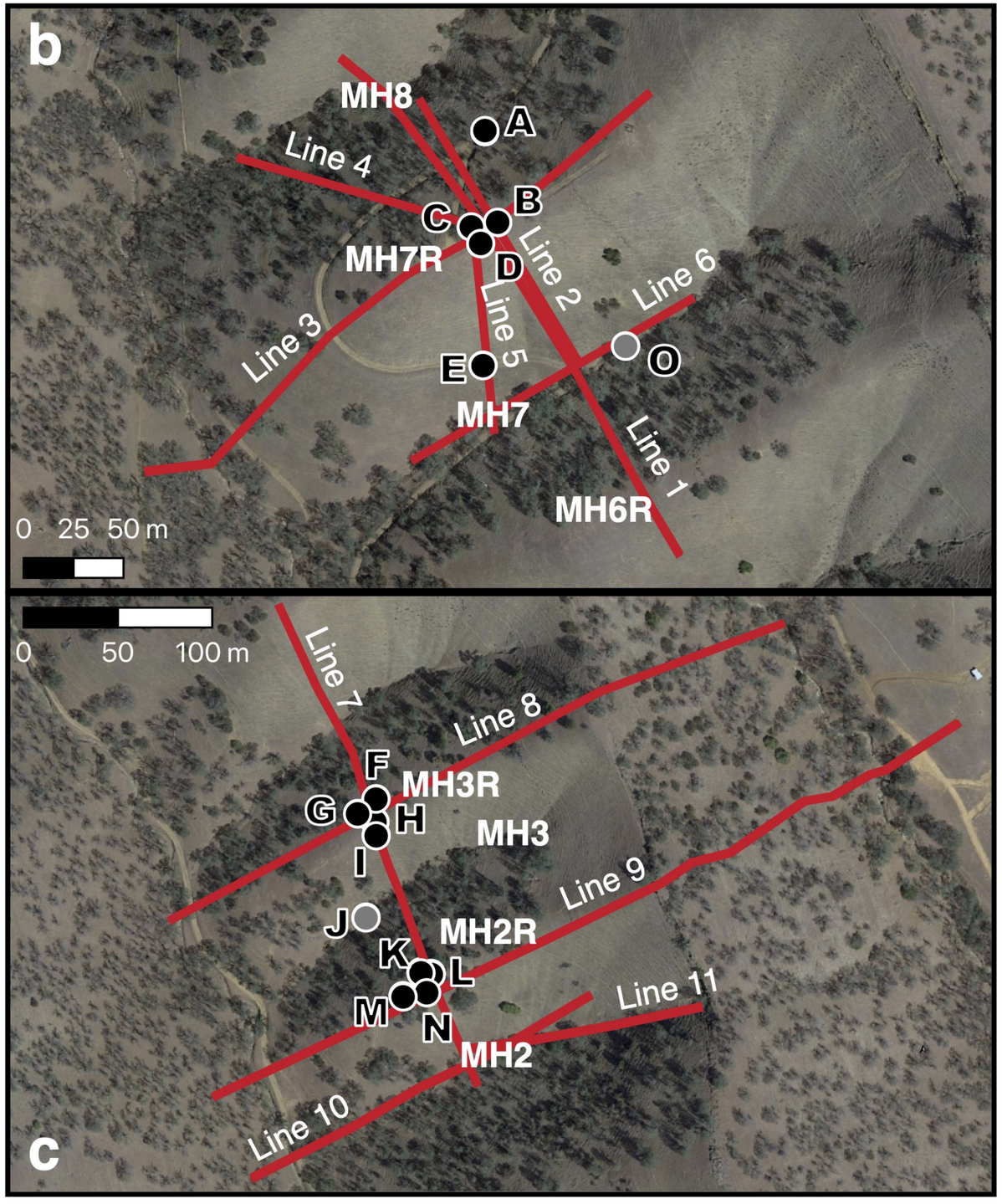

A: MH8-W1	D: MH7-W3	G: MH3-W3	J: MH3-P1	M: MH3-W5
B: MH7-W1	E: MH7-W4	H: MH3-W1	K: MH3-W6	N: MH3-W7
C: MH7-W2	F: MH3-W4	I: MH3-W2	L: MH3-W8	O: MH7-P1

Figure_02.

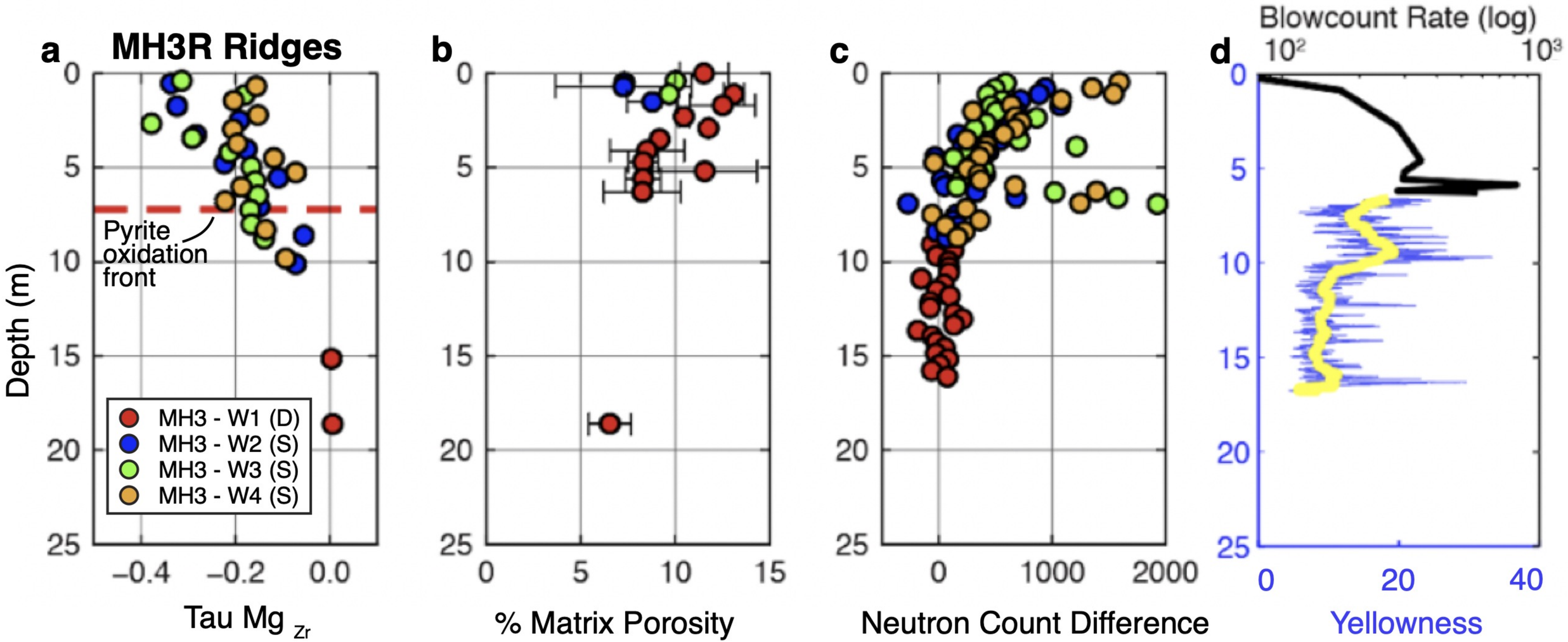
a
MH3R Ridges
Depth (m)
Pyrite oxidation front
MH3 - W1 (D)
MH3 - W2 (S)
MH3 - W3 (S)
MH3 - W4 (S)
Tau Mg Zr
b
% Matrix Porosity
c
Neutron Count Difference
d
Blowcount Rate (log)
Yellowness

Figure_03.

MH7 Ridge Inversion Products

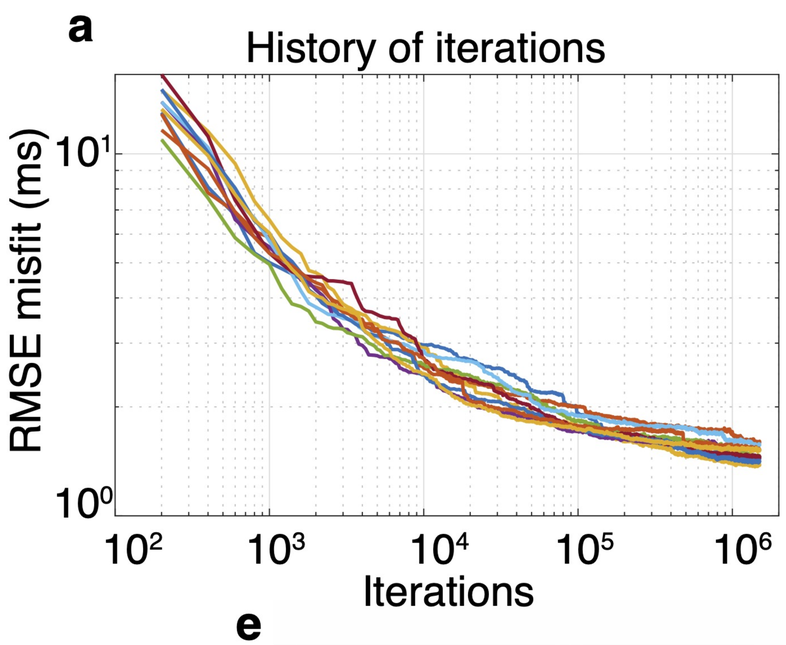

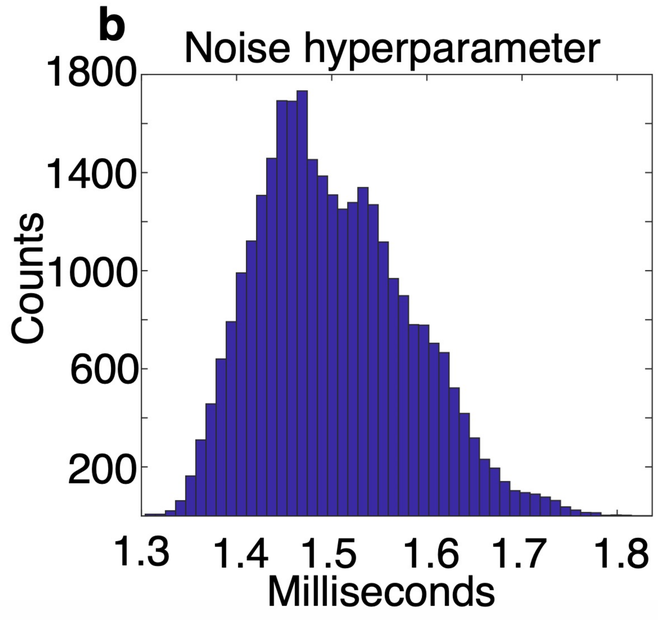

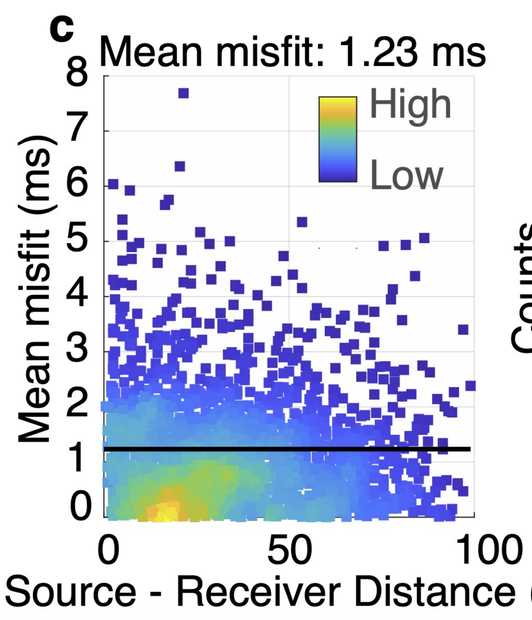

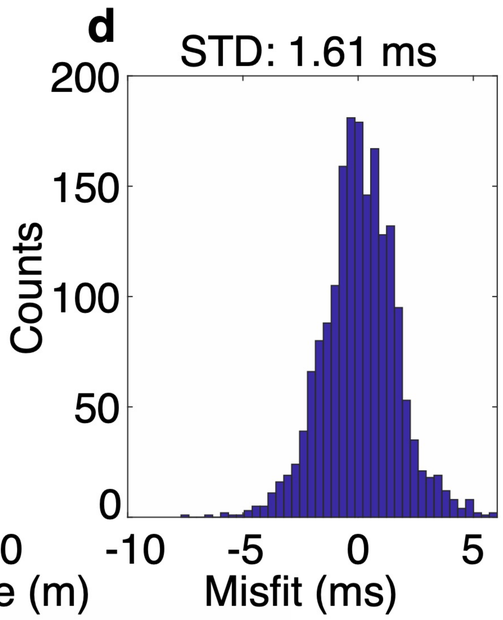

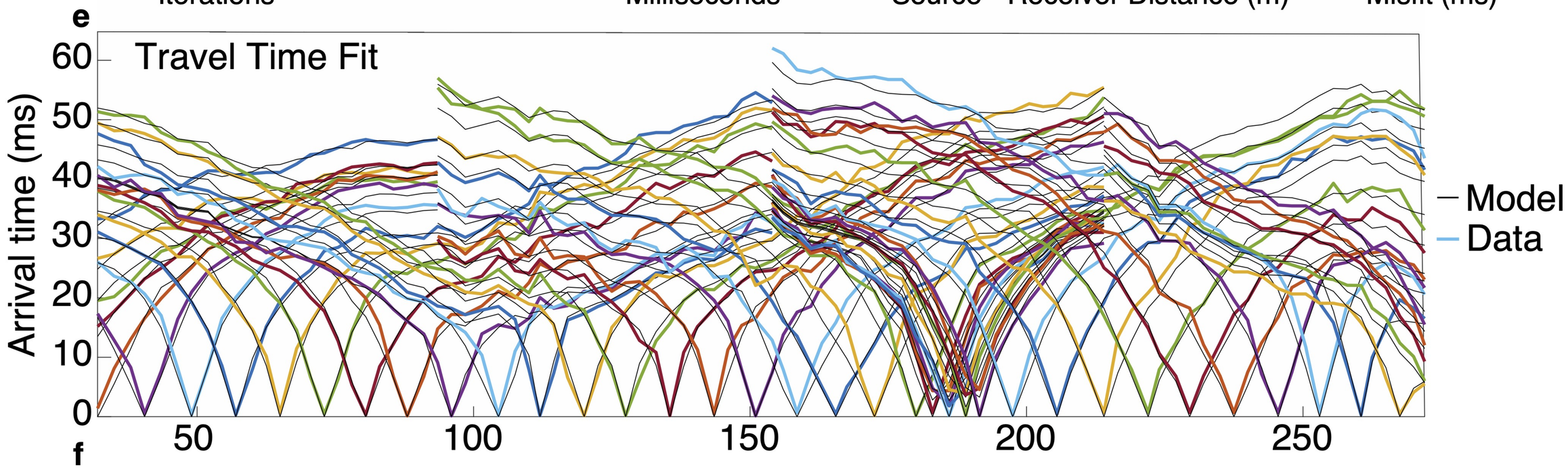

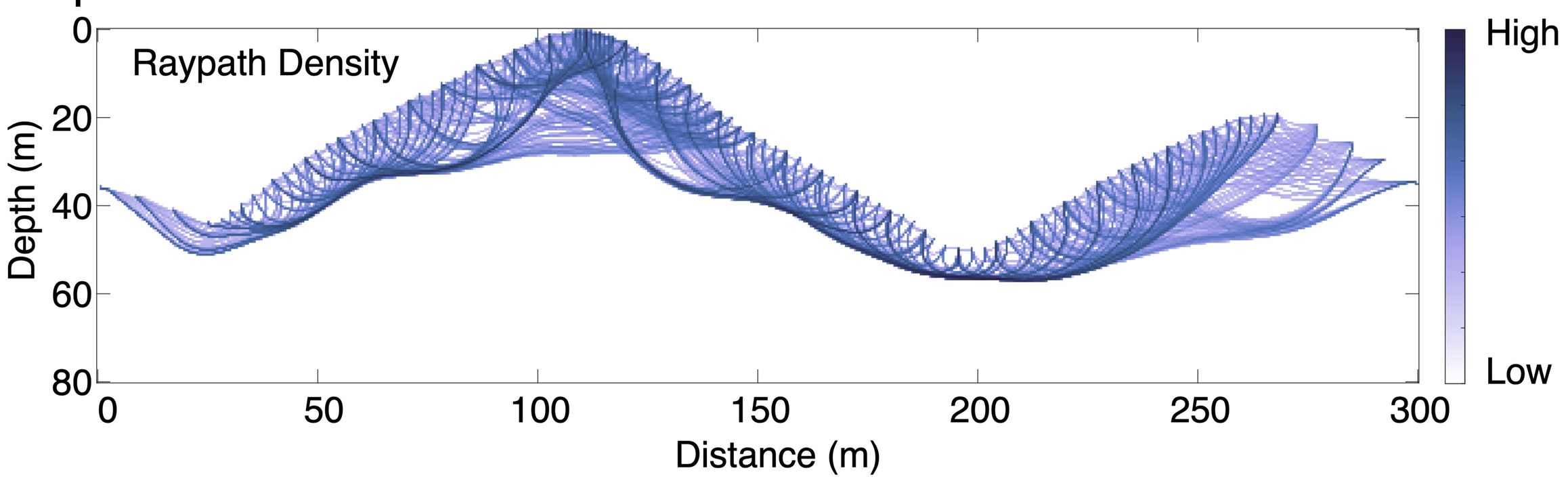

Figure_04.

a
Mean velocity (m/s)
MH7R
Line 1
B: MH7-W1
C: MH7-W2
D: MH7-W3
N
S
MH8
MH7
MH6R
Line 3
Line 6
Depth (m)
0
20
40
60
0
50
100
150
200
250
300
4000
3000
2000
1000
0
b
Coefficient of Variation (%)
50
25
0
c
Mean vertical gradient (m/s/m)
200
100
0
-100
Distance (m)

Figure_05.

a Line 6

Mean velocity (m/s)

O: MH7-P1

W

E

Line 5

Line 1

Depth (m)

0 10 20 30

0 20 40 60 80 100 120 140

4000 2000 0

b

Mean vertical gradient (m/s/m)

Depth (m)

0 10 20 30

0 20 40 60 80 100 120 140

Distance (m)

300 200 100 0 -100

Figure_06.

F: MH3-W4 H: MH3-W1 K: MH3-W8 N: MH3-W7
G: MH3-W3 I : MH3-W2 L: MH3-W5

a

Line 7

Mean velocity (m/s)

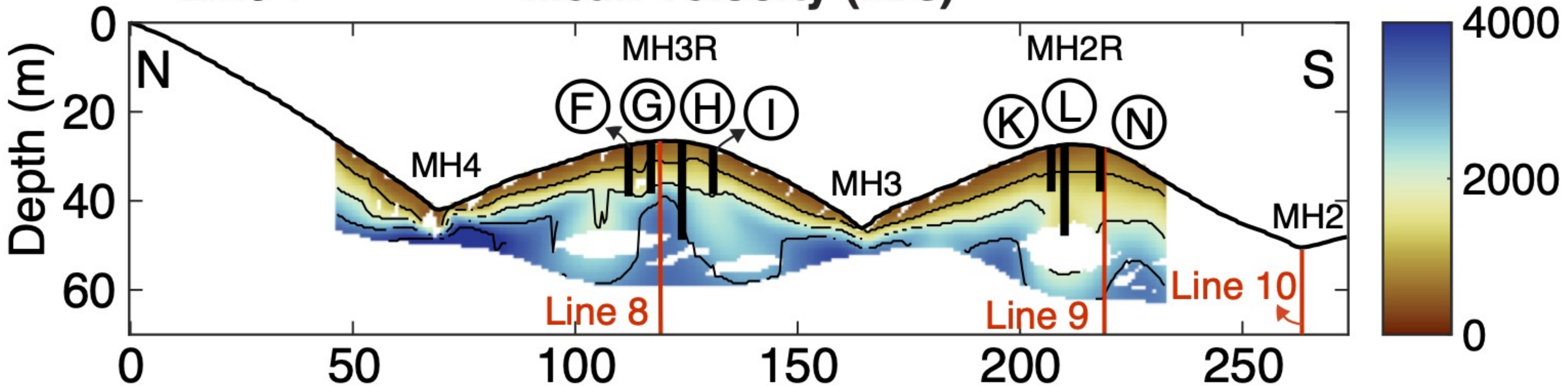

b

Mean vertical gradient (m/s/m)

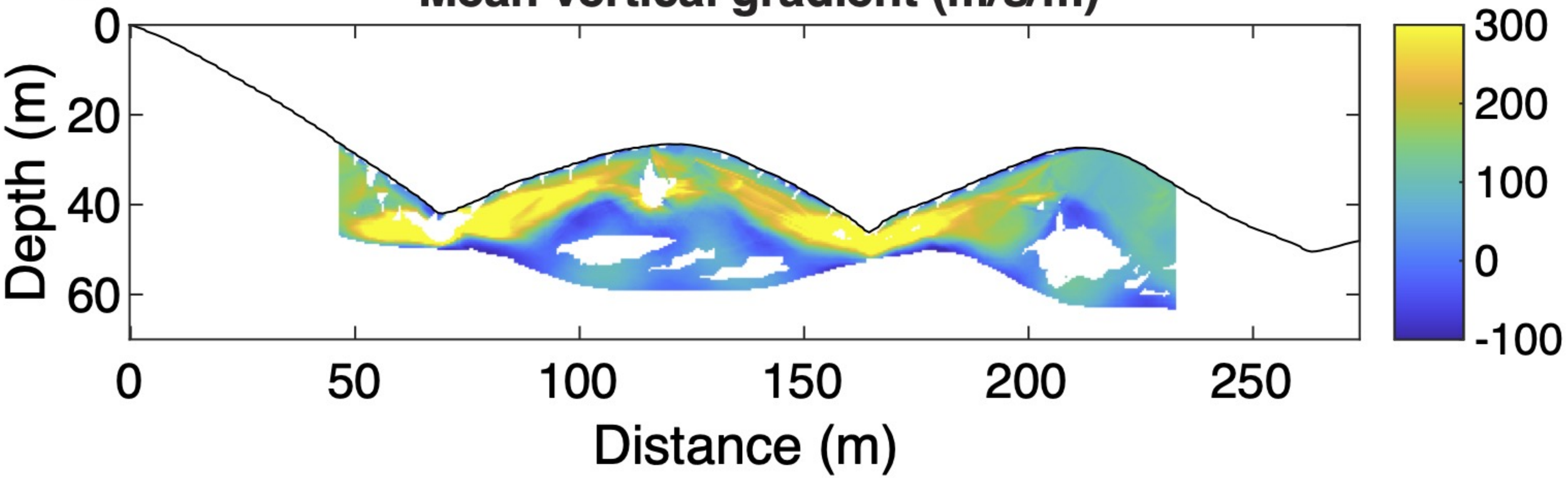

Figure_07.

a W **Mean velocity (m/s)** E

F: MH3-W4
G: MH3-W3
H: MH3-W1

MH3R

G H F

Line 8

Line 7

Sandstone cap

Depth (m)

0 20 40 60 80 100 120

0 50 100 150 200 250 300 350 400

4000 3000 2000 1000 0

b **Mean vertical gradient (m/s/m)**

Depth (m)

0 20 40 60 80 100 120

0 50 100 150 200 250 300 350 400

Distance (m)

200 100 0 -100

Figure_08.

a

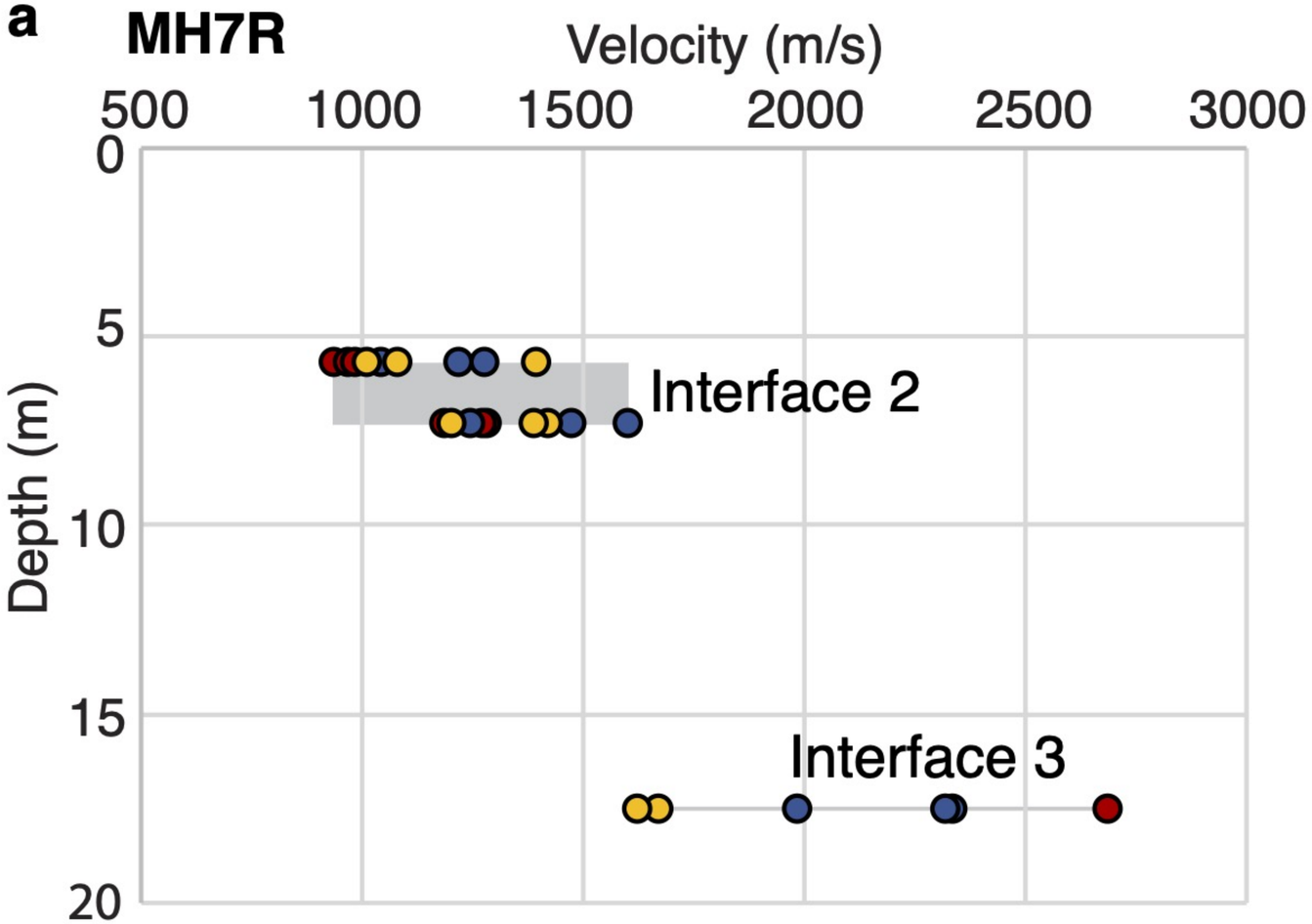

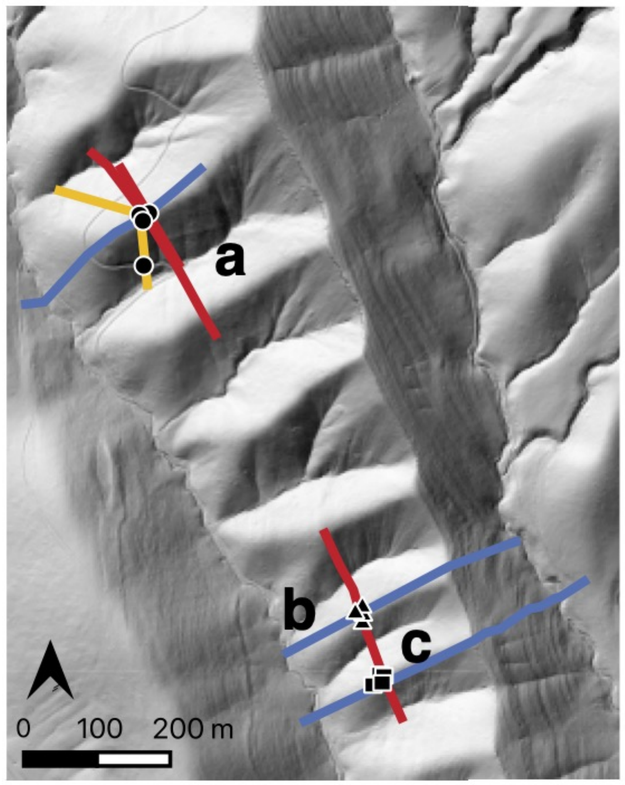

Bedding-∥

Bedding-⊥

Steepest Descent

b

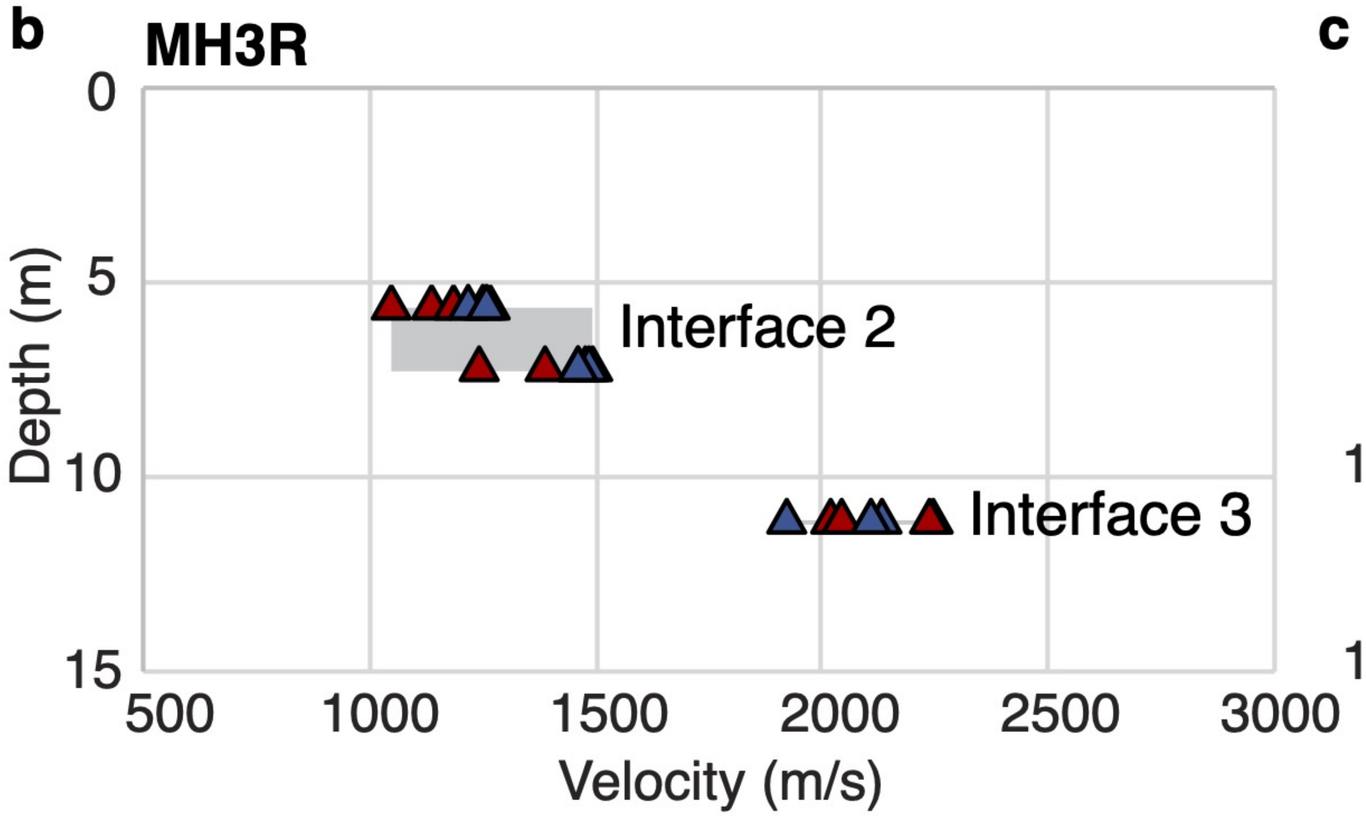

c

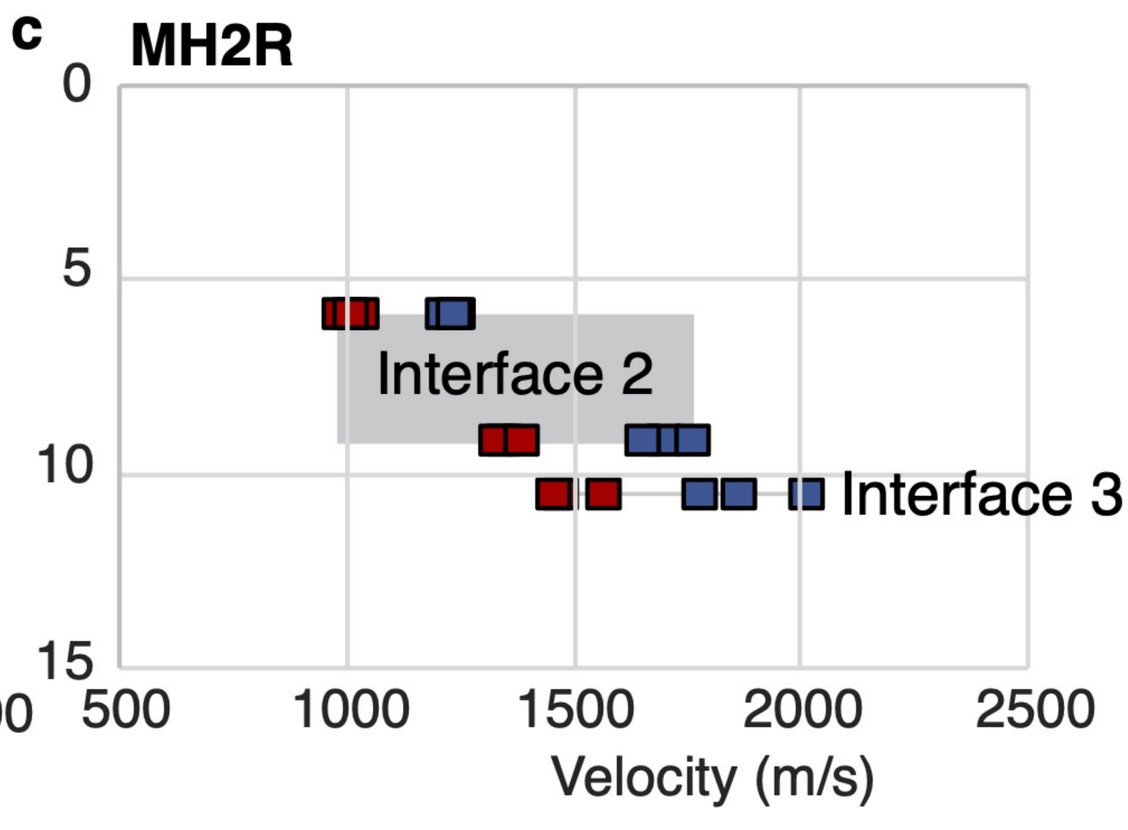

Figure_09.

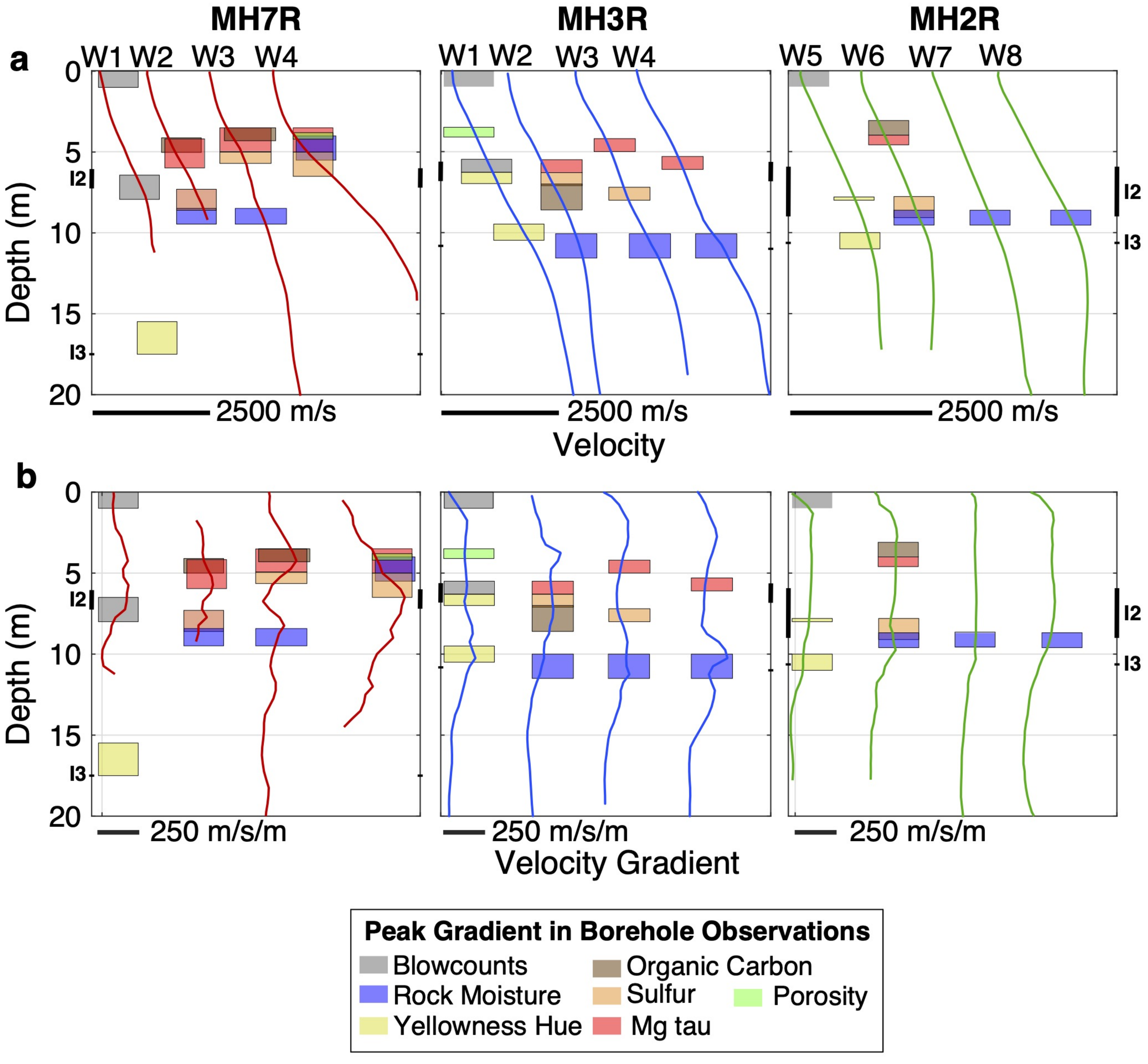
MH7R
MH3R
MH2R
a
W1 W2 W3 W4
W1 W2 W3 W4
W5 W6 W7 W8
Depth (m)
0
5
10
15
20
I2
I3
2500 m/s
2500 m/s
2500 m/s
Velocity
b
250 m/s/m
250 m/s/m
250 m/s/m
Velocity Gradient
Peak Gradient in Borehole Observations
Blowcounts
Organic Carbon
Rock Moisture
Sulfur
Porosity
Yellowness Hue
Mg tau

Figure_10.

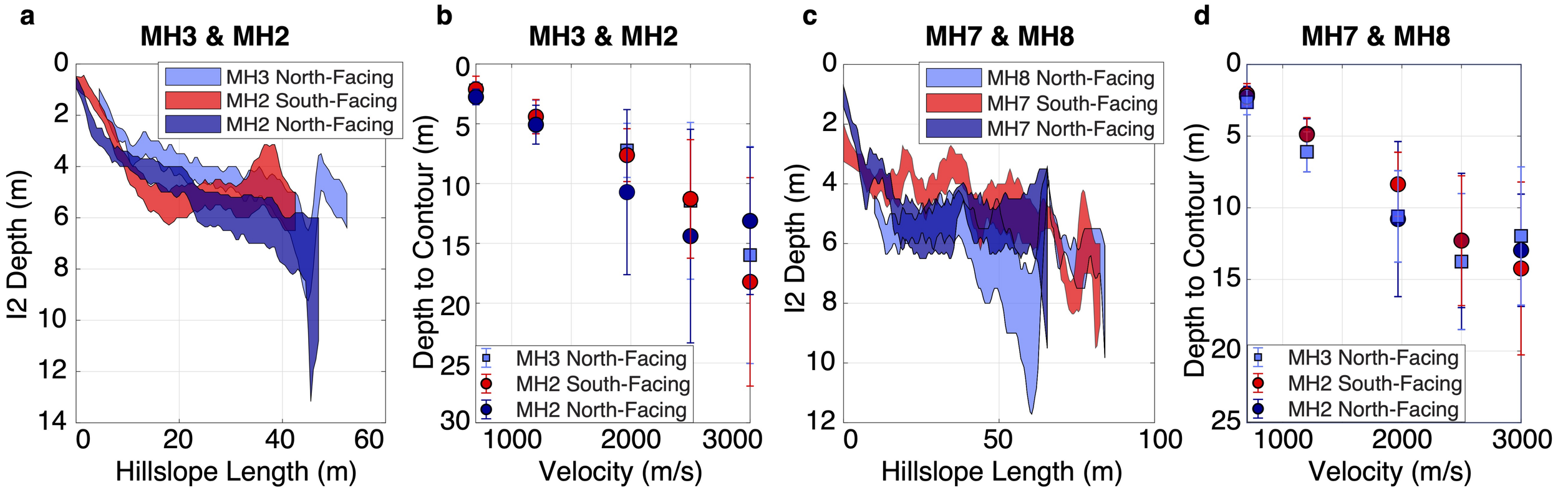
a
MH3 & MH2
MH3 North-Facing
MH2 South-Facing
MH2 North-Facing
l2 Depth (m)
Hillslope Length (m)
b
MH3 & MH2
MH3 North-Facing
MH2 South-Facing
MH2 North-Facing
Depth to Contour (m)
Velocity (m/s)
c
MH7 & MH8
MH8 North-Facing
MH7 South-Facing
MH7 North-Facing
l2 Depth (m)
Hillslope Length (m)
d
MH7 & MH8
MH3 North-Facing
MH2 South-Facing
MH2 North-Facing
Depth to Contour (m)
Velocity (m/s)

Figure_11.

a

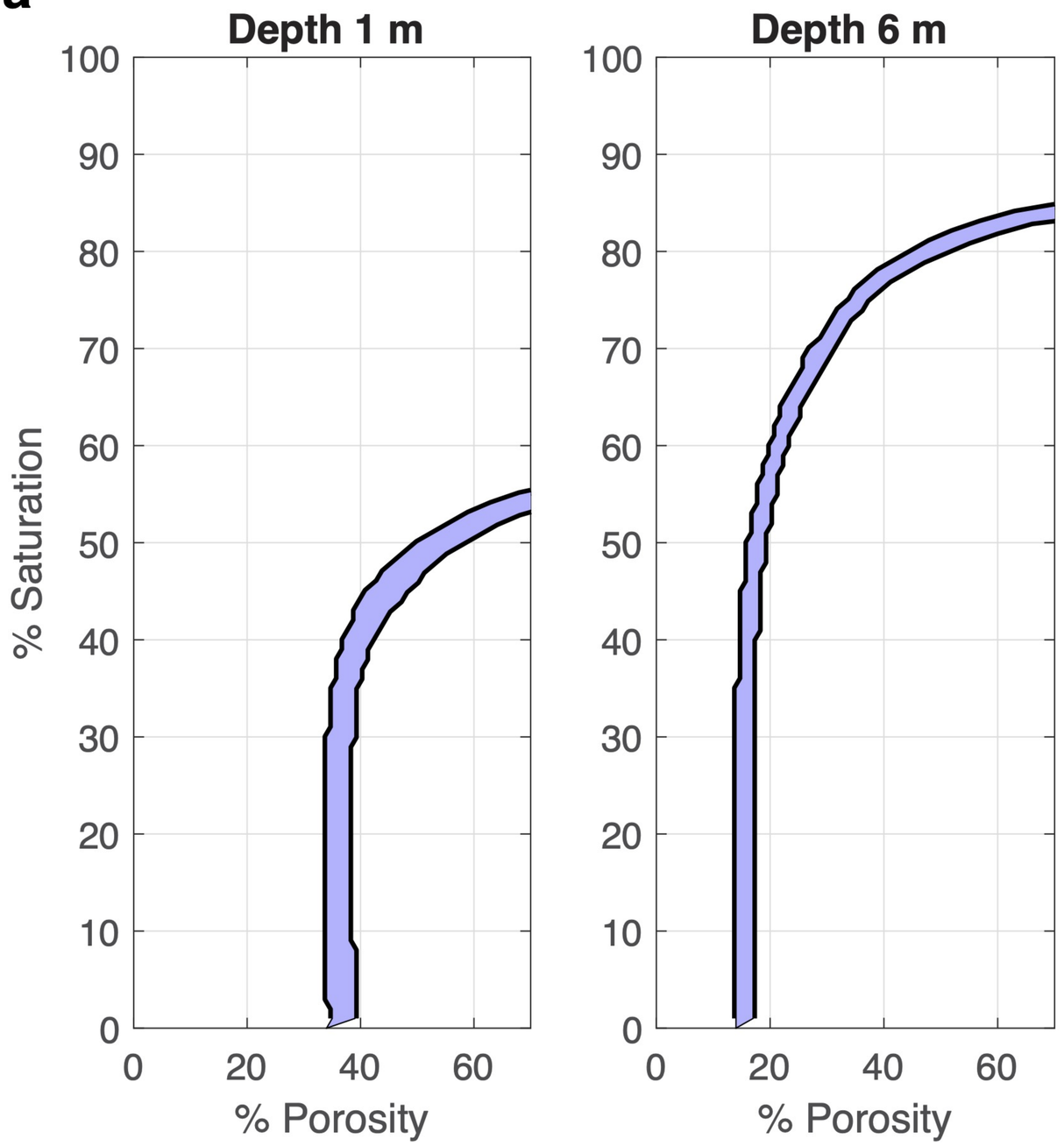
Depth 1 m
Depth 6 m
% Saturation
100
90
80
70
60
50
40
30
20
10
0
0
20
40
60
% Porosity

b

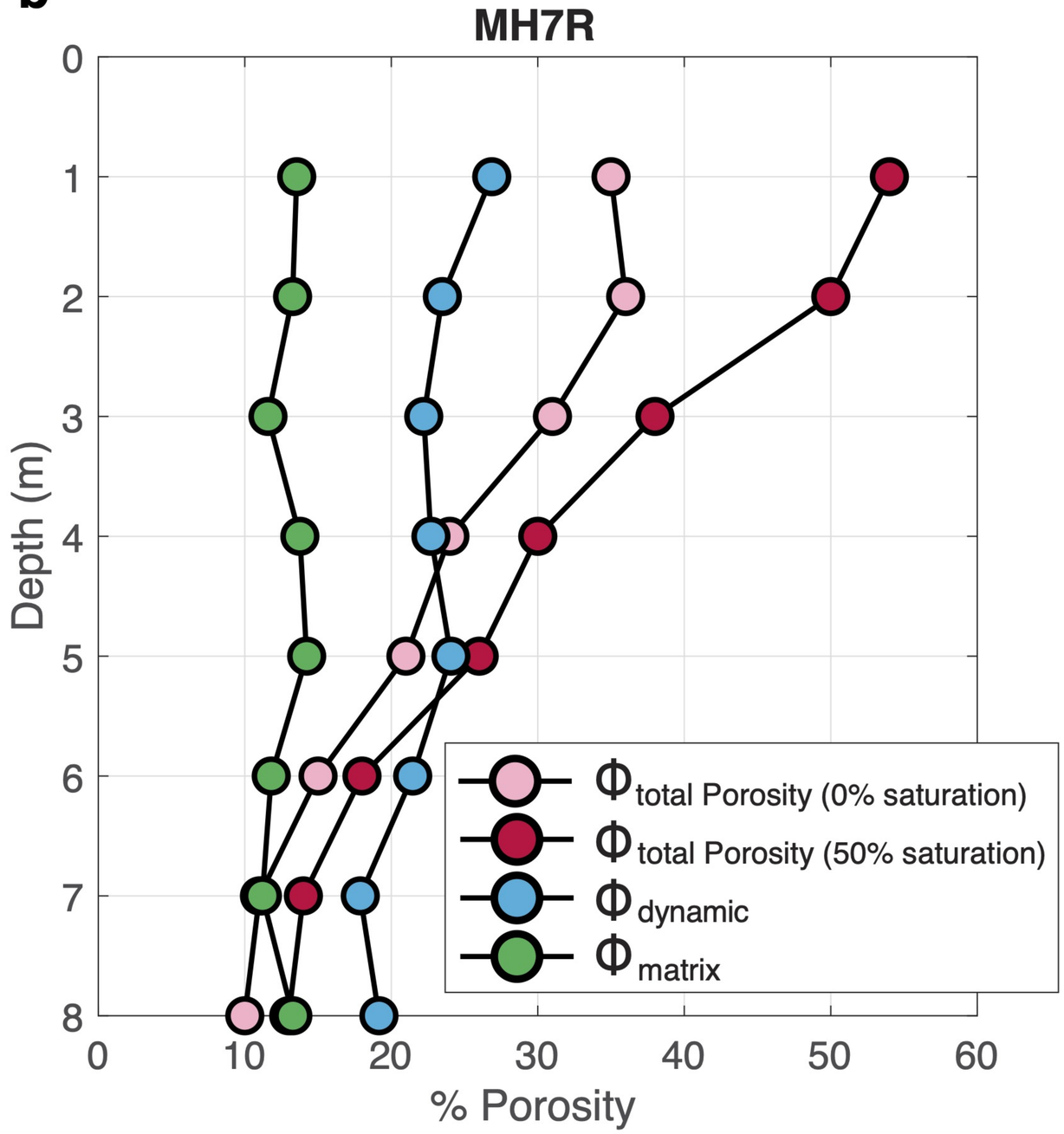
MH7R
Depth (m)
0
1
2
3
4
5
6
7
8
0
10
20
30
40
50
60
% Porosity
Φ total Porosity (0% saturation)
Φ total Porosity (50% saturation)
Φ dynamic
Φ matrix

c

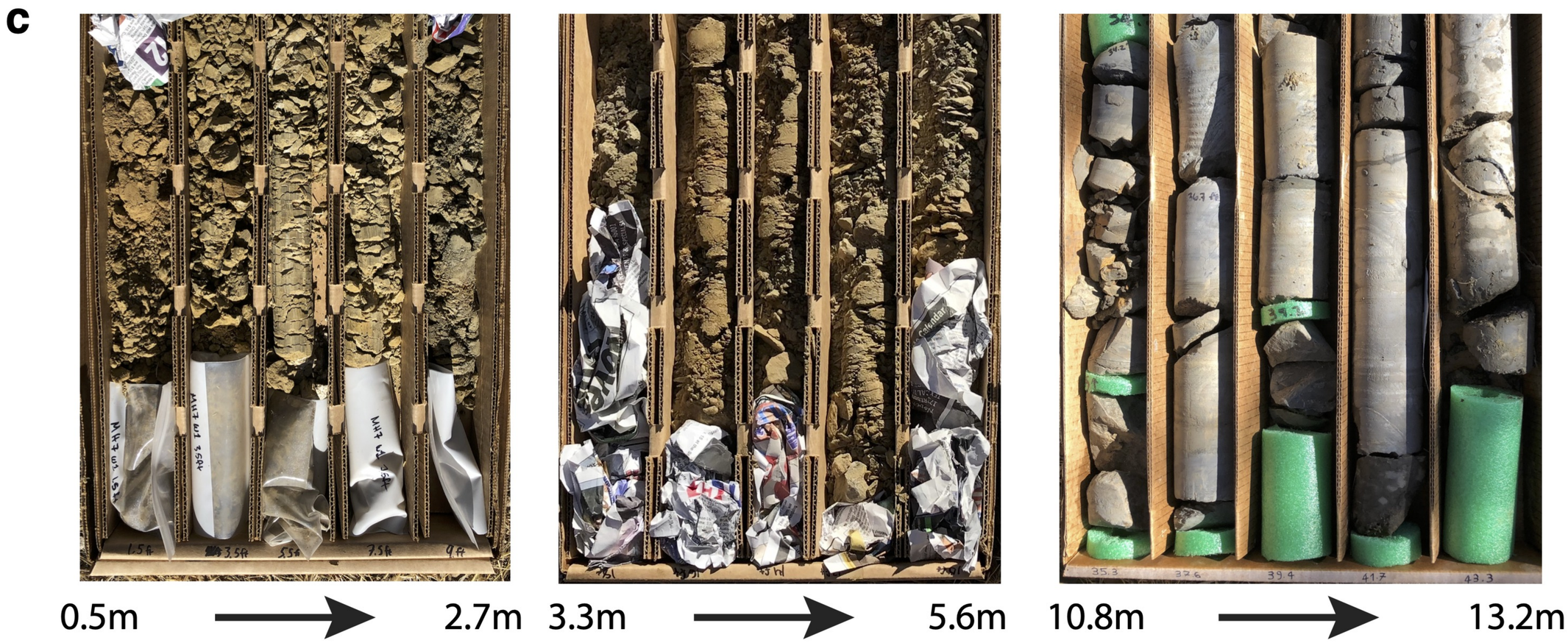
0.5m
2.7m
3.3m
5.6m
10.8m
13.2m

Figure_12.

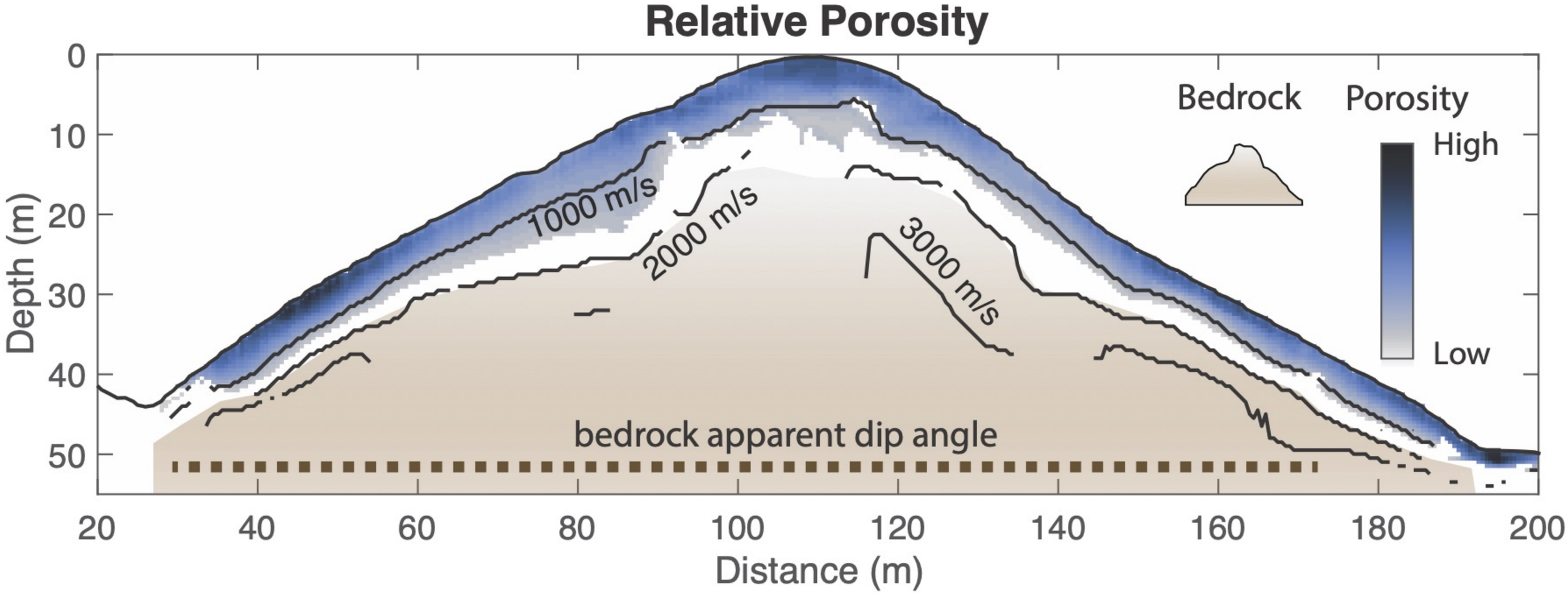
Relative Porosity
Depth (m)
0
10
20
30
40
50
20
40
60
80
100
120
140
160
180
200
Distance (m)
Bedrock
Porosity
High
Low
1000 m/s
2000 m/s
3000 m/s
bedrock apparent dip angle

Figure_13.

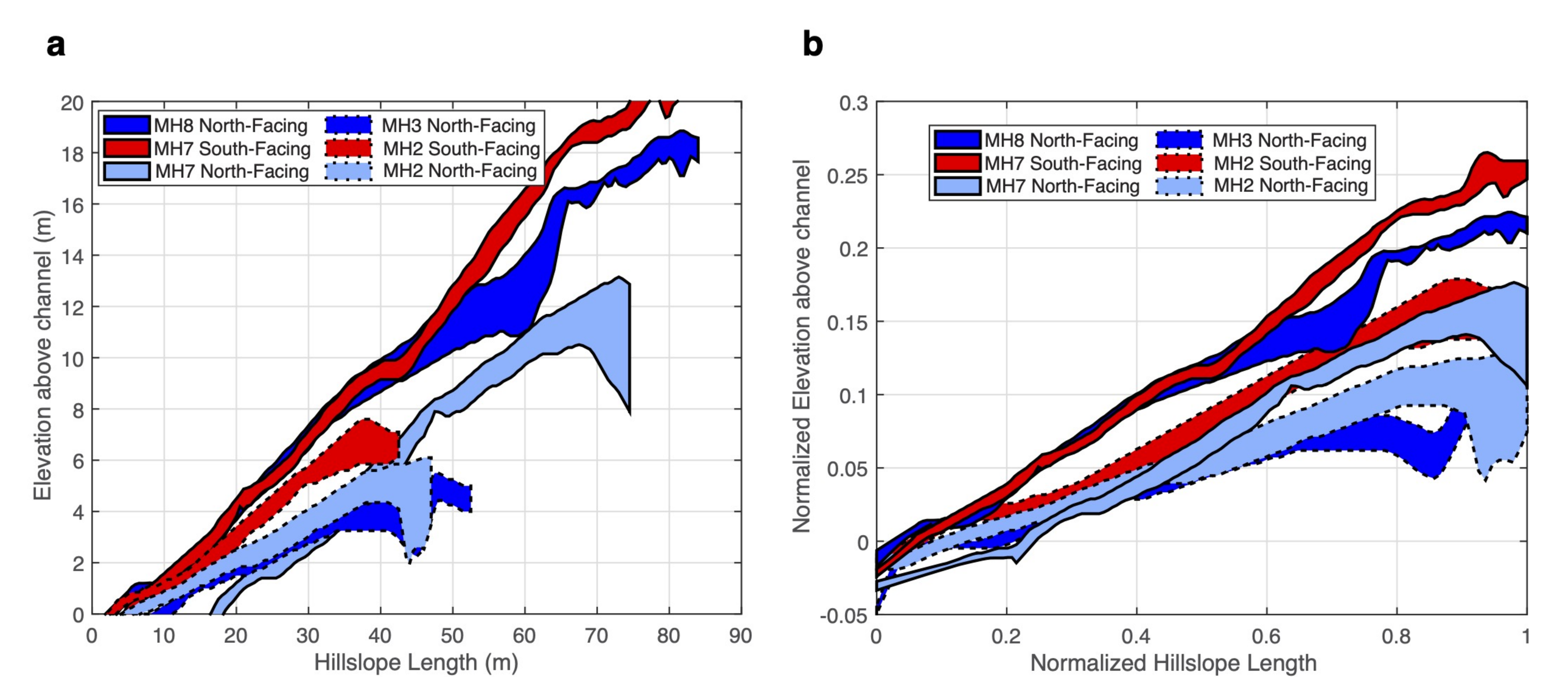
a
b
MH8 North-Facing
MH7 South-Facing
MH7 North-Facing
MH3 North-Facing
MH2 South-Facing
MH2 North-Facing
Elevation above channel (m)
Hillslope Length (m)
Normalized Elevation above channel
Normalized Hillslope Length
0
10
20
30
40
50
60
70
80
90
2
4
6
8
12
14
16
18
20
-0.05
0.05
0.1
0.15
0.2
0.25
0.3
0.4
0.6
0.8
1

JGR: Earth Surface

Supporting Information for

Mapping variations in bedrock weathering with slope aspect under a sedimentary ridge-valley system using near-surface geophysics and drilling

Berit M. Hudson Rasmussen[1], Mong-Han Huang[1], W. Jesse Hahm[2], Daniella M. Rempe[3], David Dralle[4], and Mariel D. Nelson[3]

[1]Department of Geology, University of Maryland, College Park, MD, USA,
[2]Department of Geography, Simon Fraser University, Burnaby, BC, Canada,
[3]Department of Geosciences, Jackson School of Geosciences, The University of Texas at Austin, Austin, TX, USA,
[4]Pacific Southwest Research Station, United States Forest Service, Albany, CA, US

Contents of this file

Introduction

Text S1 describes seismic velocity results not shown in the main text.
Figure S1 shows seismic line 2 results parallel to the bedding.
Figure S2 shows seismic line 3 results perpendicular to the bedding.
Figure S3 compares velocity profile with seismic velocity surveyed parallel or perpendicular to the bedding.
Figure S4 shows seismic lines 4 and 5 result along two maximum hillslope descend profiles.
Figure S5 shows seismic line 9 results perpendicular the bedding and across the main ridge.
Figure S6 shows seismic lines 10 and 11 results along the MH2 channel.
Figure S7 compares the critical zone structure for north- and south-facing hillslopes for lines 4 and 5, respectively.
Figure S8 compares weathering thickness on north- and south-facing hillslopes for line 6.
Figure S9 compares weathering thickness between north- and south-facing hillslopes of MH2, MH3, MH7, and MH8 based on interface 3 property.
Figure S10 shows a 1D porosity model for MH3R (Line 7).
Figure S11 shows a 1D porosity model for MH2R (Line 7).
Figure S12 compares 1D velocity profiles between mean west- and east-facing hillslopes of lines 8 and 9.
Figure S13 shows an average porosity with depth for the MH7R ridgetop.
Figure S14 shows the topography of interface 3 along north or south facing hills.
Table S1 lists the model parameters used for the seismic inversion.
Table S2 lists the elastic moduli for minerals used in the rock physics model.

Supplementary Text S1 – Summary of seismic velocity models (lines 3, 4, 5, 9)

S1.1 MH7R Bedding-Perpendicular (Line 3)

The low-velocity material of the bedding-perpendicular profile (Line 3; **Figure S2**) is generally faster than material in the same depth range of the bedding-parallel profile (**Figures 4, S1**). CoV is < 20% almost everywhere above the deepest raypath, indicating consistency of velocity distribution between model ensembles (**Figure S2b**). The mean vertical gradient is lower than that of the bedding-parallel survey line, indicating a more gradual increase in velocity with depth (**Figure S2c**). The highest gradients (> 500 m/s/m) are located below the channel. 1D velocity at the intersection point with bedding-parallel Line 1 indicates an overall similar profile, however Line 3 is slightly faster above a 6m depth (**Figure S3**). Similar to Lines 1 and 2, we do not reach high-velocity material below the MH7R ridgetop in this survey line.

S1.2 MH8 North-Facing Slope (Line 4) and MH7 South-Facing Slope (Line 5)

Lines 4 (north-facing) and 5 (south-facing) are traced roughly perpendicular to the topographic contour lines to capture the steepest descent of the hillslope. Both survey lines show upslope-thickening weathering with a 30 m-thick weathered zone at the ridgetop (**Figure S4a,c**). The two slopes appear to have a similar thickness of low-velocity material, although the south-facing slope has considerably thinner mid-velocity (1000-3000 m/s) material. Velocity appears to increase more gradually below the north-facing slope and increases more rapidly on the south-facing slope. There is Vp > 4000 m/s visible more than halfway up the south-facing slope, faster than is resolved in Line 1. Line 5 also resolves deeper (~35 m) below the MH7R ridge than Line 1 (only ~15 m), possibly due to a longer maximum source-receiver distance for Lines 4 and 5.

S1.3 MH2R Perpendicular (Line 9)

Three boreholes at MH2R are within 10 m of Line 9: MH3-W5, MH3-W7, and MH3-W8. CoV is high (> 50%) below the ridgetop, but along the slopes, we can resolve up to 30-40 m depth. Velocity gradient is once again highest at the channels and is generally < 200 m/s/m elsewhere (**Figure S5a**). Similar to Line 8, velocity appears mostly sub-parallel to the topography (**Figure 7**). The low-velocity layer is uniformly 6-8 m thick along the east-facing slope of the MH2R perpendicular profile, with the exception of the eastern channel where it is < 3 m thick. The middle-velocity layer is more variable, increasing to > 10 m thick where the slope angle is most gradual, and thinning where the hillslope is steepest. The mid-velocity layer is nearly absent at the eastern channel, but it is still several meters thick at the western channel.

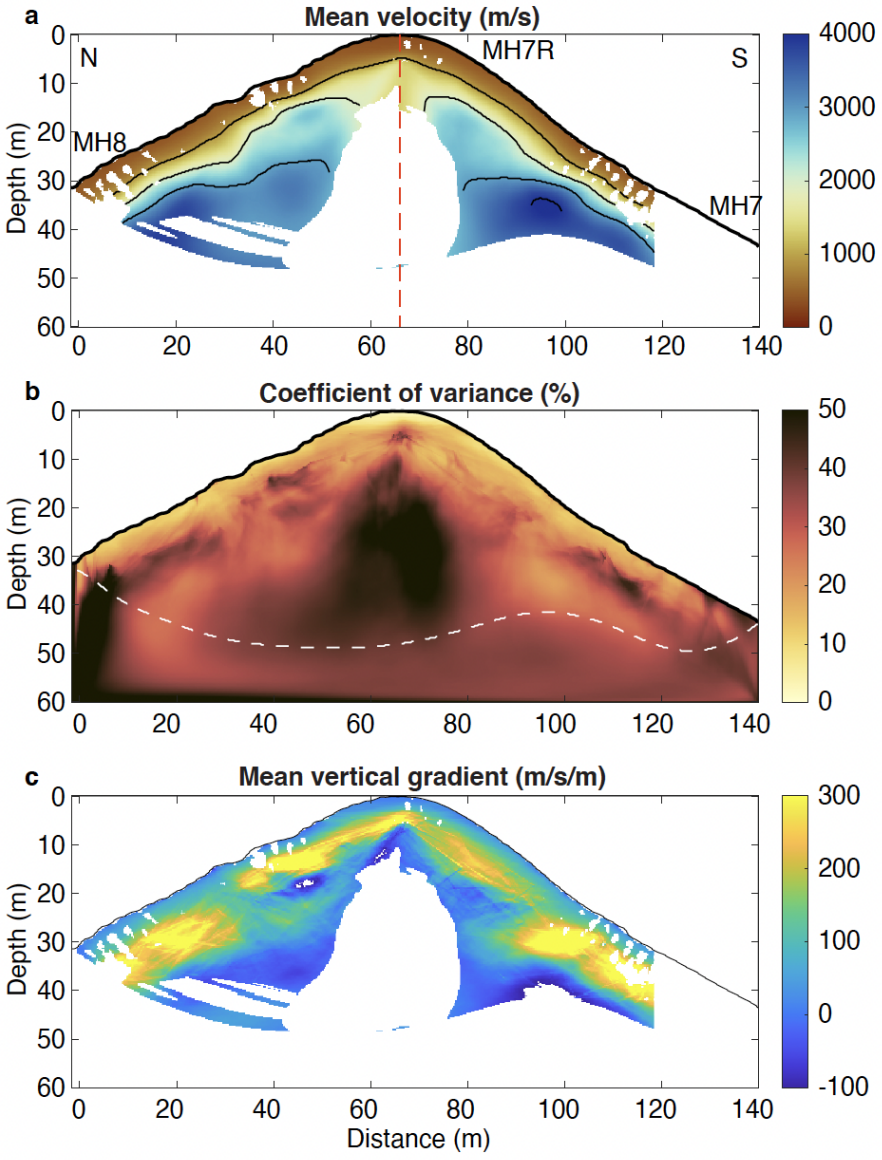

Figure S1. Results of Line 2 (**a-c**) inversion using THB rj-MCMC (Huang et al., 2021). (**a**) Mean velocity model with contour lines at 1000, 2000, 3000, and 4000 m/s. The model is masked out where no geophones are present (edges of survey), below the deepest raypath, and where coefficient of variation (CoV; standard deviation/mean velocity x 100) > 30%. The vertical dashed line highlights the locations of borehole MH7-W1. The same line also indicates the intersection point of Line 2 with Line 1 (see Figure 1b). (**b**) Percent CoV with the deepest raypath as the white dashed line. (**c**) Mean vertical velocity gradient (m/s/m).

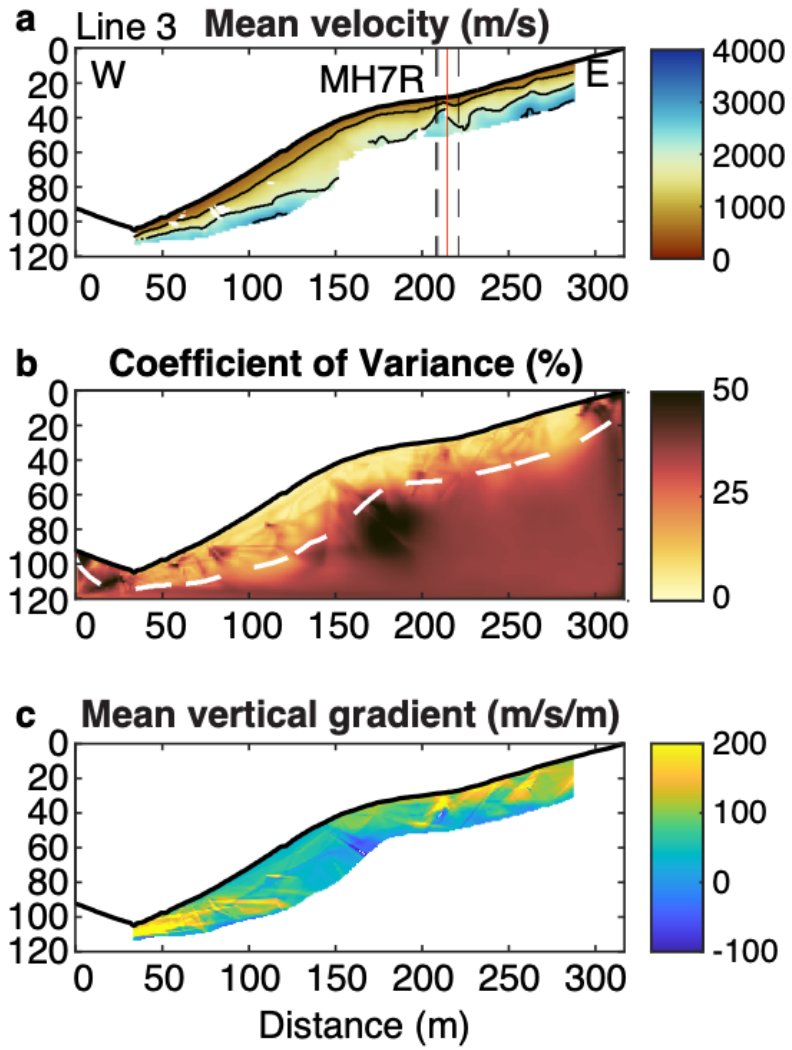

Figure S2. Results of Line 3 (**a-c**) inversion using THB rj-MCMC (Huang et al., 2021). (**a**) Mean velocity model with contour lines at 1000, 2000, 3000, and 4000 m/s. The model is masked out where no geophones are present (edges of survey), below the deepest raypath, and where coefficient of variation CoV > 30%. Vertical dashed lines highlight the locations of boreholes within 10 m of the survey line. From west to east, these include boreholes MH7-W2, MH7-W3, and MH7-W1. The orange vertical line indicates the intersection point of Lines 1 and 3. (**b**) Percent CoV with the deepest raypath as the white dashed line. (**c**) Mean vertical velocity gradient (m/s/m).

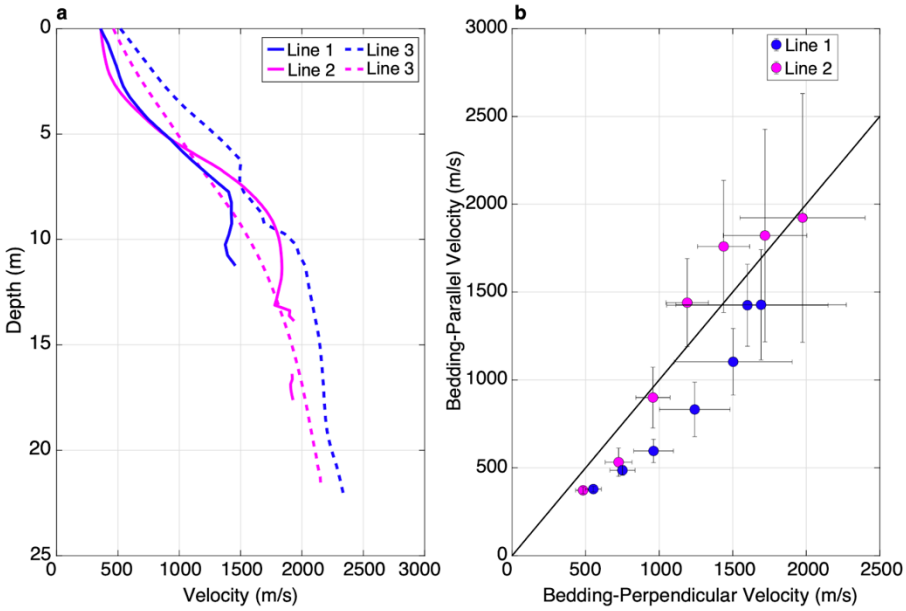

Figure S3. Velocity with depth at the intersection points of bedding-parallel and bedding-perpendicular survey lines for MH7R. (**a**) Solid and dashed lines show the velocity for bedding-parallel and bedding-perpendicular lines, respectively. (**b**) Bedding-perpendicular velocity vs bedding-parallel velocity. Blue circles represent the velocities at the intersection of Lines 1 and 3, and pink circles represent the velocities at the intersection of Lines 2 and 3.

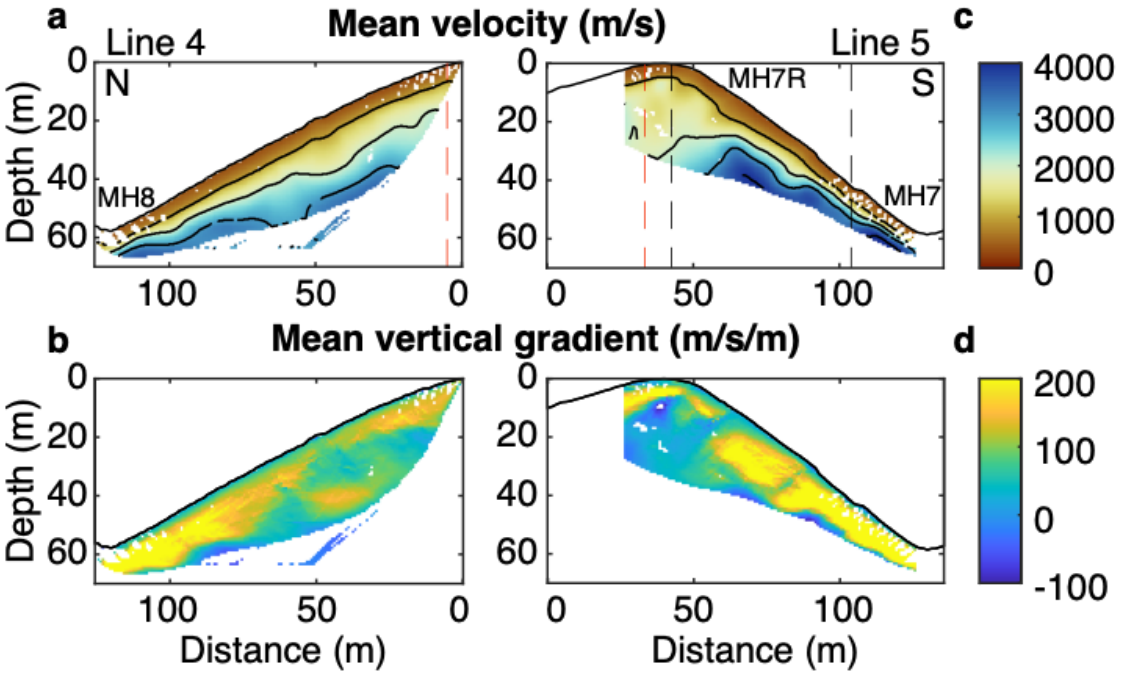

Figure S4. Results of Line 4 (**a-b**) and Line 5 (**c-d**) inversions. (**a,c**) Mean velocity model with contour lines at 1000, 2000, 3000, and 4000 m/s. The model is masked out below the deepest raypath and where CoV > 30%. Black dashed lines highlight the locations of boreholes within 10 m of the survey line (borehole MH7-W2 for Line 4; boreholes MH7-W2, MH7-W3, and MH7-W4 for Line 5). Lines 4 and 5 intersect at the MH7-W2 borehole (red dashed line). (**b,d**) Mean vertical velocity gradient (m/s/m).

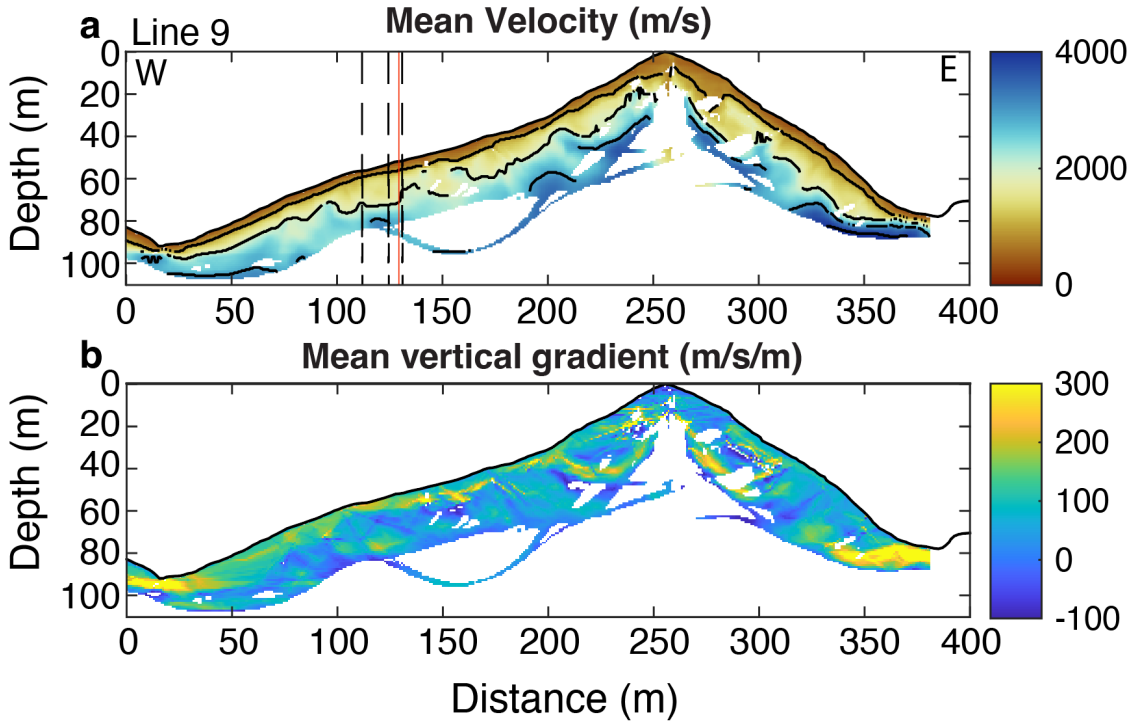

Figure S5. Results of Line 9 inversion. (**a**) Mean velocity model with contour lines at 1000, 2000, 3000, and 4000 m/s. The model is masked out below the deepest raypath and where CoV > 40%. Black dashed lines highlight the locations of boreholes within 10 m of the survey line. From west to east, these include boreholes MH3-W8, MH3-W7, and MH3-W5. The orange vertical line indicates the intersection point with Line 7. (**b**) Mean vertical gradient (m/s/m). Note the gradient color scale ranges from -100 to 300 m/s/m.

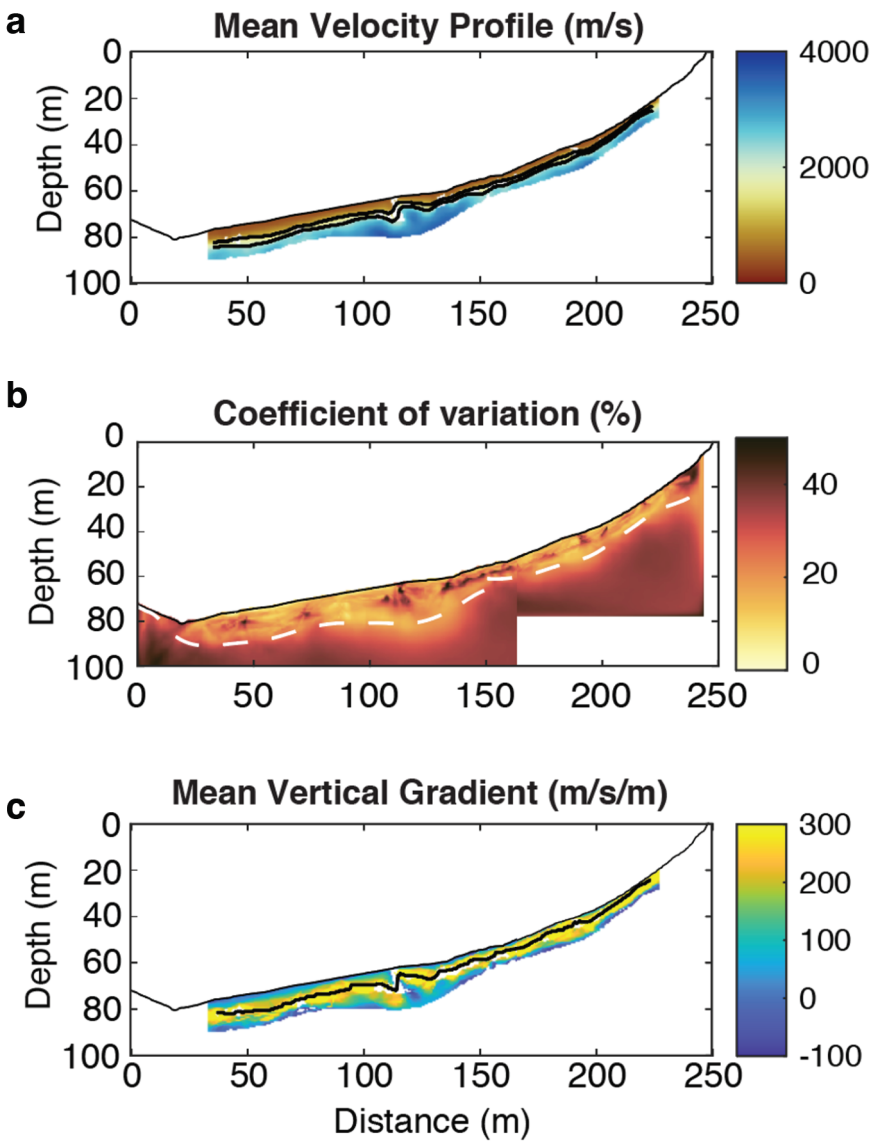

Figure S6. Results of Lines 10 and 11 (**a**-**c**) inversion using THB rj-MCMC (Huang et al., 2021). (**a**) Mean velocity model with contour lines at 1000, 2000, 3000, and 4000 m/s. The model is masked out where no geophones are present (edges of survey), below the deepest raypath, and where CoV > 30%. (**b**) Percent CoV with the deepest raypath as the white dashed line. (**c**) Mean vertical velocity gradient (m/s/m).

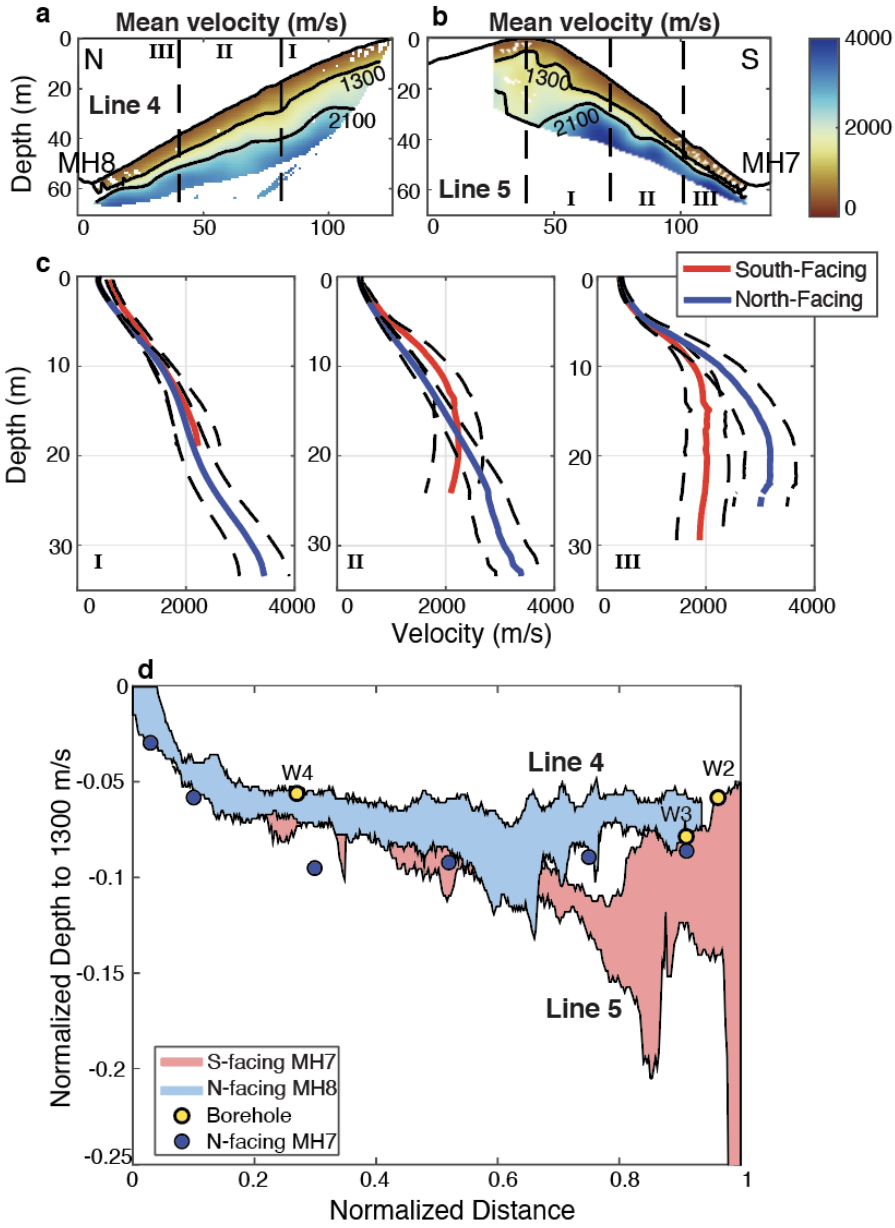

Figure S7. Comparison of Interface 2 depth for north- and south-facing hillslopes of Lines 4 and 5 (steepest descent of the slope). Mean velocity profiles for Lines 4 and 5 are shown in (**a**) and (**b**), respectively. Contour lines are at the approximate velocities of the Interface 2 (1284 m/s) and Interface 3 (1972 m/s) transitions. Roman numerals indicate three sections of the hillslopes used in (**c**). (**c**) shows 1D velocity profiles for three sections of the hillslope for north-facing (blue) and south-facing (red) slopes. Dashed black lines indicate 1 standard deviation. (**d**) Normalized depth to Interface 2 (1284 m/s contour) with normalized hillslope length. Zero is the channel and one is the ridgetop position. Blue circles represent points where Line 1 intersects a steepest descent transect, since we have no steepest descent survey line for MH7N. Yellow circles represent normalized Interface 2 depth in boreholes MH7-W2, MH7-W3, and MH7-W4.

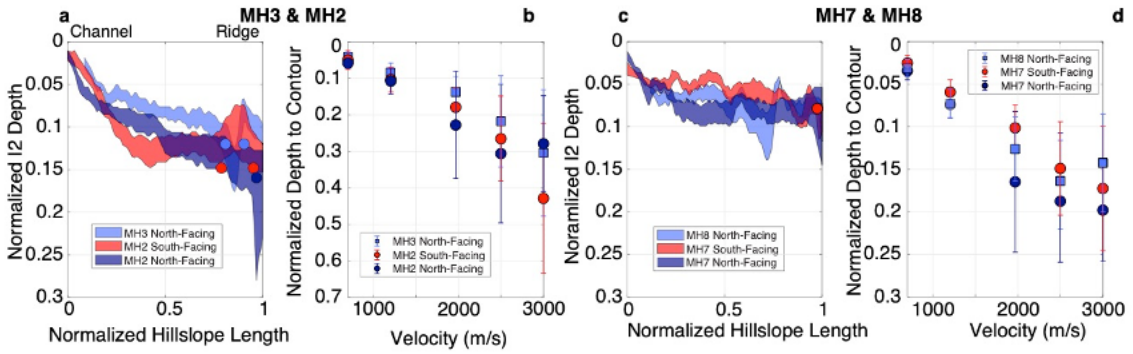

Figure S8. Comparison of weathering thickness on north- versus south-facing hillslopes for Line 6 (**ab**), and Line 1 (**cd**). Depth to Interface 2 (I2; saprolite-weathered bedrock) with normalized hillslope length (**a,c**) is shown based on the I2 velocity range (1284 ± 203 m/s velocity contours). Average depths to various velocity contours are shown normalized to hillslope length in (**b, d**), including the average Interface 2 velocity contour (1284 m/s) and average Interface 3 velocity contour (1973 m/s).

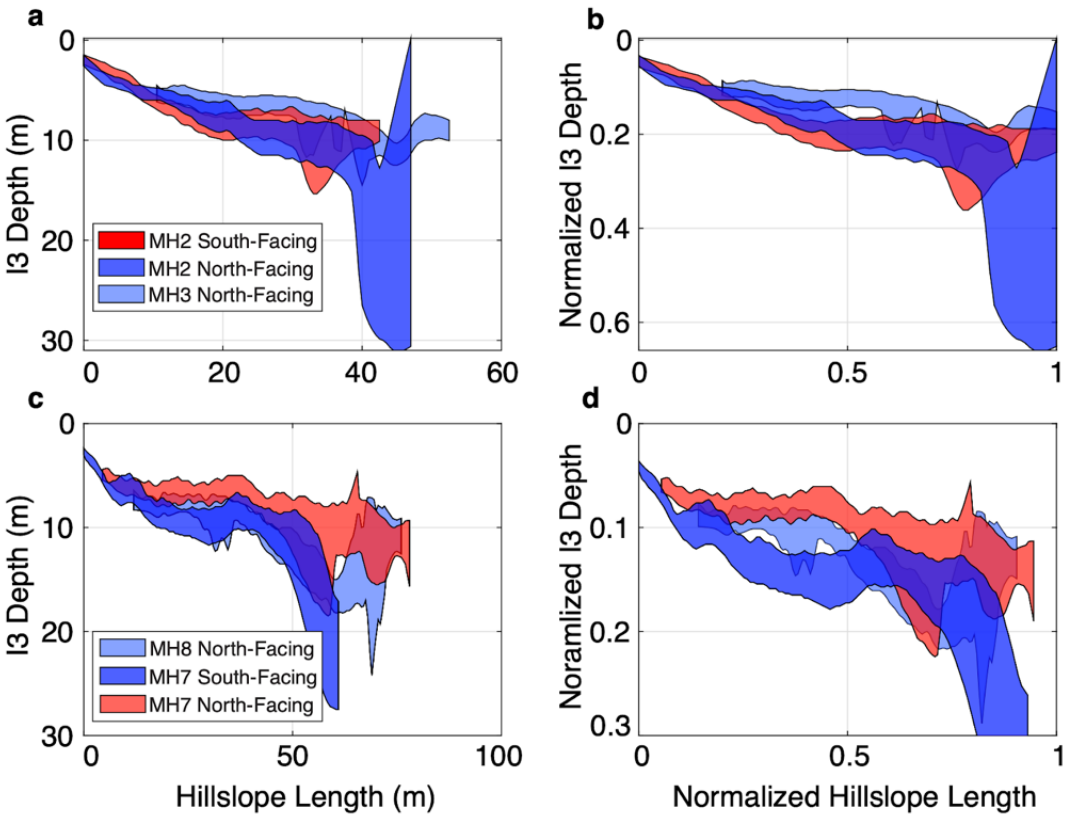

Figure S9. Comparison of weathering thickness on north- versus south-facing hillslopes for Line 6 (**a-b**), and Line 1 (**c-d**). Depth to Interface 3 (I3; weathered-unweathered bedrock transition) with hillslope length is shown based on the 1972 m/s velocity contour. (**b,d**) represent the same as (**a,c**), but hillslope length and depth to I3 are normalized by the hillslope length.

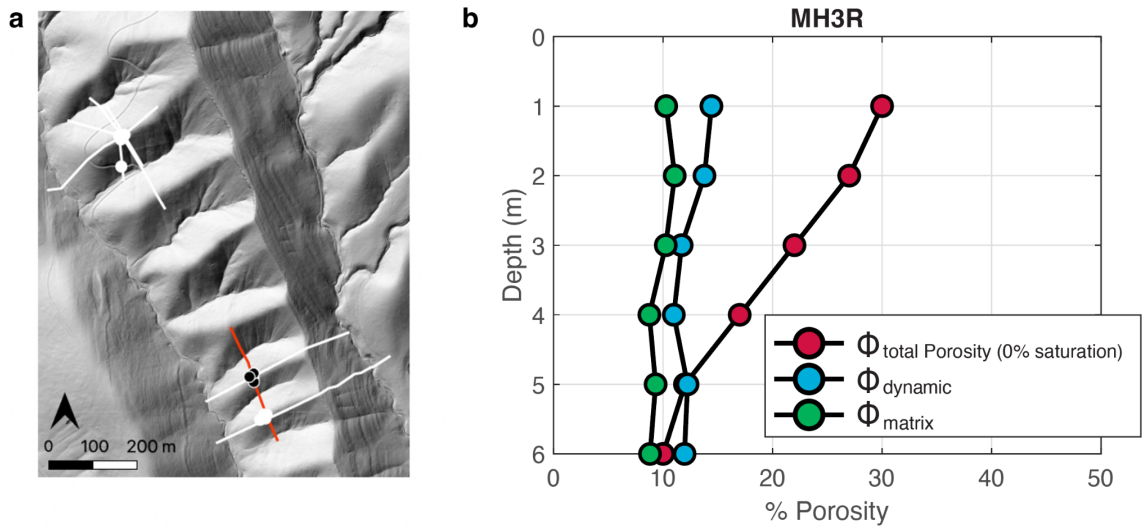

Figure S10. 1D rock physics model at MH3R (Line 7). (**a**) Location of Line 7 (red line) and the boreholes used to measure volumetric water content (black circles). (**b**) Porosity with depth from the rock physics model (Φ_{total}) based on the average velocity profile across all wells at MH3R. Measured matrix porosity (Φ_{matrix}) from cores at MH3-W2, MH3-W4, and MH3-W4, interpolated to a 1m depth is shown in green. The dynamic porosity ($\Phi_{dynamic}$) is based on neutron probe measurements at MH7-W2 and MH7-W3, with outliers removed and also interpolated to 1m depth.

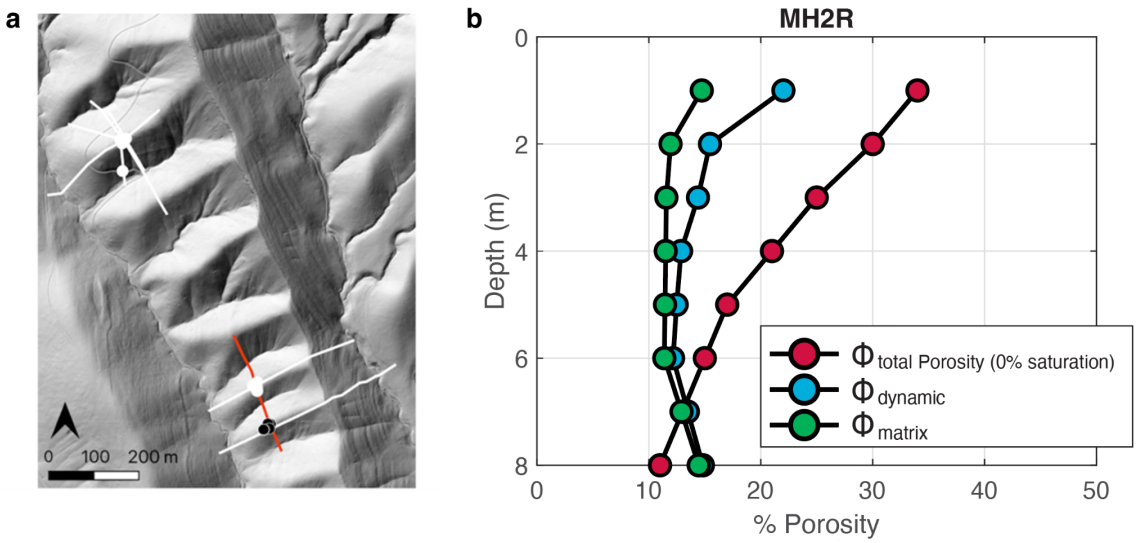

Figure S11. 1D rock physics model at MH2R (Line 7). (**a**) Location of Line 7 (red line) and the boreholes used to measure volumetric water content (black circles). (**b**) Porosity with depth from the rock physics model (Φ_{total}) based on the average velocity profile across all wells at MH2R. Measured matrix porosity (Φ_{matrix}) from cores at MH7-W1, MH7-W2, and MH7-W3, interpolated to a 1m depth is shown in green. The dynamic porosity ($\Phi_{dynamic}$) is based on neutron probe measurements at MH3-W6 and MH3-W7, with outliers removed and also interpolated to 1m depth.

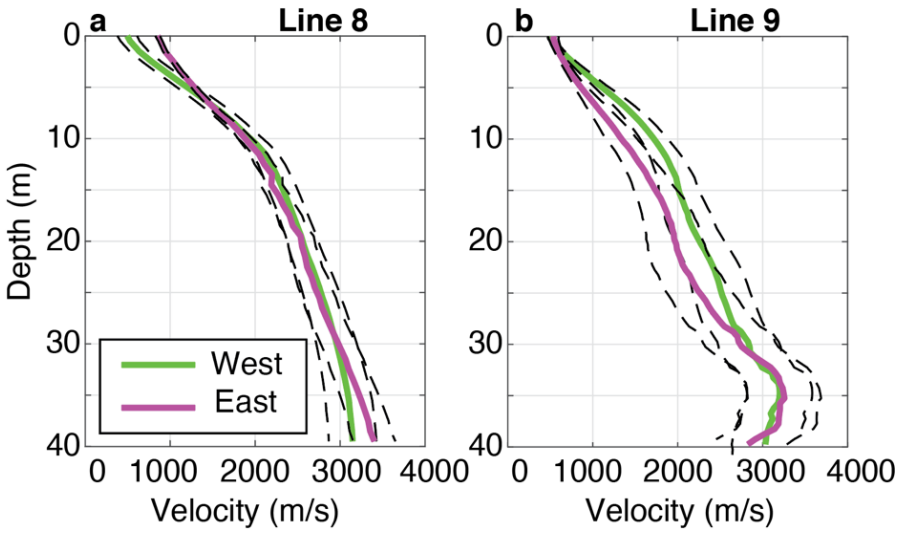

Figure S12. Average 1D velocity profile across the entire west-facing (green) and east-facing (pink) slopes for Lines 8 (**a**) and 9 (**b**). Dashed black lines represent 1 standard deviation.

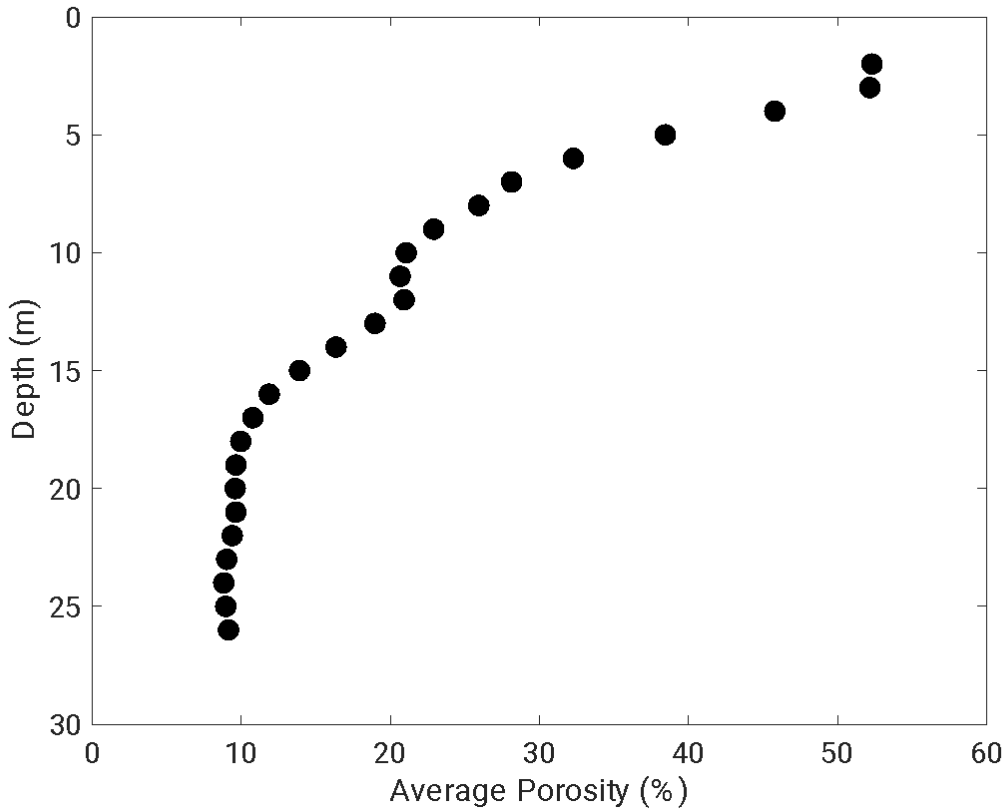

Figure S13. Average porosity with depth for the MH7R ridgetop (Line 1). Porosity values were averaged across 180-200 m horizontal distance of the 2D model (**Figure 12**).

Table S1. List of model parameters used in different seismic refraction survey lines.

Survey Line	Date	Geophone Number, Spacing (m)	Grid Size (m)	Markov Chains	Iterations	Mean misfit (ms)	Std. Dev. of Misfit (ms)	Noise Hyper-parameter (ms)
Line 1	08/2019	24, 3	0.5	10	1.5×10^6	1.23	1.6	1.47
Line 2	08/2021	48, 3	0.25	100	1.2×10^6	0.84	1.09	1.09
Line 3	08/2019	24, 3	0.5	15	1.0×10^6	1.67	2.13	2.00
Line 4	08/2021	48, 3	0.25	100	1.5×10^6	1.30	1.70	1.23
Line 5	08/2021	48, 2.5	0.25	100	1.5×10^6	1.16	1.47	1.16
Line 6	08/2021	48, 2	0.25	18	1.3×10^6	0.89	1.17	1.05
Line 7	12/2019	24, 3	0.5	15	1.2×10^6	1.14	1.64	1.62
Line 8	08/2021	48, 5	1	10	0.7×10^6	1.75	2.25	2.23
Line 9	01/2018	72, 2	0.5	15	2.9×10^6	1.35	1.85	1.5-1.8
Line 10/11	12/2019	24, 3	0.5	10	0.8×10^6/ 1.0×10^6	1.29/0.96	1.78/1.23	1.70/1.20

Table S2. Elastic moduli for minerals used in rock physics models (Mavko et al., 2009; Gu et al., 2020s).

Mineral	Bulk Modulus (Pa)	Shear Modulus (Pa)
Quartz	37×10^9	44×10^9
Feldspar	37.5×10^9	15×10^9
Illite	52.3×10^9	31.7×10^9